1 2 90

UNIVERSIDADE DE
COIMBRA

Nuno Gonçalo Pereira Portela Branco

Axiões e Instabilidades Superradiantes de buracos negros primordiais

Dissertação no âmbito do mestrado em Física, ramo de Física Nuclear e de Partículas, orientada pelo Professor Doutor João Rosa e pelo Doutor Ricardo Zambujal Ferreira, e apresentada ao Departamento de Física da Faculdade de Ciências e Tecnologia da Universidade de Coimbra.

Setembro de 2022

Faculty of Sciences and Technology
University of Coimbra

Axions and Superradiant Instabilities of Primordial Black Holes

Nuno Gonçalo Pereira Portela Branco

A thesis written in fulfilment of the requirements for the Physics MSc Program,
Supervised by Prof. Dr. João Rosa and Dr. Ricardo Zambujal Ferreira.

September 2022

Abstract

Black holes are a great laboratory to probe high energy physics. Recent works studied black holes that, through the superradiant instability phenomenon, produce in their vicinity a cloud constituted by the quantum chromodynamics axion or axion-like particles. In this thesis, we analyze some of the phenomenological aspects of the underlying physics of these systems focusing on their applications to cosmology and astrophysics.

We review the Klein Gordon equation for a massive scalar field in the Kerr spacetime, which leads to superradiant instabilities of the particles connected with the field. We obtain an analytical approximation to the radial part of the solution and interpret physical properties of the particle cloud in analogy with the Hydrogen atom. Then, we propose axions as candidates for these systems and we review the quantum chromodynamics axion as well as the physics underlying this beyond the Standard Model particle. To complete these systems, we ponder primordial black holes due to their wide mass range and we present a review on these objects' formation mechanism. Then, we study the dynamics of a system composed by a rotating primordial black hole, assuming primordial black holes are a relevant fraction of the dark matter, surrounded by a cloud of heavy axions, which decay into photons, in the presence of interactions between superradiant states. We perform numerical and analytical studies to determine the number of axions produced by superradiance throughout the cosmic history and we estimate the resulting Milky Way's galactic center and extragalactic background photon fluxes and compare them with observational data. This way, we present a new cosmological axion production mechanism that represents a fraction of the dark matter.

Keywords: *Primordial Black Hole, Superradiant Instabilities, Superradiance, Quantum Chromodynamics Axion, Axion-Like-Particle, Dark Matter.*

Resumo

Os buracos negros são um ótimo laboratório para testar física de altas energias. Trabalhos recentes estudaram buracos negros que, através do fenómeno de instabilidades superradiantes, produziram na sua vizinhança uma nuvem constituída por axiões da cromodinâmica quântica ou partículas axiónicas. Nesta tese, analisamos alguns aspetos fenomenológicos da física subjacente a estes sistemas focando-nos nas suas aplicações à cosmologia e astrofísica.

Revemos a equação de Klein Gordon para um campo escalar massivo num espaço-tempo de Kerr, que leva a uma instabilidade superradiante de partículas associadas a este campo. Obtemos uma aproximação analítica para a solução da parte radial e interpretamos propriedades físicas da nuvem de partículas em analogia com o átomo de Hidrogénio. Posteriormente, propomos axiões como candidatos a estes sistemas e revemos o axião da cromodinâmica quântica e a física subjacente a esta partícula. De forma a completarmos estes sistemas, ponderamos buracos negros primordiais devido ao seu vasto intervalo de massas e apresentamos uma revisão ao mecanismo de formação destes objetos. De seguida, estudamos a dinâmica de sistemas constituídos por um buraco negro primordial em rotação, assumindo que os buracos negros primordiais são uma fração significativa da matéria escura, rodeado por uma nuvem de axiões pesados, que decaem em fotões, na presença de interações entre estados superradiantes. Efetuamos estudos numéricos e analíticos para determinar o número de axiões produzidos através de superradiância ao longo da história cósmica e estimamos os fluxos de fotões de fundo extragalático e do centro galáctico da Via Láctea e comparamos com dados observacionais. Desta forma, apresentamos um novo mecanismo cosmológico de produção de axiões que representam uma fração da matéria escura.

Palavras-Chave: *Buraco Negro Primordial, Instabilidades Superradiantes, Superradiância, Axião da Cromodinâmica Quântica, Partícula Axiónica, Matéria Escura.*

Agradecimentos

Para começar, gostaria de deixar o meu profundo agradecimento aos meus orientadores Professor Doutor João Rosa e Doutor Ricardo Zambujal Ferreira pelo apoio incansável e conhecimento partilhado que me foram fornecendo ao longo deste ano. O entusiasmo e eficácia com que partilharam a sua sabedoria impulsionou-me fortemente a querer aprender mais sobre diversos ramos da física.

Muito obrigado a todos os meus colegas e amigos que fiz nesta cidade, sem os quais o meu progresso seria certamente mais complicado.

Muito obrigado à minha Mãe, ao meu Pai e Irmão por todo o apoio e incentivo que me deram, tanto no meu trajeto pessoal como académico.

Muito obrigado à minha namorada, sem a qual não teria sequer iniciado esta caminhada, pela inesgotável fonte de força e perseverança.

Muito obrigado à minha estimada Avó que me ensinou a ler, escrever e a adorar matemática. Que descanses em paz e me esperes, até um dia me juntar a ti.

Contents

List of Figures **VII**

List of Tables **X**

List of Abbreviations **XI**

Notation and Conventions **XII**

1 Introduction **1**

2 Black hole superradiant instabilities **4**

2.1 Klein Gordon equation in Kerr spacetime 4

2.2 Solution and separation of variables 5

2.3 An approximation to the radial solution 6

2.4 Properties of the boson cloud and comparison with the Hydrogen atom 10

3 Axions **14**

3.1 Quantum anomalies 14

3.2 Solitons and instantons 15

3.3 Theta vacuum 17

3.4 Strong CP problem 18

3.5 Possible solution - axion 19

4 Primordial black holes as dark matter candidates **22**

4.1 Brief introduction to the Standard Model of Cosmology 22
4.2 Formation of PBHs 25
    4.2.1 Possible masses 25
    4.2.2 Formation mechanisms 26
    4.2.3 Abundance 26
    4.2.4 PBH mass as a function of the comoving wavenumber k 27
4.3 Inflation 29
4.4 Constraints on PBHs as DM candidates 32

5 Dynamics of primordial axion superradiant clouds 34

5.1 Dynamics of multiple superradiant states 34
    5.1.1 Equations that rule the dynamics 34
    5.1.2 Parameter space 36
    5.1.3 Numerical solution 38
    5.1.4 Analytical solution 41
    5.1.5 Axions outside the cloud 48
5.2 Bosenova 53

6 Electromagnetic signatures of superradiant axion clouds 55

6.1 Photon emission from bound axions 55
    6.1.1 Milky Way's galactic center photon flux 55
    6.1.2 Extragalactic background photon flux 59
6.2 Photon emission from free axions 62

7 Conclusion **65**

A - Details on Klein Gordon equation in Kerr spacetime **67**

B - Decay rate calculation **68**

B.1 Decay rate 68

B.2 Matrix element $\mathcal{M}$ 69

8 References **71**

List of Figures

1 Black hole's particle cloud sketch constructed from the radial and angular solutions. The cloud has an oblate toroidal shape. 11

2 Black hole's oblate toroidal 2D shape representing the major radius and the minor radius. . . 12

3 Constraints on the QCD axion mass. The constraints give an upper bound of 10^{-2} eV [32, 34] and a lower bound of 10^{-11} eV [33]. This gives an open window of $[10^{-11} - 10^{-2}]$ eV for the QCD axion mass range. 21

4 This figure represents the constrains of the content of the present-day universe resulting from the measurements of WMAP [43, 44]. 24

5 Hierarchy between the CMB/LSS scale and amplitudes and accessible scale by PBHs [53]. . . 28

6 The evolution of a comoving scale and comoving horizon as a function of $\ln a$. Modes with a constant comoving scale become super-horizon ($k < aH$) during inflation and then re-enter the horizon after inflation has ended when the comoving horizon, $\frac{1}{aH}$, grows. The red line corresponds to a large scale observed in the CMB, while the yellow line corresponds to a smaller scale that re-enters the horizon earlier [13]. 30

7 An example of an inflaton potential that has a SR regime and an USR regime which may produce a strong enough spectrum to form PBHs. The inflaton eventually leaves this inflection point moving to the global minimum which translates in the ending of inflation. Image taken from [13]. 32

8 All constraints on the fraction of DM in the form of PBHs: evaporation, microlensing, gravitational waves, PBH accretion and dynamical constraints. Attention is restricted to PBHs with $M_{PBH} \ll 10^7 M_\odot$ which could constitute the DM halos of small dwarf galaxies [14]. 33

9 Dominant axion self-interaction processes. Process a) is the annihilation of two axions in the 211 state leading to one axion in the 322 state and the other in an $m = 0$ non-superradiant mode that is absorbed by the black hole. Process b) is the annihilation of two axions in the 322 state leading to one axion in the 211 state and the other to escape the black hole's gravitational potential. Note that angular momentum m is conserved. 35

10 Regions where condition 1 and 2 are satisfied for ALPs. We consider black hole masses within the range where they may account for 100% of the DM and $f_a = 10^{10}$ GeV. Different values for the decay constant do not imply a significant change in the allowed parameter space since the f_a dependent condition scales logarithmically. We consider two extreme values of spin: In the left plot $\tilde{a} = 0.01$, and in the right plot $\tilde{a} = 0.99$. Different values of α are represented by straight lines with different colours as labelled. 37

11 Regions where condition 1 and 2 are satisfied for the QCD axion. There is no available region for the black hole masses within the $[10^{14} - 10^{18}]$ kg range. We extended this region until 10^{19} kg where it may represent 10% of the DM [14]. We consider two extreme values of spin: In the left plot $\tilde{a} = 0.01$, and in the right plot $\tilde{a} = 0.99$. Different values of α are represented by straight lines with different colours as labelled. 38

12 Numerical solution to the dynamics considering four different f_a values assuming $M = 10^{14}$ kg, $\tilde{a} = 0.01$, $\mu = 1$ keV and $|C_{a\gamma\gamma}| = 1$. 39

13 Left plot: Evolution of the ALP number in the 211 state for different f_a values. We observe a slight suppression of the ALP number which seems to slowly decrease, at an approximately constant rate, for $f_a \gtrapprox 10^{10}$ GeV. Right plot: N_2/f_a^2 fraction as a function of time. We consider a time interval ranging over the instant the system reaches an equilibrium until today. For $f_a \lessapprox 10^{10}$ GeV, the fraction reaches a constant value. For both cases we consider f_a values ranging over $[10^7 - 10^{12}]$ GeV with different colours as labelled. 40

14 Different regimes for the dynamics according to the decay constant value. Here we consider $\mu = 1$ keV, $\tilde{a} = 0.01$ and $M = 10^{14}$ kg. 43

15 Contrast between numerical and analytical solutions. We obtain a fairly reasonable matching for $f_a < 10^{11}$ GeV. For higher f_a values a change in the dynamics is required. 44

16 Numerical solution plot for $f_a = 10^{11}$ GeV (in red). We match the analytical axion number, once the superradiant condition is saturated (in blue), with the analytical axion number, once a significant amount of the black hole's angular momentum is extracted but has not yet saturated (in green). We plot both expressions starting at exactly the same point. 45

17 Numerical (red) *versus* analytical (black) plot for $f_a = 5.0 \times 10^{12}$ GeV. 46

18 Numerical solutions considering $\mu = 1$keV, $M = 10^{14}$kg and $\tilde{a} = 0.01$. 49

19 Different regimes for the dynamics of N_∞ according to the decay constant value considering $\mu = 1$ keV, $M = 10^{14}$ kg and $\tilde{a} = 0.01$. 51

20 Contrast between numerical and analytical solutions for the number of free axions considering $\mu = 1$ keV, $M = 10^{14}$ kg and $\tilde{a} = 0.01$. 52

21 Sketch of the geometry. 56

22 Experimental data of the intensity flux bound for the XMM-NuSTAR observation, for $[2-30]$ keV range X-ray particle decay. Plot taken from [64]. 58

23 Parameter space for which the galactic center photon flux estimate exceeds the observational data in the bosenova analysis, and is therefore excluded. Parameters assumed: $\tilde{a} = 0.9$, $|C_{a\gamma\gamma}| = 1$, $M = 10^{14}$ kg and $\alpha > 0.1$. 58

24 Extragalactic background photon flux. Plot and data taken from [68]. 60

25 Parameter space for which the extragalactic background photon flux exceeds the observational data in the bosenova analysis, and is therefore excluded. Parameters assumed: $\tilde{a} = 0.9$, $|C_{a\gamma\gamma}| = 1$, $M = 10^{14}$ kg and $\alpha > 0.1$. 62

26 Axion-photon coupling strength limits [69]. Constraints in green do not account axions as DM candidates. The X-ray bounds assume axions as DM candidates. 63

27 Parameter space for which theoretical flux estimates surpass observational data, and is therefore excluded. Parameters assumed: $M = 10^{14}$ kg, $\tilde{a} = 0.01$ and $|C_{a\gamma\gamma}| = 1$. The axion mass ranges over $\simeq [450-5000]$ eV (Figure 10). 64

28 Constraints on the axion-photon coupling from PBH superradiance (blue), assuming 100% of DM in 10^{14} kg and $\tilde{a} = 0.01$ PBHs. For comparison, we show existing constraints on axions in the keV mass range that are independent on the fraction of DM they account for, from globular clusters (green). 64

29 Feynman diagram of the decay of the axion into two photons with coupling strength $g_{a\gamma\gamma}$. . . 69

List of Tables

1 Value discrepancy for the numerical and analytical solutions for the 211 occupation number with $f_a = 10^6$ GeV. 47

2 Value discrepancy for the numerical and analytical solutions for the 211 occupation number with $f_a = 10^9$ GeV. 47

3 Value discrepancy for the numerical and analytical solutions for the 211 occupation number with $f_a = 10^{11}$ GeV. 47

4 Value discrepancy for the numerical and analytical solutions for the 211 occupation number with $f_a = 5.0 \times 10^{12}$ GeV. 48

5 Value discrepancy for the numerical and analytical solutions for N_∞ at $t = t_{uni}$ for various f_a values. 52

List of Abbreviations

PBH Primordial Black Hole
QFT Quantum Field Theory
RMS Root-Mean-Square
DM Dark Matter
DE Dark Energy
SR Slow Roll
USR Ultra Slow Roll
PDF Probability Density Function
NFW Navarro-Frenk-White
FLRW Friedmann-Lemâitre-Robertson-Walker
SMBH Supermassive Black Hole
ALP Axion-Like-Particle
QCD Quantum Chromodynamics
CMB Cosmic Microwave Background
WMAP Wilkinson Microwave Anisotropy Probe
PNG Pseudo-Nambu-Goldstone

Notation and Conventions

Throughout this thesis we use the following notations and conventions:

- Natural units $c = G = \hbar = 1$ are always assumed unless specifically mentioned;
- Einstein's summation notational convention is always assumed unless specifically mentioned;
- The signature used is (-,+,+,+);
- The Minkowski metric is written as $\eta_{\mu\nu}$ and non-Minkowski metrics are written as $g_{\mu\nu}$;
- Planck's mass is given by $M_p = \sqrt{\frac{\hbar c}{G}} \simeq 2.2 \times 10^{-8}$ kg. In sections 2, 3 and 4 we set it as $M_p = 1$ for a simpler analysis;
- We write $\log(x)$ as a base-10 logarithm and $\ln(x)$ as a base-e logarithm.

1 Introduction

One of the most fascinating breakthroughs in physics was Albert Einstein's General Relativity. Massive objects distort the fabric of spacetime, which is reflected in their dynamics. As the objects move, the curvature of spacetime changes accordingly providing a constant evolution of its geometry. Besides several important features, General Relativity, and more concretely the solutions to Einstein's field equations, predict the existence of objects with such a powerful gravitational pull that nothing can escape them. These objects are called black holes and they are characterized by three quantities: mass, M, charge, Q, and angular momentum, J. The geometry of the surrounding spacetime depends on these particular properties of the black hole. One particularly interesting solution to Einstein's field equations is the Kerr solution which describes a rotating uncharged axially-symmetric black hole. Our main interest in this particular solution is due to superradiance.

Superradiant scattering in classical systems was originally considered by Zel'dovich where the effects of scalar waves hitting a rotating absorbing cylinder were studied [1]. Zel'dovich concluded that below a given frequency of the incident wave, the scattered wave would be amplified and, by surrounding the object with a mirror, the system would become unstable. Some years after, Press and Teukolsky proposed the "Black Hole Bomb" [2, 3] where the rotating absorbing cylinder surrounded by mirrors was replaced by a Kerr black hole. The mirrors, which may be naturally mimicked with the introduction of a massive scalar field where the gravitational potential of the black hole traps the massive field, would reflect back and forth the scattered wave. Due to the presence of the rotating black hole, the amplitude of the wave would then grow exponentially and eventually become unstable. In this way, a cloud of light bosons that are copiously produced in quasi-bound states would be generated around the black hole at the expense of its angular momentum. In the presence of self-interactions there can be a non-trivial dynamics between the quasi-bound states [4].

Black holes are a great laboratory to probe high energy physics. Recent works studied systems of black holes with a surrounding cloud constituted by the Quantum Chromodynamics (QCD) axion or Axion-Like Particles (ALPs) [5, 6, 7]. The QCD axion is a Pseudo-Nambu-Goldstone (PNG) boson resulting from the spontaneous symmetry breaking of the anomalous $U(1)_{PQ}$ [8] symmetry postulated to solve the problem that emerges from the existence of the QCD theta vacuum, the strong CP problem [9]. ALPs are the PNG bosons emerging from the spontaneous symmetry breaking of more general $U(1)$ symmetries [10]. These particles may decay into photons, which will ultimately be relevant when estimating the electromagnetic flux emitted by these systems. In order for the superradiant phenomena to occur one requires that the superradiance condition[1], $4\mu M M_p^{-2} < \tilde{a}$, which involves the mass of the scalar field, μ, the black hole's mass, M, and its dimensionless spin, $\tilde{a}$, to be satisfied [11]. Since we will be considering particularly heavy particles we must ponder black holes with smaller masses than the ones resulting from stellar collapse.

Black holes are usually connected with the collapse of dying stars. Stephen Hawking introduced and studied a new possibility. He predicted that gravitationally collapsed objects of mass larger than the Planck mass $\simeq 10^{-8}$ kg could be formed as a result of large fluctuations in the density of the early universe [12]. These black holes formed in the early universe are named Primordial Black Holes (PBH). Their masses vary largely depending on their time of formation [13] and for a small window of masses they might represent 100% of the Dark Matter (DM) fraction [14]. These black holes may fulfill the requirements for the superradiant condition with heavy axions.

Our goal is to study the dynamics of a system made of a rotating PBH, assuming PBHs are a relevant fraction of the DM, surrounded by a cloud of heavy axions, which decay into photons, in the presence of interactions between superradiant states. Furthermore, theoretical estimates for the extragalactic background and galactic photon fluxes are compared with observational data providing signatures of these systems.

The outline of this thesis is as follows:

In section 2 we review the Klein Gordon equation for a massive scalar field in the Kerr spacetime and obtain an analytical approximation to the radial part of its solution. Furthermore, physical properties of the particle cloud are interpreted in analogy with the Hydrogen atom.

In section 3 we review the physics behind the QCD axion as well as the main ingredients that motivate its existence. Then, we study the QCD axion and elaborate on the requirements made by R. Peccei and H. Quinn in order to solve the strong CP problem.

In section 4 we review the main ideas that constitute the Cosmological Standard Model followed by an insight into the physics of PBHs and inflationary regimes which effectively predict the observations of the Cosmic Microwave Background (CMB) and may produce large enough density fluctuations on small physical scales in order to produce these objects.

In section 5 we study the dynamics of axion/ALP clouds around spinning PBHs, including the effects of axion self-interaction and decays. We perform numerical and analytical studies to determine the number of axions produced by superradiance throughout the cosmic history.

---

[1] For the dominant superradiant state in the small spin, $\tilde{a}$, and mass coupling constant, α, limit.

In section 6 we estimate the photon flux for these systems assuming PBHs to be a significant fraction of DM and the axion decay into photons. We cover two options for this calculation: the flux from the center of our galaxy and the extragalactic background flux. We end this section by comparing theoretical results with observational data.

2 Black hole superradiant instabilities

Superradiant scattering in classical systems was originally considered by Zel'dovich, who studied the effects of scalar waves hitting a rotating absorbing cylinder [1]. Furthermore, Zel'dovich concluded that below a given frequency of the incident wave, the scattered wave would be amplified. The frequency of this incident wave ω would have to satisfy what is now known as the superradiance condition that can be written as $\omega < m\Omega$, where Ω is the angular velocity of the object and m is the angular momentum quantum number. He also concluded that by surrounding the object with a mirror the system would become unstable.

Inspired by this idea, Press and Teukolsky took a step further and proposed the "Black Hole Bomb" [2, 3] where the rotating cylindrical absorbing object surrounded by mirrors was replaced with a Kerr black hole. The task of placing a mirror around a black hole may seem very much undoable but it turns out that this impossible task could be reproduced by considering a massive field scattering off a Kerr black hole [15]. The trapping of the low-frequency wave modes is ultimately achieved by the black hole's gravitational potential on which massive fields can be trapped in Hydrogen-like bound states (see *e.g* [11] and references therein). The potential would reflect back and forth the scattered wave. Due to the presence of the rotating black hole, the amplitude of the wave would then grow exponentially and eventually become unstable.

In this section we develop the Klein Gordon equation for a massive scalar field in the Kerr spacetime and obtain an analytical approximation for the radial part of the solution. Furthermore, we interpret the physical properties of the particle cloud in analogy with the Hydrogen atom.

2.1 Klein Gordon equation in Kerr spacetime

The Klein Gordon equation in the Kerr background for a scalar field Ψ of mass μ can be written as [16],

$$\frac{1}{\sqrt{-g}}\partial_\mu(\sqrt{-g}g^{\mu\nu}\partial_\nu\Psi) - \mu^2\Psi = 0 \tag{2.1}$$

where g is the determinant of the metric. In this background one needs to consider Kerr's metric which can be written in Boyer-Lindquist coordinates as [17],

$$ds^2 = -\Big(1 - \frac{2Mr}{\Sigma}\Big)dt^2 + \frac{\Sigma}{\Delta}dr^2 + \Sigma d\theta^2 + \\ + \Big(r^2 + a^2 + \frac{2Mra^2\sin^2\theta}{\Sigma}\Big)\sin^2\theta d\phi^2 - \frac{4Mra\sin^2\theta}{\Sigma}dtd\phi \tag{2.2}$$

where,

$$a = \frac{J}{M} \tag{2.3}$$

$$\Sigma = r^2 + a^2\cos^2\theta \tag{2.4}$$

$$\Delta = r^2 - 2Mr + a^2 \tag{2.5}$$

Here M and J are the mass and angular momentum of the black hole, respectively. The event horizon is determined by the outermost location where the coefficient of dr^2 diverges which corresponds to a coordinate singularity at $\Delta = 0$,

$$r_+ = M + \sqrt{M^2 - a^2} \tag{2.6}$$

One then concludes that the event horizon exists only in the case where $a \leq M$. This conclusion is ensured by the cosmic censorship hypothesis [18] which states that black holes always form with $J \leq M^2$, meaning that singularities are protected by a horizon. Computing this metric in the Klein Gordon equation and after some algebra (See Appendix A.1),

$$\Bigg(\frac{1}{\Delta}\Big((r^2+a^2)^2 - \Delta a^2\sin^2\theta\Big)\partial_t^2 - \partial_r(\Delta\partial_r) - \frac{1}{\sin\theta}\partial_\theta(\sin\theta\partial_\theta) + \\ - \frac{1}{\Delta\sin^2\theta}(\Delta - a^2\sin^2\theta)\partial_\phi^2 - \frac{2a}{\Delta}\Big(\Delta - (r^2+a^2)\Big)\partial_\phi\partial_t + \Sigma\mu^2\Bigg)\Psi = 0 \tag{2.7}$$

2.2 Solution and separation of variables

To solve this equation one assumes that its solution can be separated as [11],

$$\Psi = \Psi(\mathbf{r}, t) = R(r)S(\theta)e^{im\phi}e^{-i\omega t} \tag{2.8}$$

Inserting this into equation 2.7 one may notice that it is separable into two independent differential equations,

$$\frac{1}{\sin\theta}\partial_\theta\Big(\sin\theta\partial_\theta S(\theta)\Big) + S(\theta)\Big(\lambda_{l,m} + a^2(\omega^2 - \mu^2)\cos^2\theta - \frac{m^2}{\sin^2\theta}\Big) = 0 \tag{2.9}$$

$$\Delta\partial_r\Big(\Delta\partial_r R(r)\Big) + R(r)\Big(\omega^2(r^2+a^2)^2 - r^2\mu^2\Delta + a^2m^2 - 4Ma\omega mr - (\omega^2a^2 + \lambda_{l,m})\Delta\Big) = 0 \tag{2.10}$$

Equation 2.9 has as solutions the oblate spheroidal harmonics functions $S_{l,m}(ic, \cos\theta)$ with eigenvalues $\lambda_{l,m}$ where l, m are integers such that $|m| \leq l$ [19]. The $\lambda_{l,m}$ eigenvalue is given by,

$$\lambda_{l,m} = l(l+1) + \sum_{k=1}^{+\infty} C_{klm}(aq)^{2k} \tag{2.11}$$

where q is defined as $q = \sqrt{\mu^2 - \omega^2}$ and C_{klm} is a set of coefficients [20]. In the non-relativistic regime (small scalar field mass) $aq \ll 1$, one may then approximate the latter equation as,

$$\lambda_{l,m} \simeq l(l+1) \tag{2.12}$$

As for equation 2.10, it represents the radial differential equation, which does not have an exact analytical solution and will be further explored in the next subsection.

2.3 An approximation to the radial solution

Even though the radial equation does not have an exact analytical solution, one can use Starobinsky's matching procedure which consists in dividing the exterior of the black hole into two overlapping regions [21]. It is easier to first re-write equation 2.10 in a more convenient way by using a set of dimensionless coordinates [11],

$$x = \frac{r - r_+}{r_+} \qquad \text{and} \qquad \tau = \frac{r_+ - r_-}{r_+} \tag{2.13}$$

where $r_- = M - \sqrt{M^2 - a^2}$ is the Cauchy horizon. Now it yields,

$$x^2(x+\tau)^2\partial_x^2 R + x(x+\tau)(2x+\tau)\partial_x R + V(x)R = 0 \tag{2.14}$$

where $V(x)$,

$$\begin{aligned} V(x) = &\Big(x(x+\tau)\bar{\omega} + (2-\tau)(\bar{\omega} - m\bar{\Omega})\Big)^2 + \\ &+ x(x+\tau)\Big((\tau-1)\bar{\omega}^2 + 2(2-\tau)m\bar{\omega}\bar{\Omega} - \bar{\mu}^2(x+1)^2 - \lambda\Big) \end{aligned} \tag{2.15}$$

where a set of dimensionless quantities, identified by a bar on top of the respective quantity, *e.g*, $\bar{\mu} = r_+\mu$, was used. Here Ω represents the angular velocity of the black hole at the event horizon [11],

$$\Omega = \frac{a}{r_+^2 + a^2} = \frac{\tilde{a}}{2r_+} \tag{2.16}$$

where the dimensionless spin parameter $\tilde{a}$ is given by,

$$\tilde{a} = \frac{a}{M} \qquad 0 < \tilde{a} < 1 \tag{2.17}$$

As previously mentioned, one may obtain an approximate analytical solution by dividing the exterior of the black hole into two overlapping regions: a near region defined by $x \ll \frac{l}{\omega}$ and a far region $x \gg 1$. One may solve it analytically by matching the solutions in the overlapping domain of validity $1 \ll x \ll \frac{l}{\omega}$ [11, 21]. In the small mass coupling limit, $\bar{\omega} \simeq \bar{\mu} \ll 1$. Thus, in the near region equation 2.14 can be written as,

$$x^2(x+\tau)^2\partial_x^2 R + x(x+\tau)(2x+\tau)\partial_x R + \Big(\Big[(2-\tau)(\bar{\omega} - m\bar{\Omega})\Big]^2 - x(x+\tau)\lambda\Big) R = 0 \tag{2.18}$$

The boundary conditions are obtained as follows: one requires the wave to travel into the black hole and never outwards. In this sense, and using Starobinsky's procedure, this equation has an analytical solution [11, 20, 21],

$$R_N(x) = A\Big(\frac{x}{x+\tau}\Big)^{-\frac{i\bar{\varpi}}{\tau}} {}_2F_1\Big(l+1, -l, 1 - \frac{2i\bar{\varpi}}{\tau}, -\frac{x}{\tau}\Big) \tag{2.19}$$

where $\bar{\varpi} = (2-\tau)(\bar{\omega} - m\bar{\Omega})$ and ${}_2F_1(a,b,c,x)$ is the hypergeometric function. In the limit $x \gg \tau$, and using the properties of the hypergeometric function in this asymptotic limit ($|\frac{x}{\tau}| \gg l$), one finds an approximate solution of the form [11, 20],

$$R_N(x) \simeq A\Gamma\Big(1 - \frac{2i\bar{\varpi}}{\tau}\Big)\Bigg[\frac{\Gamma(2l+1)}{\Gamma(l+1)\Gamma(l+1-\frac{2i\bar{\varpi}}{\tau})}\Big(\frac{x}{\tau}\Big)^l + \frac{\Gamma(-2l+1)}{\Gamma(-l)\Gamma(-l-\frac{2i\bar{\varpi}}{\tau})}\Big(\frac{x}{\tau}\Big)^{-l-1}\Bigg] \tag{2.20}$$

As for the far region, equation 2.14 reduces to,

$$x^2\partial_x^2 R + 2x\partial_x R + (\bar{q}^2 x^2 + 2\bar{q}\nu x - \lambda) R = 0 \tag{2.21}$$

where,

$$\nu = \Big(\frac{2-\tau}{2}\Big)\Big(\frac{\bar{\omega}^2 - \bar{q}^2}{\bar{q}}\Big) \tag{2.22}$$

This differential equation has an asymptotically regular solution in terms of the confluent hypergeometric function $U(a,b,x)$,

$$R_F(x) = Bx^l e^{-\bar{q}x} U(l+1-\nu, 2l+2, 2\bar{q}x) \tag{2.23}$$

In the far limit, $\bar{q}x \ll 1$, this equation has an approximate solution of the form [11, 20],

$$R_F(x) \simeq \frac{B\pi}{\sin\left(2\pi(l+1)\right)}\Bigg[\frac{x^l}{\Gamma(-\nu-l)\Gamma(2l+2)} - (2\bar{q})^{-1-2l}\frac{x^{-1-l}}{\Gamma(l+1-\nu)\Gamma(-2l)}\Bigg] \tag{2.24}$$

Having found the solutions in both regions, one can match the near region solution with the far region solution since in this domain they overlap. Matching the coefficients of x^l and x^{-l-1} yields,

$$\frac{\Gamma(2l+2)\Gamma(-\nu-l)}{\Gamma(l+1-\nu)\Gamma(-2l)} = -(2\bar{q}\tau)^{2l+1}\frac{\Gamma(l+1)\Gamma(-2l-1)\Gamma(l+1-\frac{2i\bar{\varpi}}{\tau})}{\Gamma(2l+1)\Gamma(-l)\Gamma(-l-\frac{2i\bar{\varpi}}{\tau})} \tag{2.25}$$

In the non-relativistic limit, $\bar{q} \ll 1$, the right-hand side of the latter equation is $\simeq 0$. Thus, the matching gives,

$$\frac{1}{\Gamma(l+1-\nu)} = 0 \tag{2.26}$$

For any negative integer value of the argument of the gamma function one obtains infinity. Let n' be a positive integer,

$$l+1-\nu = -n' \leftrightarrow \nu = n'+1+l \leftrightarrow \nu = n \tag{2.27}$$

where n' is the number of the radial function.

In order to get the bound state frequency one can recall equation 2.22 in order to expand the frequency as $\bar{\omega} = \bar{\omega}^{(0)} + \delta\bar{\omega}$. After some algebra and Taylor expanding terms up to first order, the bound state frequency results in the Hydrogen-like spectrum,

$$\bar{\omega} = \bar{\mu}\Big(1 - \frac{(\mu M)^2}{n^2}\Big)^{1/2} \simeq \bar{\mu}\Big(1 - \frac{(\mu M)^2}{2n^2}\Big) \tag{2.28}$$

and,

$$\bar{q} = \sqrt{\bar{\mu}^2 - \bar{\omega}^2} \simeq \frac{(\mu M)\bar{\mu}}{n} \tag{2.29}$$

This expansion is useful because unstable particles are characterized by a complex frequency which is ultimately the decay width/growth rate[2] of the particle. One may consider the frequency to have the form $\omega = \omega_R + i\omega_I$. Now, and to determine whether the mode is superradiant, one computes the sub-leading imaginary part of the bound state by expanding the left-hand side of equation 2.25 perturbatively and matching it with the right-hand side with the leading order result $\bar{\omega}^{(0)}$. Using some properties of the gamma function [11] and after some algebra the right-hand side of the mentioned equation becomes,

$$\frac{i(l!)^2}{(2l+1)!(2l)!}\Big(\frac{M\omega_1}{\tau}\Big)\prod_{k=1}^{l}\Big(k^2 + 16\Big(\frac{M\omega_1}{\tau}\Big)^2\Big)\Big(\frac{r_+ - r_-}{r_+ + r_-}\Big)^{2l+1} 2^{4l+3}\Big(\frac{(\mu M)^2}{n}\Big)^{2l+1} \tag{2.30}$$

where $\omega_1 = \omega - m\Omega$. As for the left hand side,

$$-\frac{(2l+1)!(n-l-1)!(2l)!}{(n+l)!}\delta\nu \tag{2.31}$$

Recall that to leading order $\bar{\omega} = \bar{\mu} - \frac{\bar{\mu}}{2}(\frac{\mu M}{n})^2$, with $n \equiv \nu$, which means that,

$$\delta\nu = \frac{n^3}{\mu(\mu M)^2}\delta\omega \tag{2.32}$$

---

[2] Depending whether the sign is negative or positive, respectively.

Putting all pieces together, one can get the sub-leading imaginary part of the bound state frequency. After some algebra,

$$\omega_I M = -\frac{1}{2}\Big(\frac{l!}{(2l+1)!(2l)!}\Big)^2 \frac{(l+n)!}{(n-l-1)!}\frac{4^{2l+2}}{n^{2l+4}}\times$$
$$\times \prod_{k=1}^{l}\Big(k^2+16\Big(\frac{M\omega_1}{\tau}\Big)^2\Big)\Big(\frac{M\omega_1}{\tau}\Big)(\mu M)^{4l+5}\Big(\frac{r_+-r_-}{r_++r_-}\Big)^{2l+1} \tag{2.33}$$

Looking at the initial anzats (equation 2.8) one concludes that if the imaginary part of the frequency is positive one gets a positive exponential, which means an exponential amplification, leading to the superradiant instability. So, a mode is unstable for $\omega_I > 0$, when the superradiant condition $\varpi < 0$ or equivalently $\omega_R < m\Omega$ is satisfied. In the small mass limit $\omega_R \simeq \mu$ and for the fastest growing state [11, 22], which is the $2p$ state ($n=2, l=1, m=1$), the superradiant condition yields,

$$\mu < \frac{\tilde{a}}{2M(1+\sqrt{1-\tilde{a}^2})} \quad\Longrightarrow\quad \mu M < \frac{1}{2} \tag{2.34}$$

The number of particles has an exponential growth of the form [11],

$$|\Psi|^2 \propto e^{\Gamma_s t} \tag{2.35}$$

where we defined the superradiant rate as $\Gamma_s = 2\omega_I$. This is the quantity of interest when making this analysis.

Of course the analytical solution of equation 2.14 is only an approximation. To obtain a better result one needs to apply numerical methods in order to compute the spectrum of quasi-bound states. Such studies have been done for instance in [11] where the radial equation was integrated from the horizon up to large distances. Quasi-bond states were then extrapolated by minimizing the solution in the complex frequency plane. In the same work it is concluded that analytical results deviate significantly from numerical results for $\mu M \gtrapprox 0.1$ and for large values of the black hole's spin $\tilde{a}$. Using the same reference and in order to get better results we extract an improved analytical expression[3] which will be used in future calculations when considering high spins. For the fastest growing mode the improved analytical expression yields [11],

$$\omega_I M = -\frac{1}{12}\Big(\frac{M\omega_1}{\tau}\Big)(\mu M)^9\Big(\frac{r_+-r_-}{r_++r_-}\Big)^3\times$$
$$\times\Big(1+\frac{\big(2\mu M(1+\sqrt{1-\tilde{a}^2})-\tilde{a}\big)^2}{1-\tilde{a}^2}\Big)\Big(1+\frac{3}{2}\frac{\tilde{a}^{9/5}}{\sqrt{1-\tilde{a}}}\Big(\frac{\mu}{\Omega}\Big)^6\Big) \tag{2.36}$$

---

[3] The starting point to this expression was the analytical approximation exactly obtained here. From equation 2.33 the correction was obtained by trial and error aiming to a result as close as possible to the numerical result.

2.4 Properties of the boson cloud and comparison with the Hydrogen atom

There are plenty of similarities between the system consisting of light bosons being copiously produced in quasi-bound states around a Kerr black hole and an electron "orbiting" the nucleus of the Hydrogen atom forming a bound state. One may then obtain and interpret some physical properties of the cloud such as its volume and radius in perfect analogy with the Hydrogen atom.

The time independent Schrödinger equation yields [23],

$$\hat{H}\Psi = E\Psi \tag{2.37}$$

where the Hamiltonian $\hat{H}$ for the Hydrogen atom is given by,

$$\hat{H} = -\frac{\nabla^2}{2\mu} - \frac{e^2}{4\pi\epsilon_0 r} \tag{2.38}$$

where μ is the reduced mass of the proton/electron system and r is the radial position under the Born-Oppenheimer approximation that assumes the nucleus approximately fixed. Taking as an anzats [23],

$$\Psi_{n,l,m_l}(r,\theta,\phi) = R_{n,l}(r)Y_l^{m_l}(\theta,\phi) \tag{2.39}$$

one can separate this equation according to the variable dependence, with the separation constant[4] $\lambda = l(l+1)$,

$$r^2\partial_r^2 R + 2r\partial_r R + \Big(2\mu r^2 E + \frac{\mu e^2 r}{2\pi\epsilon_0} - l(l+1)\Big)R = 0 \tag{2.40}$$

$$\frac{1}{\sin\theta}\partial_\theta(\sin\theta\partial_\theta Y) + \frac{1}{\sin^2\theta}\partial_\phi^2 Y + l(l+1)Y = 0 \tag{2.41}$$

It is now clear that the radial part (equation 2.40) has the exact same form as equation 2.21 which corresponds to the far region of the black hole. As for the angular part (equation 2.41) it is similar to equation 2.9. In this case it corresponds to the spherical harmonics, whereas for the black hole it corresponds to the equation of the spheroidal harmonics which has a slightly different form [20].

For the Hydrogen case, the wave functions are well studied [23] and one can check what is the form of the wave function for a $2p$ state. In order to get a pictorial view of the black hole's cloud we constructed the probability density of particles surrounding the black hole with the help of *Wolfram Mathematica*. We constructed this probability density as,

---

[4] The value for this constant can be obtained if one solves the angular part which can be checked in various physics books *e.g* [24].

$$|\Psi|^2 r^2 \sin\theta \tag{2.42}$$

where Ψ is the solution as depicted by equation 2.8 for the wave function considering the radial function in the far region of the black hole. The 3D plot is as shown in Figure 1. The cloud has an oblate[5] toroidal shape. As stated, the eigenstates of our system are Hydrogen-like with a redefined "Bohr radius", r_0, and a redefined "fine structure constant", α. In perfect analogy with the Hydrogen atom, the radial function can be expressed as [7],

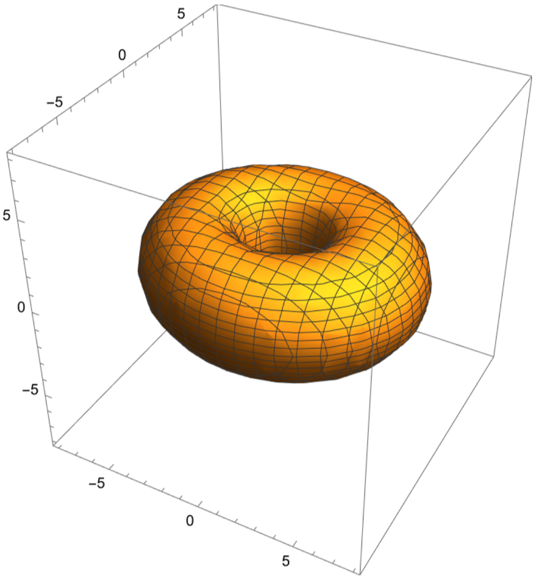

Figure 1: Black hole's particle cloud sketch constructed from the radial and angular solutions. The cloud has an oblate toroidal shape.

$$R_{n,l} \propto r^{2l+1} L^{2l+1}_{n-l-1}(2qr)e^{-qr} \tag{2.43}$$

and from equation 2.29,

$$R_{n,l} \propto r^{2l+1} L^{2l+1}_{n-l-1}\left(\frac{2r}{nr_0}\right)e^{-\frac{r}{nr_0}} \tag{2.44}$$

where L^{2l+1}_{n-l-1} is the associated Laguerre polynomial [20] where we defined the "Bohr radius" as,

$$r_0 = \frac{1}{\alpha\mu} \simeq 10^{-5}\left(\frac{4\times10^{-4}}{\alpha}\right)\left(\frac{\text{keV}}{\mu}\right)\text{cm} \tag{2.45}$$

---

[5] It is oblate due to the spheroidal harmonics. In contrast, if we had considered the spherical harmonics we would obtain a perfectly spherical shape.

and the “fine structure constant” as,

$$\alpha = \frac{\mu M G}{\hbar c} \tag{2.46}$$

where, for reference, we explicitly included all the missing constants. This definition provides an elegant way of expressing the superradiant condition as depicted by equation 2.34, which, for extremal black holes can be written as,

$$\alpha < \frac{1}{2} \tag{2.47}$$

There are still two important quantities to take into consideration: the major radius and the minor radius of the cloud's oblate toroidal shape, as depicted in Figure 2.

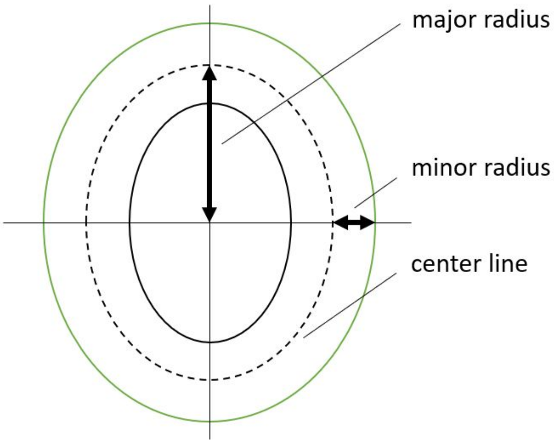

Figure 2: Black hole's oblate toroidal 2D shape representing the major radius and the minor radius.

The size of the major radius may be obtained via the expectation value of the radial coordinate for each state [16],

$$\langle r_{n,l,m} \rangle = \frac{\int_0^\infty dr r^3 R_{n,l}^2(r)}{\int_0^\infty dr r^2 R_{n,l}^2(r)} \tag{2.48}$$

For the $2p$ state,

$$R_{2,1} \propto r L_0^3 \left(\frac{r}{r_0}\right) e^{-\frac{r}{2r_0}} \tag{2.49}$$

Thus,

$$\langle r_{2,1,1} \rangle = 5 r_0 \tag{2.50}$$

For the radius of the cloud, that is the minor radius, one can estimate it by measuring the uncertainty of the observable r as a spread of results around $\langle r \rangle$,

$$\Delta r = \sqrt{\langle r^2 \rangle - \langle r \rangle^2} \tag{2.51}$$

which gives,

$$\langle r^2_{2,1,1}\rangle = 30r_0^2 \quad \text{and} \quad \Delta r = \sqrt{5}r_0 \tag{2.52}$$

One may now estimate the root-mean-square (RMS) of the velocity. Considering [23],

$$\langle H\rangle = \frac{\langle |v|^2\rangle\mu}{2} + \langle V(r)\rangle \tag{2.53}$$

In analogy with the Hydrogen atom, $V(r) = -\frac{\alpha}{r}$ where α is now the redefined fine structure constant and for the $2p$ state, $\langle H\rangle = E_2 = -\frac{\mu\alpha^2}{8}$. This translates into,

$$-\frac{\mu\alpha^2}{8} = \frac{\langle |v|^2\rangle\mu}{2} - \alpha\Big\langle\frac{1}{r}\Big\rangle \tag{2.54}$$

where $\Big\langle\frac{1}{r}\Big\rangle = \frac{\mu\alpha}{4}$ can be obtained in a similar way as the mean square radius. So the RMS of the velocity yields,

$$\sqrt{\langle |v|^2\rangle} = \frac{\alpha}{2} \tag{2.55}$$

For the purposes of this work $\alpha \ll 1$, where one immediately concludes that the velocity of the particles is non-relativistic.

Furthermore, one can estimate where the cloud is located by working out the quotient,

$$\frac{r_0}{r_+} = \frac{1}{\alpha^2(1+\sqrt{1-\tilde{a}^2})} \quad \Longrightarrow \quad r_0 \gg r_+ \tag{2.56}$$

meaning that the cloud is located far away from the horizon and curvature effects may be neglected within the cloud.

Finally, one can estimate the volume of the cloud. According to its toroidal shape and considering the volume of a torus which is given by,

$$V_{\text{torus}} = 2\pi^2 r_M^2 r_m \tag{2.57}$$

where r_M is the major radius and r_m is the minor radius, yielding,

$$V_{\text{torus}} = \frac{50\pi^2}{\alpha^3\mu^3} \simeq 10^{-45}\Big(\frac{4\times10^{-4}}{\alpha}\Big)^3\Big(\frac{\text{keV}}{\mu}\Big)^3 \text{cm}^3 \tag{2.58}$$

3 Axions

The QCD axion is a PNG boson resulting from the spontaneous symmetry breaking of the anomalous $U(1)_{PQ}$ symmetry first formulated by the physicists Roberto Peccei and Hellen Quinn in 1977 [8]. More general axions, named ALPs, are the PNG bosons emerging from the spontaneous symmetry breaking of more general $U(1)$ symmetries [10]. The physics underlying these beyond the Standard Model particles is intriguing and requires a closer look. Here, we try both to understand the physics behind these particles as well as capture the main ingredients that motivate their existence. We will focus mainly on the QCD axion throughout this section.

3.1 Quantum anomalies

Quantum anomalies are important in the understanding of the QCD axion in the sense that it is the $U(1)_{PQ}$ anomaly that provides the axion's mass. The main goal of this subsection is therefore to understand where the anomaly comes from. To do so, one may consider a massless Dirac field Ψ with charge $Q = +1$. The Lagrangian is [25],

$$\mathcal{L} = i\bar{\Psi}\gamma^{\mu}D_{\mu}\Psi - \frac{1}{4}F^{a\mu\nu}F^{a}_{\mu\nu} \tag{3.1}$$

where D_μ is the covariant gauge derivative defined as $D_\mu = \partial_\mu - igA_\mu$ where g is a coupling constant and A_μ the gauge field. The non-abelian field strength tensor, $F^a_{\mu\nu}$, is defined as $F^a_{\mu\nu} = \partial_\mu A^a_\nu - \partial_\nu A^a_\mu + gf^{abc}A^b_\mu A^c_\nu$ where f^{abc} are the structure constants. For simplicity, we consider the gauge field as a fixed background quantity to be integrated afterwards. In these terms, the path integral over the Dirac field has the following form,

$$Z(A) = \int \mathcal{D}\bar{\Psi}\mathcal{D}\Psi e^{iS(A)} \tag{3.2}$$

where $S(A) = \int d^4xi\bar{\Psi}\gamma^{\mu}D_{\mu}\Psi$ is the action and $\mathcal{D}\bar{\Psi}\mathcal{D}\Psi$ is the integration measure where the condensed notation was used, $\prod_{t,\mathbf{x}} d\Psi(t,\mathbf{x}) \equiv \mathcal{D}\Psi$. Considering a local axial $U(1)$ transformation of the Dirac field,

$$\Psi(x) \to e^{-i\alpha(x)\gamma_5}\Psi(x) \tag{3.3}$$

$$\bar{\Psi}(x) \to \bar{\Psi}(x)e^{-i\alpha(x)\gamma_5} \tag{3.4}$$

which transforms the action, after integrating by parts, as,

$$S(A) \to S(A) - \int d^4x\alpha(x)\partial_\mu J^\mu_a(x) \tag{3.5}$$

Naively, one could consider the integration measure $\mathcal{D}\bar{\Psi}\mathcal{D}\Psi$ invariant under such a transformation, which would lead to a conserved current and hence the validation of Noether's Theorem, $\partial_\mu J^\mu_a(x) = 0$. But this assumption would be incorrect. In fact, the integration measure is not invariant under such a transformation and it transforms as[6],

$$\mathcal{D}\bar{\Psi}\mathcal{D}\Psi \to \mathcal{D}\bar{\Psi}\mathcal{D}\Psi e^{-\frac{ig^2}{16\pi^2}\int d^4x\alpha(x)\varepsilon^{\mu\nu\rho\tau}Tr(F_{\mu\nu}(x)F_{\rho\tau}(x))} \tag{3.6}$$

which translates into a transformation of the path integral as,

$$Z(A) \to \int \mathcal{D}\bar{\Psi}\mathcal{D}\Psi e^{i(S(A)-\int d^4x\alpha(x)[\frac{g^2}{16\pi^2}\varepsilon^{\mu\nu\rho\tau}Tr(F_{\mu\nu}(x)F_{\rho\tau}(x))+\partial_\mu J^\mu_a(x)])} \tag{3.7}$$

where one concludes that for the path integral to be invariant under the axial transformation from equations 3.3-3.4 the quantity in between square brackets in equation 3.7 must vanish (so that the path integral is exactly the same as the original expressed in equation 3.2). By doing so, one gets an anomalous divergence of the axial current,

$$\partial_\mu J^\mu_a(x) = -\frac{g^2}{16\pi^2}\varepsilon^{\mu\nu\rho\tau}Tr(F_{\mu\nu}(x)F_{\rho\tau}(x)) \tag{3.8}$$

Therefore, an anomaly is a classical symmetry that is not a symmetry of the quantum path integral.

3.2 Solitons and instantons

Having the concept of quantum anomalies understood one can proceed to the next topic. Instantons play a major role in the axion discussion because it is due to them that the axion acquires a potential and hence a mass. Ultimately, they make the integration measure non-invariant under a given chiral transformation, which leads to an effective anomaly that then generates the mass of the resulting Goldstone boson. But first, let us introduce the concept of soliton. Consider a gauge field theory in D spatial dimensions with a scalar field Φ. The energy of a localized time-independent solution is given by [26],

$$E = \int d^Dx\Big[\frac{1}{2}(D_i\Phi)^2 + \frac{1}{4}F^a_{ij}F^{aij} + V(\Phi)\Big] \tag{3.9}$$

where D_i is the usual covariant gauge derivative, and F^a_{ij} is the non-abelian field strength tensor. One can then separate the integral in equation 3.9 into a sum of three quantities for each component of the latter equation and the localized solution can be written as,

$$E = I_K + I_G + I_V \tag{3.10}$$

---

[6] The complete calculation is extensive and will not be performed here. For more technical details check [25].

where the potential is positive defined such that the kinetic, I_K, gauge, I_G, and potential, I_V, terms are also positive. Under the transformations,

$$\Phi(x) \rightarrow \Phi(\lambda x) \tag{3.11}$$

$$A_i^a(x) \rightarrow \lambda A_i^a(\lambda x) \tag{3.12}$$

where λ is a positive defined parameter, one gets the following energy configuration,

$$E = \lambda^{2-D} I_K + \lambda^{4-D} I_G + \lambda^{-D} I_V \tag{3.13}$$

In order to find a stable solution one requires two conditions,

$$1. \qquad \left.\frac{dE}{d\lambda}\right|_{\lambda=1} = 0 \tag{3.14}$$

$$2. \qquad \left.\frac{d^2E}{d\lambda^2}\right|_{\lambda=1} > 0 \tag{3.15}$$

Requiring also that this solution is finite one obtains a solution called a soliton: a solution of the classical field equations with a finite energy density that is localized in space, and that does not change its shape with time. Furthermore, one can draw two conclusions:

- In the absence of gauge fields ($I_G = 0$) there are only stable solutions for $D = 1$, which is a consequence of Derrick's Theorem [26]: In the absence of gauge fields there are no spatially localized, finite energy and time-independent solutions in more than 1D. The problem arises from the divergence of the gradient of energy at large distances;
- In the absence of scalar fields ($I_K = I_V = 0$) there are only solutions for $D = 4$. Afterwards, if one performs a Wick Rotation, one gets a non-trivially topological solution named an instanton which is characterized by a finite action and localized in spacetime.

Following the line of thought of the latter conclusion, and in order to get the instanton solution, consider a pure gauge theory in which the Lagrangian is invariant under transformations of a non-abelian gauge group G. The Euclidean action is [27],

$$S = \frac{1}{4g^2} \int d^4x F_{\mu\nu}^a F_{\mu\nu}^a \tag{3.16}$$

For the action to be finite one requires the field strength tensor to vanish at spatial infinity ($F_{\mu\nu}^a \rightarrow 0$ at $|\mathbf{x}| \rightarrow \infty$). In this limit the gauge field, A_μ^a, must approach a pure gauge configuration [27],

$$A_\mu^a(\mathbf{x}) \rightarrow \frac{i}{g}(\partial_\mu U(\hat{\mathbf{x}}))U^{-1}(\hat{\mathbf{x}}) \quad \text{at} \quad |\mathbf{x}| \rightarrow \infty \tag{3.17}$$

where $U(\hat{\mathbf{x}})$ is an element of the gauge group G. This equation maps S^3_∞ to the group manifold G. One requires such mapping because configurations of finite action depend on their value at spatial infinity and one wants to map the spatial infinity to the set of vacua. Classes of such mappings are topologically distinguishable and define the third homotopy group of the group manifold G. For QCD, where $G \equiv SU(3)$, this homotopy group is non-trivial. The topological distinguishability of the vacuum of QCD is classified by an integer element of $\mathbb{Z}$ and characterized by a topologically invariant quantity called winding number. For $SU(2)$ in 4D it can be written[7] as an integral over the Euclidean space [27],

$$\nu = \frac{g^2}{32\pi^2} \int_{E_4} d^4x F^a_{\mu\nu} \tilde{F}^a_{\mu\nu} \tag{3.18}$$

where $\tilde{F}^a_{\mu\nu} = \frac{1}{2}\varepsilon_{\mu\nu\alpha\sigma} F^{a\alpha\sigma}$. This is a topological invariant in the sense that it is invariant under changes of coordinates[8] and under applied deformations. If one were to consider the gauge group to be the abelian group $U(1)$ any mapping from S^3 to $U(1)$ would be continuously deformed into the trivial map, that is, S^3 mapped to a single point. So the winding number is a quantity exclusive to non-abelian theories.

3.3 Theta vacuum

According to these instanton solutions, one could consider describing the QCD vacuum by the winding number which corresponds to the instanton configuration with index $\nu = |p\rangle$. But this would not be a good vacuum because it is not gauge invariant. A gauge transformation of winding number p' changes the ground state as $|p\rangle \to |p'\rangle$. The way to solve this problem is to construct the vacuum as a superposition of all possible winding numbers [8, 9],

$$|\theta\rangle = \sum_{p=-\infty}^{\infty} e^{ip\theta} |p\rangle \tag{3.19}$$

Calculating the vacuum-to-vacuum transition amplitude,

$$\langle\theta'|e^{-iHt}|\theta\rangle = \delta(\theta' - \theta) \int D_A e^{-\int d^4x \mathcal{L} + i\nu\theta} \tag{3.20}$$

where the delta function ensures that this is a good vacuum because it only allows one vacuum and no transitions between different vacua. Along with this choice of vacuum, one term is added to the action. Notice the $i\nu\theta$ term in the latter equation where ν corresponds to the configuration of the winding number given by equation 3.18. So QCD is described by the usual action plus a term resulting from the winding number. The full action yields,

---

[7] This result is also valid for SU(N). This is a consequence of Raoul Bott's theorem that states that any continuous mapping of S^3 into a group manifold G can be continuously deformed into a mapping into a SU(2) subgroup of G.

[8] Notice that the indices in the field strength tensor are lowered by the anti-symmetric Levi-Civita tensor and not by the usual metric, which means that it is independent of the metric.

$$S_{eff} = S_{QCD} + \frac{g^2\theta}{32\pi^2}\int d^4x G^a_{\mu\nu}\tilde{G}^{a\mu\nu} \tag{3.21}$$

which represents a new term in the Lagrangian of the form,

$$\mathcal{L}_\theta = \frac{g^2\theta}{32\pi^2}G^a_{\mu\nu}\tilde{G}^{a\mu\nu} \tag{3.22}$$

Since this term is a total derivative it does not impact the QCD theory at the perturbative level as one knows it in the sense that neither the Feynman rules nor the equations of motion are affected by it. This term does not violate QCD symmetries (Poincaré symmetry, $SU(3)$ gauge symmetry, CPT invariance...) but it violates parity, time reversal and conserves charge conjugation, so it violates CP.

3.4 Strong CP problem

The explicit violation of CP leads to an electric dipole moment of the neutron. The theta term induces an eletric dipole moment to the neutron of the form [28],

$$|d_n| \simeq \frac{e\theta m_q}{M_N^2} \simeq 3.6\times 10^{-16}\theta\, e\,\text{cm} \tag{3.23}$$

Experimental data gives an upper bound on this quantity [29],

$$|d_n| < 2.9\times 10^{-26}\, e\,\text{cm} \tag{3.24}$$

Which implies that θ is also bound to,

$$\theta \lessapprox 10^{-10} \tag{3.25}$$

Why such a low order of magnitude for this parameter? It so happens that the problem is even more severe. In fact, we were not considering the action of chiral transformations in the theta vacuum and the fact that the quarks most likely have a mass[9]. Chiral transformations, and due to an anomaly, change the theta vacuum as [9],

$$e^{i\alpha Q_5}|\theta\rangle = |\theta+\alpha\rangle \tag{3.26}$$

---

[9] Lattice QCD estimates $\frac{m_u}{m_d} \simeq 0.5$ [30].

where Q_5 is the generator of the $U(1)_A$ symmetry. If one were not considering the mass of the quarks one could just define a chiral symmetry that is conserved in order to get rid of the theta term, by rotating it to zero. Taking into account the mass of the quarks, the Lagrangian mass term is [31],

$$\mathcal{L}_{mass} = -i\bar{q}_{iR} M_{ij} q_{jL} + h.c \tag{3.27}$$

where M_{ij} is the quark mass matrix that is not diagonal and not real. Due to this fact a new problem arises. When studying the physical content of a theory one wants to express the theory in a basis where M_{ij} is real and diagonal. In order to do so one must perform a chiral transformation of the form,

$$q_L \to e^{-iArgDet(M)} q_L \tag{3.28}$$

$$q_R \to e^{iArgDet(M)} q_R \tag{3.29}$$

Such a chiral rotation implies that the theta vacuum changes as anticipated by equation 3.26 meaning that the Lagrangian changes as,

$$\mathcal{L} \to \mathcal{L} + \frac{g^2\theta}{32\pi^2} ArgDet(M) G^a_{\mu\nu}\tilde{G}^{a\mu\nu} \tag{3.30}$$

So what in fact must be smaller than 10^{-10} as expressed by equation 3.25 has two contributions: one arising from the structure of the QCD vacuum (the theta term) and the second from the dynamics of the electroweak theory that is $ArgDet(M)$,

$$\bar{\theta} = \theta + ArgDet(M) \lessapprox 10^{-10} \tag{3.31}$$

Why do two terms that arise from different physics cancel each other out with such precision? This is the strong CP problem.

3.5 Possible solution - axion

The axion[10] is a possible solution to the strong CP problem. The main ingredients formulated by R. Peccei and H. Quinn [8, 9] are to consider a chiral symmetry named $U(1)_{PQ}$ that is spontaneously broken at some energy scale greater than Λ_{QCD} ($\Lambda_{QCD} \simeq \mathcal{O}(10^2)$ MeV). The quarks must also be charged with a PQ charge such that a quantum anomaly is generated. The introduction of this symmetry in the theory replaces the $\bar{\theta}$ parameter with a dynamic field, the axion. The axion is a PNG boson where the term "Pseudo" comes from the fact that it has a mass. From Goldstone's theorem one knows that each spontaneously broken symmetry leads to a massless and spinless boson, but due to the fact that the symmetry is anomalous the axion acquires a potential and hence a mass. The $U(1)_{PQ}$ symmetry acts as a shift on the axionic field as [8],

---

[10] For this particular case it is in fact the QCD axion. We drop the "QCD" label for simplicity.

$$U(1)_{PQ} : a \rightarrow a + \alpha f_a \tag{3.32}$$

where α is an arbitrary parameter and f_a is the order parameter associated with $U(1)_{PQ}$ breaking. As stated, the current is not conserved due to an anomaly [9],

$$\partial_\mu J^\mu_{PQ} = \xi \frac{g^2}{32\pi^2} G^a_{\mu\nu} \tilde{G}^{a\mu\nu} \tag{3.33}$$

where ξ is a quantity called colour anomaly, which leads to an additional term in the Lagrangian. At low energies the relevant Lagrangian is [10],

$$\mathcal{L} \supset \frac{1}{2}\partial_\mu a \partial^\mu a + \frac{g^2\bar{\theta}}{32\pi^2} G^b_{\mu\nu}\tilde{G}^{b\mu\nu} + \xi \frac{a}{f_a}\frac{g^2}{32\pi^2} G^b_{\mu\nu}\tilde{G}^{b\mu\nu} \tag{3.34}$$

and this leads to an effective term coupled to $G\tilde{G}$,

$$\bar{\theta}_{eff} = \bar{\theta} + \frac{\xi a}{f_a} \tag{3.35}$$

The new term resulting in the Lagrangian of equation 3.34 represents an effective potential for the axion field being its minimum at $\langle a \rangle = -\frac{\bar{\theta} f_a}{\xi}$,

$$\left\langle \frac{\partial V_{eff}}{\partial a} \right\rangle = -\frac{\xi}{f_a}\frac{g^2}{32\pi^2} \langle G^b_{\mu\nu}\tilde{G}^{b\mu\nu}\rangle \big|_{\langle a \rangle = \frac{-\bar{\theta} f_a}{\xi}} = 0 \tag{3.36}$$

The problem is solved because the minimum of the potential lies exactly at the point where the effective value of $\bar{\theta}$ is completely cancelled, providing a dynamical solution to the strong CP problem. Instantons of QCD generate a potential for the axion which can be obtained by integrating over the gluon fields [9],

$$V_{eff} \simeq \Lambda^4_{QCD} \cos\left(\bar{\theta} + \frac{\xi a}{f_a}\right) \tag{3.37}$$

One can then extract the mass of the QCD axion by expanding the potential at the minimum,

$$m_a^2 = \left\langle \frac{\partial^2 V_{eff}}{\partial a^2} \right\rangle = -\frac{\xi}{f_a}\frac{g^2}{32\pi^2}\frac{\partial}{\partial a} \langle G^b_{\mu\nu}\tilde{G}^{b\mu\nu}\rangle \big|_{\langle a \rangle = \frac{-\bar{\theta} f_a}{\xi}} \tag{3.38}$$

and establishing a connection between mass and energy scale by expanding the potential of equation 3.37 in a power series and retaining the quadratic term of the axionic field. This gives,

$$m_a \simeq \frac{\Lambda^2_{QCD}}{f_a} \tag{3.39}$$

One concludes that the QCD axion has only one free parameter: its mass or equivalently its PQ symmetry breaking scale. There may be other axions besides the QCD axion such as ALPs that emerge from the spontaneous symmetry breaking of more general $U(1)$ symmetries [10]. The physics underlying these particles is very similar to the QCD axion but since ALPs do not couple to QCD there is, *a priori*, no connection between the decay constant, f_a, and their mass.

The QCD axion's mass has several astrophysical constraints [32, 33, 34]. The length of the Neutrino burst of SN1987A and, more recently investigated, cosmological effects of axion hot relics provide an upper bound on the QCD axion's mass [32, 34]. Symmetry breaking scales greater than Planck's mass, where General Relativity and hence gravity takes control are not of interest. Furthermore, a small window (depicted as the small rectangle in Figure 3) between $[10^{-13} - 10^{-11}]$ eV is constrained by black hole superradiance [33]. Thus, one has an open window of $[10^{-11} - 10^{-2}]$ eV for the QCD axion mass range.

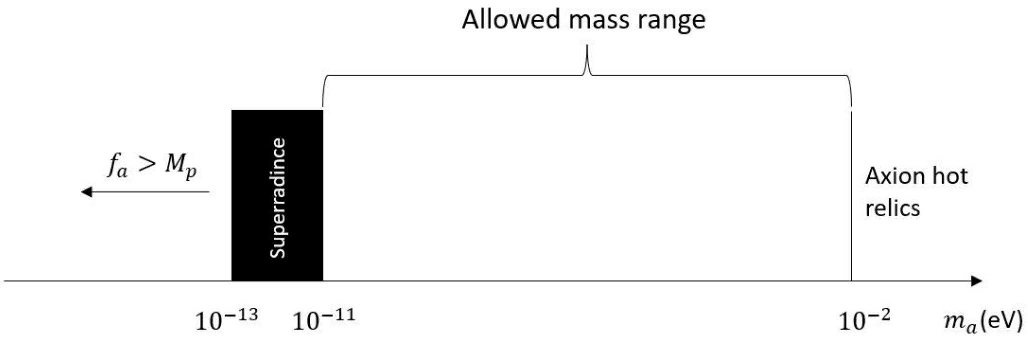

Figure 3: Constraints on the QCD axion mass. The constraints give an upper bound of 10^{-2} eV [32, 34] and a lower bound of 10^{-11} eV [33]. This gives an open window of $[10^{-11} - 10^{-2}]$ eV for the QCD axion mass range.

At low energies, the QCD axion interacts with matter as [35],

$$\mathcal{L}_{int} = ig_{aNN}\partial_\mu a(\bar{N}\gamma^\mu\gamma_5 N) + \frac{ig_{aee}}{2m_e}\partial_\mu a(\bar{e}\gamma^\mu\gamma_5 e) + g_{a\gamma\gamma} a\mathbf{E}\cdot\mathbf{B} \tag{3.40}$$

where the g components represents the axion coupling to the respective particle. For the purposes of this thesis the most relevant coupling is the interaction with photons depicted by the last term in equation 3.40. The decay rate into photon pairs for a general axion is given by,

$$\Gamma = \frac{\alpha_{EM}^2}{256\pi^3}|C_{a\gamma\gamma}|^2 m_a\left(\frac{m_a}{f_a}\right)^2 \tag{3.41}$$

We derive this quantity in Appendices B.1-B.2. The decay rate will play a crucial role in our analysis of axion superradiant instabilities and their observational signatures.

4 Primordial black holes as dark matter candidates

The study of black holes is a growing subject in physics. The growth of this subject is reflected in its recent achievements. From merger detections of black holes with tens of solar masses by LIGO/Virgo [36], which granted in 2017 the Nobel Prize to Kip Thorne, Barry Barish and Rainer Weiss, to more recently the 2020 Nobel Prize [37] which has been divided: one half to Roger Penrose for the discovery that black hole formation is a robust prediction of the general theory of relativity and the other half to Reinhard Genzel and Andrea Ghez who proved the existence of a black hole with a mass of $\simeq 10^6 M_\odot$ in the center of our galaxy. Black holes of this magnitude are labelled as Supermassive Black Holes (SMBH) and it is well established that in the center of every galaxy there should be a SMBH of very large proportions $\gtrapprox 10^6 M_\odot$ [38]. Some of these SMBH have high redshifts and it is just not possible from accretion or mergers of stellar black holes to gather such a huge amount of mass in such short time scales [39]. How do these non-stellar black holes form? Stephen Hawking predicted in 1971 that gravitationally collapsed objects of mass larger than the Planck mass $\simeq 10^{-8}$ kg could be formed as a result of large fluctuations in the density of the early universe [12]. These black holes formed in the early universe are named Primordial Black Holes (PBH) and a relatively recent proposal is a population of PBHs that provide the requisite seeds for the observed population of SMBHs [39]. As we shall see, their masses vary largely depending on their time of formation and for the mass range $\simeq [10^{14} - 10^{18}]$ kg they might represent 100% of the fraction of DM present in the universe. These are the black holes we are interested in. In this chapter, we will start by reviewing the main ideas that constitute the Cosmological Standard Model followed by an insight into the physics of PBHs.

4.1 Brief introduction to the Standard Model of Cosmology

Before investigating PBHs, *per se*, it is convenient to make a brief review of the basic ideas that make up the Standard Model of Cosmology,

1. **Hot Big Bang**: The universe is expanding. If one could reverse time in order to go back

in the opposite direction of the expansion one would eventually reach a singularity called the Big Bang. Considering an isotropic and homogeneous universe, one can describe its dynamics regarding only four fundamental equations[11]. These are the two Friedmann equations, which are obtained from the Einstein field equations using the Friedmann-Lemâitre-Robertson-Walker (FLRW) metric, the equation of continuity and one equation of state for a perfect fluid with a given pressure and density that permeates the universe [13],

$$H^2 = \left(\frac{\dot{a}}{a}\right)^2 = \frac{\rho}{3M_{PL}^2} - \frac{K}{R_o^2 a^2} \tag{4.1}$$

$$\frac{\ddot{a}}{a} = -\frac{1}{6M_{PL}^2}(\rho + 3P) \tag{4.2}$$

$$\dot{\rho} + 3H(\rho + P) = 0 \tag{4.3}$$

$$P = w\rho \tag{4.4}$$

where ρ and P are the energy density and pressure of the fluid, respectively. Also, K represents the spatial curvature of the universe, R_0 represents the radius of curvature of the universe measured today, $M_{Pl}^2 = \frac{1}{8\pi G}$ is the reduced Planck mass, a is the scale factor that describes the expansion of the universe and w is a constant which depends on the type of fluid.

2. **Gravitational instabilities**: The structures observed today (stars, galaxies, clusters...) were originated from the growth of gravitational instabilities. The idea is that starting from small fluctuations in the matter distribution in the early universe, denser regions will exert a stronger gravitational attraction on their neighbours, accreting them. These overdense regions will both become progressively larger and more irregular as time goes by. Therefore, starting with an initial spectrum of fluctuations that is observed in the CMB[12], which grows in time through this process of gravitational instabilities, one gets the large structures observed today.

3. **Inflation**: These small fluctuations can be originated during an early phase of the universe known as inflation. Inflation is believed to have taken place in the very first fraction of a second after the Big Bang singularity [40] where the universe had an extremely

---

[11] Homogeneous means that the universe is the same everywhere on large scales and isotropic means that the universe looks the same no matter which direction we look at.

[12] The CMB was originated when the temperature of the universe lowered enough allowing the electrons to bind with atomic nuclei in the recombination epoch around 400000 years after the Big Bang singularity [13]. Photons that previously scattered with electrons now became free and traveled long distances. The CMB is the imprint of these free photons and it represents a picture of the density fluctuations in the universe at this epoch.

rapid growth. It is usually more convenient not to use the concept of how much time it lasted for but, more accordingly, how much the universe grew in this period with the concept of e-folding time, where 1 e-fold means that the universe expanded by a factor of $e^1 \simeq 2.72$. It so happens that the universe might have grown about 60 efolds (it grew 10^{26} times its original size!) during this period [13, 41]. This theory is also motivated by three troublesome problems of cosmology: the flatness, the horizon and magnetic monopole problems [41]. Inflation will be further explored in the next subsections in order to understand how exactly these fluctuations are produced.

4. **Ingredients that make up the energy density of the universe**: Through accurate measurements of the CMB fluctuations, the Wilkinson Microwave Anisotropy Probe (WMAP), and more recently, the Planck mission [42], were able to measure the basic parameters of the Big Bang model including the density and composition of the universe[13]. These experiments determined that the universe is nearly flat, which tells us that the mean energy density of the universe is equal to the critical density[14]. Of this total density we know that around 5% corresponds to baryonic matter, 72% corresponds to Dark Energy (DE) and 23% corresponds to DM [43]. The present composition of the universe is represented in Figure 4 [44]. For the purposes of this thesis we are more interested in DM.

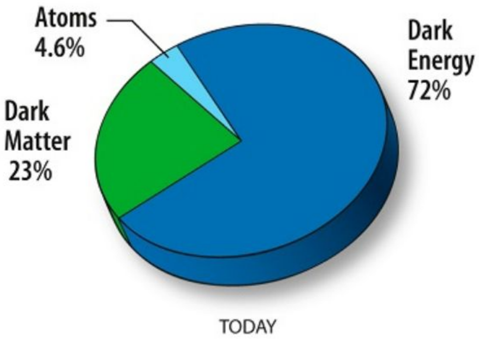

Figure 4: This figure represents the constrains of the content of the present-day universe resulting from the measurements of WMAP [43, 44].

Apart from the CMB, another way we know that DM exists is due to confrontation of theoretical and experimental values of the rotation velocity of certain objects in different relative positions to the center of our galaxy [45]. From observations, DM interacts weakly through gravity although it may have additional weak interactions [46]. We also know that black holes do not interact with anything except through gravity. This is a good motivation to consider PBHs as DM candidates.

---

[13] WMAP and Planck were NASA spacecrafts that measured temperature differences across CMB sky. These measurements played a very important role in establishing the current Standard Model of Cosmology.

[14] The critical density is the density of a flat universe.

4.2 Formation of PBHs

Black holes are usually connected with the collapse of dying stars. However, one can extend this line of thought thinking about the existence of large structures in the universe. The existence of such structures implies that surely there have been some deviations from homogeneity and isotropy at earlier times in the history of the universe. One would therefore expect some regions to become sufficiently compressed through gravitational forces to overcome pressure and the expansion of the universe and to eventually collapse into black holes.

4.2.1 Possible masses

The formation of PBHs through the initial inhomogeneities is possible if an overdense region with size R is greater than the associated Jeans length[15] [35], R_J,

$$R > R_J \quad \Longrightarrow \quad R > c_s\left(\frac{\pi}{G\rho_c}\right)^{1/2} \tag{4.5}$$

where ρ_c is the critical energy density of a flat universe and $c_s = \left(\frac{P}{\rho}\right)^{1/2} = w^{1/2}$ is the sound speed in the medium. Nevertheless, the collapsing region must be inside its Schwarzschild radius in order for the region to collapse into a black hole. Since an overdense region can only collapse once the particle horizon[16] exceeds its size, one assumes that the Hubble horizon[17] is approximately the size of the particle horizon [13, 47],

$$R_H \simeq R_{PH} \simeq \frac{1}{H} \tag{4.6}$$

which means that the mass of a PBH is approximately the mass enclosed in the particle horizon, yielding [47],

$$M_{PBH} \simeq M_{PH} \simeq \frac{4\pi}{3}\rho_c R_{PH}^3 = \frac{1}{2GH}\bigg|_{H\text{ at formation}} \simeq 10^{15}\left(\frac{t}{10^{-23}}\right)\text{g} \tag{4.7}$$

---

[15] Jeans length is the critical radius of a cloud where gravity starts to overcome pressure causing its collapse.

[16] The particle horizon is defined as the maximum distance that particles could have traveled to the observer since the Big Bang.

[17] The Hubble horizon, $\frac{c}{H}$, is defined as the distance that light can travel in one Hubble time, $\frac{1}{H}$. We explicitly write the speed of light, c, to distinguish Hubble horizon and Hubble time. Henceforth it will be set to 1 so that Hubble horizon and Hubble time are indistinguishable.

where the formation was considered to be in the radiation dominating epoch, $w = \frac{1}{3}$. The latter expression shows that one has a very wide range of masses depending on the time of formation. For instance, considering a very early time $t \simeq 10^{-43}$ s one could get a PBH of a mass of $\simeq 10^{-8}$ kg. In contrast, if one considers just a second after the Big Bang singularity one gets a mass of $\simeq 10^5 M_\odot$.

4.2.2 Formation mechanisms

Some formation mechanisms propose high densities in the early universe for PBH formation as well as large density fluctuations, so that overdense regions can eventually cease to expand and recollapse [48]. There are several possible mechanisms for PBH formation such as cosmic strings, bubble collisions and collapse of domain walls [49]. We will, however, briefly discuss the more common explanation of production in the current literature: density fluctuations resulting from inflation. This will be further explored in the following subsections.

It is required that for a PBH to form, the collapsing region must have enough density to surpass a threshold value for formation [13], that is,

$$\delta = \frac{\delta\rho}{\rho} > \delta_c \tag{4.8}$$

where δ is the density contrast, $\delta\rho$ is the density fluctuation and ρ is the average density. An initial estimate by Bernard Carr using the Jean's length and Newtonian gravity showed that an overdensity would collapse into a PBH in a radiation dominating epoch if [48],

$$\delta = \frac{\delta\rho}{\rho} > \delta_c = c_s^2 = \frac{1}{3} \tag{4.9}$$

More recent calculations show that $\delta_c \simeq 0.45$ [50]. Comparing this with the typical amplitude of the density perturbations, A_s, on CMB scales [13] $\delta \simeq \frac{\delta\rho}{\rho} \simeq \sqrt{A_s} \simeq 10^{-5}$, one therefore requires much larger density perturbations than the ones observed in the CMB for an overdensity to collapse into a PBH.

4.2.3 Abundance

Let us assume that some density fluctuations can surpass the threshold value and collapse into black holes. What is the abundance of PBHs we expect to find? One may answer this question considering the statistics of density fluctuations and by calculating the abundance or the relative energy density in PBHs relatively to the total energy density of the universe using the Press-Schechter formalism [51]. The main idea of the formalism is that one assumes that the fraction of the universe that collapses into PBHs at the time of formation is estimated considering the fraction of the universe with $\delta > \delta_c$ using a Probability Density Function (PDF) [13], $P(\delta)$,

$$\beta(M_{PBH}) = \frac{\rho(M_{PBH})}{\rho_{total}}\Big|_{\text{at formation}} = \gamma \int_{\delta_c}^{\infty} P(\delta) d\delta \tag{4.10}$$

where $\gamma \simeq 0.2$ is a numerical factor which depends on the details of gravitational collapse[18] [48]. Given the Gaussian nature of fluctuations during inflation the PDF is usually taken to be [52],

$$P(\delta) = \frac{1}{\sqrt{2\pi}\sigma} e^{-\frac{\delta^2}{2\sigma^2}} \tag{4.11}$$

where σ^2 is the variance of the density fluctuations on the mass scale M_{PBH} which is estimated as [53],

$$\sigma^2(R) = \int d\ln k \, P_\delta(k) \tilde{W}^2(k, R) \tag{4.12}$$

where $P_\delta(k)$ is the power spectra of the primordial density fluctuations[19] which is a function of the comoving wavenumber[20], k, and $\tilde{W}(k, R)$ is the Fourier transform of a real space window function smoothing over the comoving scale $R \simeq \frac{1}{aH}$. Putting all pieces together and assuming $\sigma \ll 1$,

$$\beta(M_{PBH}) \simeq \frac{\gamma\sigma}{\sqrt{2\pi}\delta_c} e^{-\frac{\delta_c^2}{2\sigma^2}} \tag{4.13}$$

On CMB scales, the amplitude of the fluctuations is $\sigma \simeq 10^{-5}$ which leads to $\beta \simeq 10^{-5} e^{-10^{10}}$, which is completely negligible [52].

4.2.4 PBH mass as a function of the comoving wavenumber k

PBHs could be formed when an overdense region enters the Hubble horizon [53]. It is crucial that the perturbation enters the horizon because the process of PBH formation is purely causal. Gravity, which travels at the speed of light, has to communicate the existence of an overdensity so that the gravitational collapse begins. If an overdense region is sourced from primordial perturbations, the size of the overdense region should be characterized by its respective comoving wavenumber. One can therefore obtain the relation between the Hubble scale at the PBH formation and the comoving wavenumber [53],

---

[18] This value was estimated considering a radiation dominating epoch.

[19] This quantity will be discussed in the following subsection.

[20] Physicists often use length scales in terms of the comoving wavenumber $k \simeq \frac{1}{\text{comoving length}}$ [13]. This will be relevant when considering the scales at which perturbations form PBHs, that is when perturbations enter the particle horizon.

$$aH\Big|_{\text{at formation}} = k \tag{4.14}$$

One may now establish a connection between the mass of the PBH and the scales required to obtain overdensities capable of producing black holes. In a radiation dominating epoch, one can show that [54],

$$M_{PBH}(k) = 30M_{\odot}\left(\frac{\gamma}{0.2}\right)\left(\frac{g_*}{10.75}\right)^{-1/6}\left(\frac{k}{2.9\times 10^5\text{Mpc}^{-1}}\right)^{-2} \tag{4.15}$$

where g_* accounts for the number of relativistic degrees of freedom at the epoch of formation [54]. As we shall see in the next subsection, for PBH formation the density perturbations must enter the Hubble horizon which constrains the accessible scale range. This equation is important because it shows that in order to form PBHs one requires very small physical scales (large k's). Looking upon the scales one has access to, Figure 5, that is the CMB scales, we get $\simeq [10^{-3} - 10^{-1}]\,\text{Mpc}^{-1}$. But the physical scales one requires to form PBHs are much smaller. Thus, to form PBHs from primordial density perturbations, one needs to consider some mechanism that can amplify perturbations during the inflationary phase at smaller physical scales than those accessible with CMB observations.

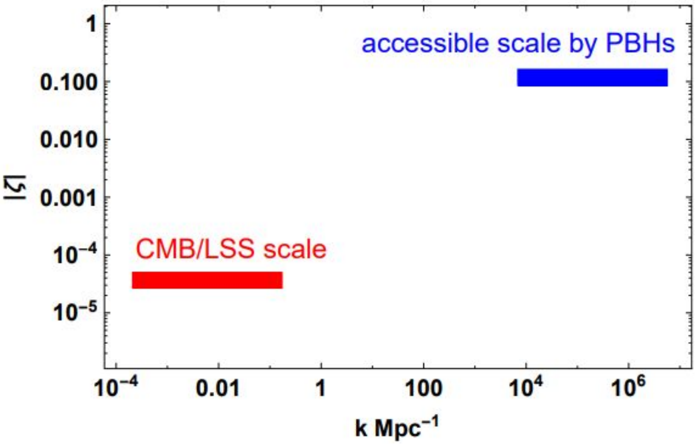

Figure 5: Hierarchy between the CMB/LSS scale and amplitudes and accessible scale by PBHs [53].

4.3 Inflation

Overdense regions are required for PBH formation. The most studied way of fulfilling this requisite is through inflation. Inflation justifies the fluctuations one observes in the CMB, which then answers the riddle of the growth of cosmological structures observed today, by assuming quantum perturbations in the inflationary epoch [13]. The most concrete definition of inflation is of an accelerated phase of expansion of the universe,

$$\ddot{a} > 0 \tag{4.16}$$

One concludes from equation 4.2 that this is only achievable considering a negative pressure fluid, $w < -\frac{1}{3}$. It so happens that considering a perfect fluid with $w < -\frac{1}{3}$ one would obtain an eternal inflation. To make it finite, at some point $w > -\frac{1}{3}$ must yield so w must be time dependent. It is also extremely difficult to get an extended duration of inflation unless the equation-of-state parameter satisfies $w \simeq -1$. This is usually a practical definition of inflation [13]. One may then introduce a new scalar field, the inflaton, with such characteristics that may reproduce the accelerated expansion of the early universe.

The dynamics of a scalar field minimally coupled to gravity is given by the action [40],

$$S = \int d^4x\sqrt{-g}\mathcal{L} = \int d^4x\sqrt{-g}\Big[-\frac{1}{2}\partial_\mu\phi\partial^\mu\phi - V(\phi)\Big] \tag{4.17}$$

where g is the determinant of the metric. From the Euler-Lagrange equations for a homogeneous field [41],

$$\ddot{\phi} + 3H\dot{\phi} + V'(\phi) = 0 \tag{4.18}$$

where $3H\dot{\phi}$ is a friction term resulting from the expansion of the universe and $V'(\phi) = \frac{dV}{d\phi}$. For a homogeneous field, one may obtain its energy density, ρ_ϕ, and pressure, P_ϕ, from the energy-momentum tensor,

$$T_{00} = \rho_\phi = \frac{\dot{\phi}^2}{2} + V(\phi) \tag{4.19}$$

$$T_{ii} = P_\phi = \frac{\dot{\phi}^2}{2} - V(\phi) \tag{4.20}$$

In order for the inflaton to behave as a negative pressure fluid with $w \simeq -1$, as required for an accelerated expansion, the potential energy must dominate over the kinetic energy, $V(\phi) \gg \dot{\phi}^2$. Requiring this implies that one can neglect the first term in equation 4.18 because the acceleration of the field must be small. This consideration is regarded as the Slow Roll (SR) assumption which can be written in terms of two dimensionless parameters [41],

$$\epsilon_\phi = \frac{M_{Pl}^2}{2}\Big(\frac{V'}{V}\Big)^2 \ll 1 \qquad |\eta_\phi| = M_{Pl}^2\Big|\frac{V''}{V}\Big| \ll 1 \tag{4.21}$$

However, as previously stated, our interest in these inflationary models is due to the production of density perturbations. The inflaton is a quantum field so it must exhibit small quantum fluctuations about its homogeneous value [41]. Introducing these fluctuations in equation 4.18 and expanding the field fluctuations in a basis of Fourier modes rescalled by the scale factor one may obtain a mode equation which corresponds to a harmonic oscillator with a time-dependent frequency [41],

$$\chi_k'' + \left(k^2 - \frac{2}{\tau^2}\right)\chi_k = 0 \tag{4.22}$$

where $\chi_k(\tau) = \delta\phi_k(\tau)a(t)$ and τ is the conformal time[21]. One can show that when a mode exits the horizon, its amplitude approaches a constant value whereas for a mode inside the horizon its amplitude decays exponentially [41]. This is important because it shows that inflation stretches quantum fluctuations to super-horizon scales and amplifies them to a constant value. Since the physical wavelength associated to a mode k is exponentially stretched by expansion during inflation,

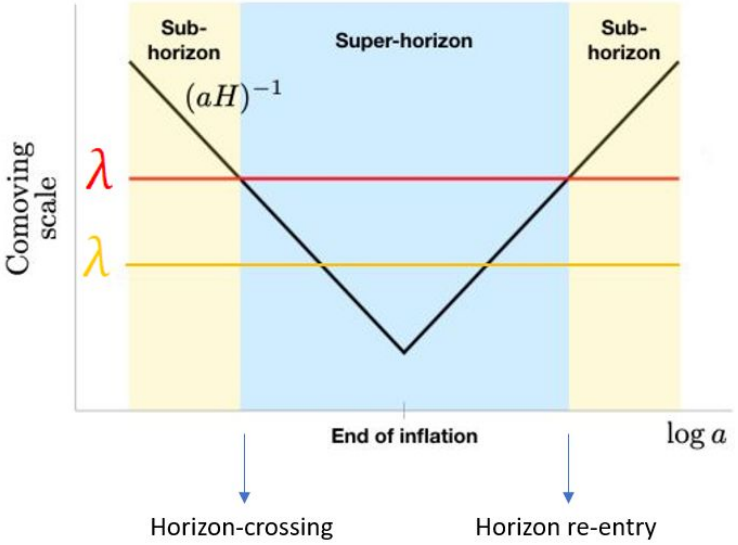

Figure 6: The evolution of a comoving scale and comoving horizon as a function of $\ln a$. Modes with a constant comoving scale become super-horizon ($k < aH$) during inflation and then re-enter the horizon after inflation has ended when the comoving horizon, $\frac{1}{aH}$, grows. The red line corresponds to a large scale observed in the CMB, while the yellow line corresponds to a smaller scale that re-enters the horizon earlier [13].

$$\lambda = \frac{2\pi}{k}a \tag{4.23}$$

at some point it will become larger than the horizon which remains roughly constant during inflation. Perturbations with length scales that are larger than the horizon are known as super-horizon, $k < aH$, while perturbations with length scales smaller than the horizon are known as sub-horizon, $k > aH$. A mode crosses the horizon when $k = aH$, as represented in Figure 6. Since comoving modes with the same wavelength re-enter the horizon at the same time their oscillating phases will be aligned and they will oscillate in phase. However, this will produce a coherent phase structure in the perturbations due to the SR assumptions such that, at the time of recombination, different modes will be in different phases of their oscillation, producing the small fluctuations one observes in the CMB [41]. One could estimate the power spectrum of these modes but it so happens that this quantity is not appropriate since it is not gauge invariant. This is because the field perturbations will lead to perturbations in the energy-momentum tensor, which in turn generate perturbations of the metric of the expanding spacetime [41]. Thus, the small quantum fluctuations of the inflaton field make the underlying spacetime slightly inhomogeneous inducing deviations both in the scalar field as well as in the metric,

---

[21] The conformal time is defined as $d\tau = \frac{dt}{a(t)} \implies \tau = \int \frac{dt}{a(t)} = -\frac{1}{aH}$. During inflation the scale factor grows exponentially, $a(t) \simeq e^{Ht}$, and H is approximately constant.

$$\phi = \bar{\phi} + \delta\phi \qquad g_{\mu\nu} = \bar{g}_{\mu\nu} + \delta g_{\mu\nu} \tag{4.24}$$

Therefore, if one wants to compare theoretical values with experimental data one requires a gauge invariant quantity that is invariant under change of coordinates. The quantity of interest is the comoving curvature perturbation which represents the gravitational potential of a comoving hypersurface [40],

$$\zeta = \frac{1}{a}\Big(\frac{H}{\dot{\phi}}\delta\phi + \Psi\Big) \tag{4.25}$$

With this gauge invariant quantity one may obtain the power spectrum which is defined from its 2-point correlation function [40],

$$P_\zeta(k) = \Big(\frac{H}{2\pi}\Big)^2\Big(\frac{H}{\dot{\phi}}\Big)^2 \tag{4.26}$$

For the production of PBHs, one requires larger perturbations as well as smaller physical scales (larger k's). One has the freedom to study a smaller wavenumber but this leaves a problem. This wavenumber exits the horizon after the one we were considering before and re-enters the horizon earlier[22], that is the yellow line in Figure 6. So for these times one can only take an educated guess. What about the large perturbation requirement? A quick look at equation 4.26 tells us that if one could somehow slow down the field maybe one could produce a larger power spectrum. One can imagine another inflationary regime without spoiling the SR prediction considering, for instance, a regime with an inflection point in the scalar potential, as depicted in Figure 7, where the approximation that the velocity is nearly constant is spoiled.

---

[22] A mode re-entering the horizon earlier than the CMB scales means that it is not accessible to us.

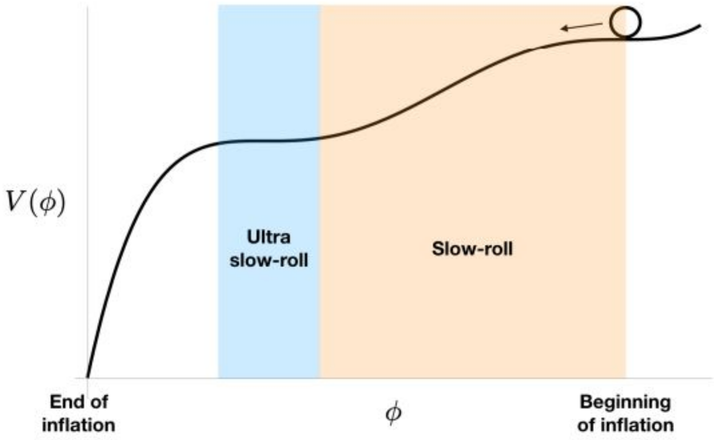

Figure 7: An example of an inflaton potential that has a SR regime and an USR regime which may produce a strong enough spectrum to form PBHs. The inflaton eventually leaves this inflection point moving to the global minimum which translates in the ending of inflation. Image taken from [13].

At this point $V' \simeq 0$ and from equation 4.18 [13],

$$\ddot{\phi} + 3H\dot{\phi} = 0 \tag{4.27}$$

The inflection point implies that the velocity of the field is exponentially suppressed therefore enhancing the power spectrum. This is known as the Ultra Slow Roll (USR) regime. This way, when the perturbations re-enter the horizon, they will be so large at such small scales that they will collapse forming PBHs. The inflaton eventually leaves this inflection point[23] moving to the global minima which translates in the ending of inflation.

4.4 Constraints on PBHs as DM candidates

When studying PBHs as a DM candidate the constraints are normally best expressed as the fraction of DM in the form of PBHs today, $f_{PBH} = \frac{\Omega_{PBH}}{\Omega_{DM}}$. There are several phenomena that provide constrains on the PBH's mass such as Evaporation, Microlensing, Gravitational Waves, Accretion, Dynamical [13, 14, 55]. A summary on f_{PBH} showing which types of constraints are most important over a wide range of mass scales is shown in Figure 8 [14]. From this figure one can extract the mass range on which PBH may represent 100% of DM, $\simeq [10^{14} - 10^{18}]$kg. This mass range was constrained until 2014 due to PBH capture by neutron stars at the centres of globular clusters [38, 56, 57]. However, these constrains have been disputed because the DM

---

[23] Note that the potential must be carefully chosen such that a period of eternal inflation is avoided.

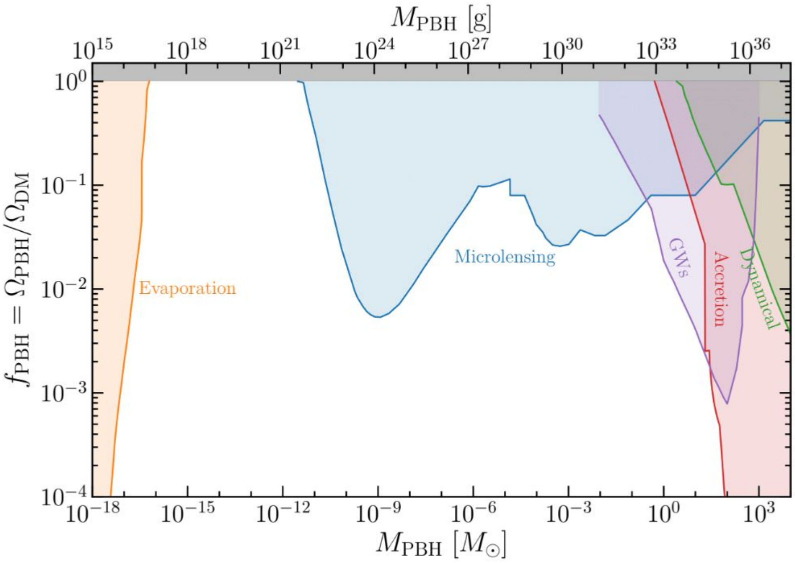

Figure 8: All constraints on the fraction of DM in the form of PBHs: evaporation, microlensing, gravitational waves, PBH accretion and dynamical constraints. Attention is restricted to PBHs with $M_{PBH} \ll 10^7 M_\odot$ which could constitute the DM halos of small dwarf galaxies [14].

density in globular clusters is currently known to be much lower than assumed in these analyses [38, 58]. We will focus our study of PBH superradiant instabilities in this mass range since, being the most abundant PBHs, they may lead to the largest axion population on galactic and cosmological scales, and therefore to the strongest electromagnetic signatures.

5 Dynamics of primordial axion superradiant clouds

After the thorough analysis of the cloud properties in section 2 we are ready to study the dynamics of the system composed by a rotating PBH surrounded by a cloud of heavy axions, which decay into photons, in the presence of interactions between superradiant states [4]. In this section, we perform numerical and analytical studies to determine the number of axions produced by superradiance throughout the cosmic history. Henceforth, we use Planck's mass as $M_p \simeq 2 \times 10^{-8}$ kg and we write $\hbar$ explicitly to recognize angular momentum exchange.

5.1 Dynamics of multiple superradiant states

Here, we study the dynamics of these systems and analyse the number of axions within and outside the cloud. What is the number of particles produced through superradiance and how does this number vary in time? In what manner do axion self-interactions and decays affect the cloud's growth? In order to answer these questions we first need to compute the equations that rule the dynamics of the dominant superradiant states. This dynamics is non-trivial and requires a thorough investigation.

5.1.1 Equations that rule the dynamics

For a spin-0 particle, the simplest non-gravitational interaction is a quartic self-interaction. The introduction of such a term induces non-trivial dynamics amongst superradiant states and the evolution of the system can be treated perturbatively [4]. Such analysis confronts the non-linear term with the gravitational binding energy in the non-relativist limit providing numerous possible quartic self-interaction processes. All these processes occur at a given rate that grows with a power of the fine structure constant α [4]. Since for this analysis to hold it is required that $\alpha \ll 1$, the dominant quartic self-interaction processes are the ones depicted in Figure 9 [4]. Note that there are other quartic self-interaction processes that represent different transitions than the ones illustrated in Figure 9. In particular, some processes provide gravitational wave emission. However, these are negligible when compared with the dominant processes depicted

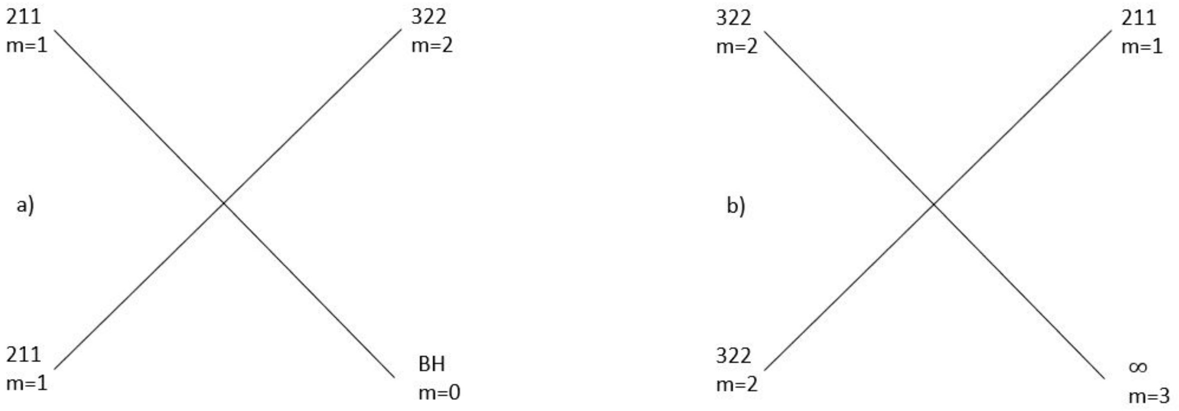

Figure 9: Dominant axion self-interaction processes. Process a) is the annihilation of two axions in the 211 state leading to one axion in the 322 state and the other in an $m = 0$ non-superadiant mode that is absorbed by the black hole. Process b) is the annihilation of two axions in the 322 state leading to one axion in the 211 state and the other to escape the black hole's gravitational potential. Note that angular momentum m is conserved.

in Figure 9 [4]. This way, we perform a simplified analysis where the dominant processes involve only two superradiant states. In process a) we expect the annihilation of two axions in the 211 state[24] leading to one axion in the 322 state and the other in an $m = 0$ non-superadiant mode that is absorbed by the black hole. In process b) we expect the annihilation of two axions in the 322 state leading to one axion in the 211 state and the other to possess enough energy to escape the black hole's gravitational potential, becoming free. Apart from these processes, the evolution of the scalar field around black holes is also driven by superradiant growth and axion to photon decay. The number of axions in the 211 and 322 states varies according to Boltzmann equations,

$$\frac{dN_2}{dt} = \Gamma_2 N_2 - 2\Gamma_{22} N_2^2 N_3 + \Gamma_{33} N_3^2 N_2 - \Gamma_{a\gamma\gamma} N_2 \tag{5.1}$$

$$\frac{dN_3}{dt} = \Gamma_3 N_3 + \Gamma_{22} N_2^2 N_3 - 2\Gamma_{33} N_3^2 N_2 - \Gamma_{a\gamma\gamma} N_3 \tag{5.2}$$

where $\Gamma_{a\gamma\gamma}$ is the axion to photon decay rate (equation 3.41), Γ_2/Γ_3 is the superradiant rate of the 211/322 state, and Γ_{22}/Γ_{33} is the transition rate of the annihilation of two axions in the 211/322 state (Figure 9 a)/b)), respectively. Taking into account superradiant emission into the 211 and 322 states, as well as the $m = 0$ mode reabsorption, the black hole's mass and angular momentum vary according to,

---

[24] We use the spectroscopic notation where 211 means $n = 2$, $l = 1$ and $m = 1$.

$$\frac{dM}{dt} = -\mu(\Gamma_2 N_2 + \Gamma_3 N_3 - \Gamma_{22} N_2^2 N_3) \tag{5.3}$$

$$\frac{dJ}{dt} = -\hbar(\Gamma_2 N_2 + 2\Gamma_3 N_3) \tag{5.4}$$

These, together with equations 5.1-5.2, describe the dynamics of the system. The system reaches an equilibrium when,

$$\frac{dN_2}{dt} = \frac{dN_3}{dt} = 0 \tag{5.5}$$

As we shall discuss in the next subsections, in our analysis we consider regimes where $\Gamma_2 > \Gamma_{a\gamma\gamma}$, meaning that we can neglect the decay terms in equations 5.1-5.2. Additionally, since $\alpha \ll 1$, we also neglect the superradiant growth rate of the 322 state which grows as $\Gamma_3 \propto \alpha^{12}$ [4]. Solving equation 5.5 provides the equilibrium numbers for the 211 and 322 states,

$$N_2 = \frac{2}{\Gamma_{22}}\sqrt{\frac{\Gamma_{33}\Gamma_2}{3}} \quad , \quad N_3 = \sqrt{\frac{\Gamma_2}{3\Gamma_{33}}} \tag{5.6}$$

According to the computation in [4] we can extract the rates of the relevant processes,

$$\Gamma_{22} \simeq 8 \times 10^{-7}\alpha^7\lambda^2\mu \ , \ \Gamma_{33} \simeq 10^{-8}\alpha^4\lambda^2\mu \text{ and } \Gamma_2 \simeq 4 \times 10^{-2}\alpha^8\mu(\tilde{a} - 4\alpha) \tag{5.7}$$

where λ is the coupling constant of the quartic self-interaction term and Γ_2 is obtained from equation 2.33 considering $\Gamma_2 = 2\omega_I$ and evaluating for the 211 state in the $\alpha \ll 1$ limit. Since for axions from equation 3.37, $\lambda^{-1} = \left(\frac{f_a}{\mu}\right)^2$, we estimate the equilibrium number for the 211 state as,

$$N_{eq} \simeq \frac{50}{\sqrt{3}}\sqrt{\tilde{a} - 4\alpha}\,\alpha^{-1}\left(\frac{f_a}{\mu}\right)^2 \tag{5.8}$$

5.1.2 Parameter space

Before proceeding we recall the fundamental parameters of the problem. Whether we consider the QCD axion or an ALP, the black hole spin, $\tilde{a}$, and mass, M are always two fundamental parameters. For the QCD axion, its mass, μ, is an additional parameter. For an ALP, the decay constant, f_a, is independent of its mass meaning that it is another additional parameter. In this work we are interested in black holes with masses capable of accounting for 100% of the fraction of DM [14], $[10^{14} - 10^{18}]$kg, since they may lead to the largest axion population on galactic and cosmological scales, and therefore to the strongest electromagnetic signatures. We compute our parameter space plots (in yellow) in Figures 10-11 for the ALP and QCD axion with low $\tilde{a} = 0.01$ and high $\tilde{a} = 0.99$ spins where two conditions must be satisfied:

1. To guarantee the superradiant growth we require the superradiant condition to be fulfilled,
$$\frac{2\mu M}{M_p^2} < \frac{\tilde{a}}{1+\sqrt{1-\tilde{a}^2}} \tag{5.9}$$
2. We want the cloud to be fully formed within the universe's age. We therefore require that the universe's age is greater than the equilibrium time which can be obtained from equation 5.1 where we neglected the self-interaction terms, since they are negligible until equilibrium is reached, yielding $\frac{dN_2}{dt} \simeq \Gamma_2 N_2$. This provides a condition,
$$t_{uni} > t_{eq} \simeq \frac{\ln(N_{eq})}{\Gamma_2} \tag{5.10}$$
where N_{eq} is given by equation 5.8 and Γ_2 by equation 5.7. Even though this equation is f_a dependent, different f_a values do not imply a significant change in the parameter space since this condition scales logarithmically with f_a.

We are particularly interested in the low spin plots since recent studies propose that PBHs formed in a radiation dominating era should possess a percent level dimensionless spin parameter [59].

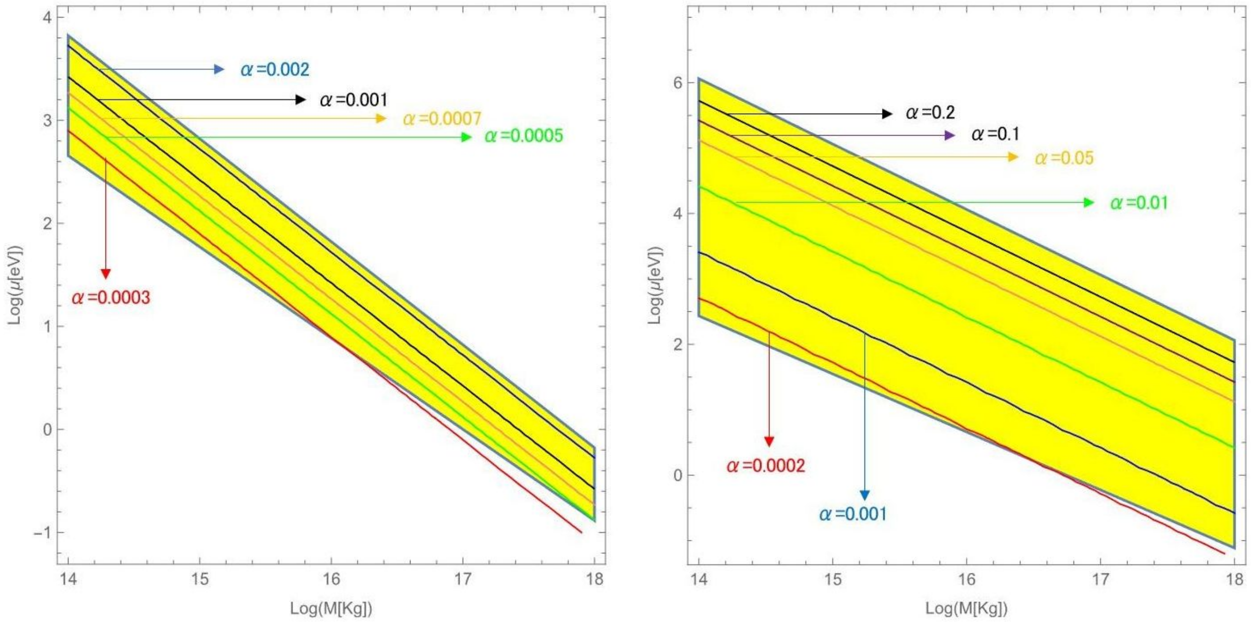

Figure 10: Regions where condition 1 and 2 are satisfied for ALPs. We consider black hole masses within the range where they may account for 100% of the DM and $f_a = 10^{10}$ GeV. Different values for the decay constant do not imply a significant change in the allowed parameter space since the f_a dependent condition scales logarithmically. We consider two extreme values of spin: In the left plot $\tilde{a} = 0.01$, and in the right plot $\tilde{a} = 0.99$. Different values of α are represented by straight lines with different colours as labelled.

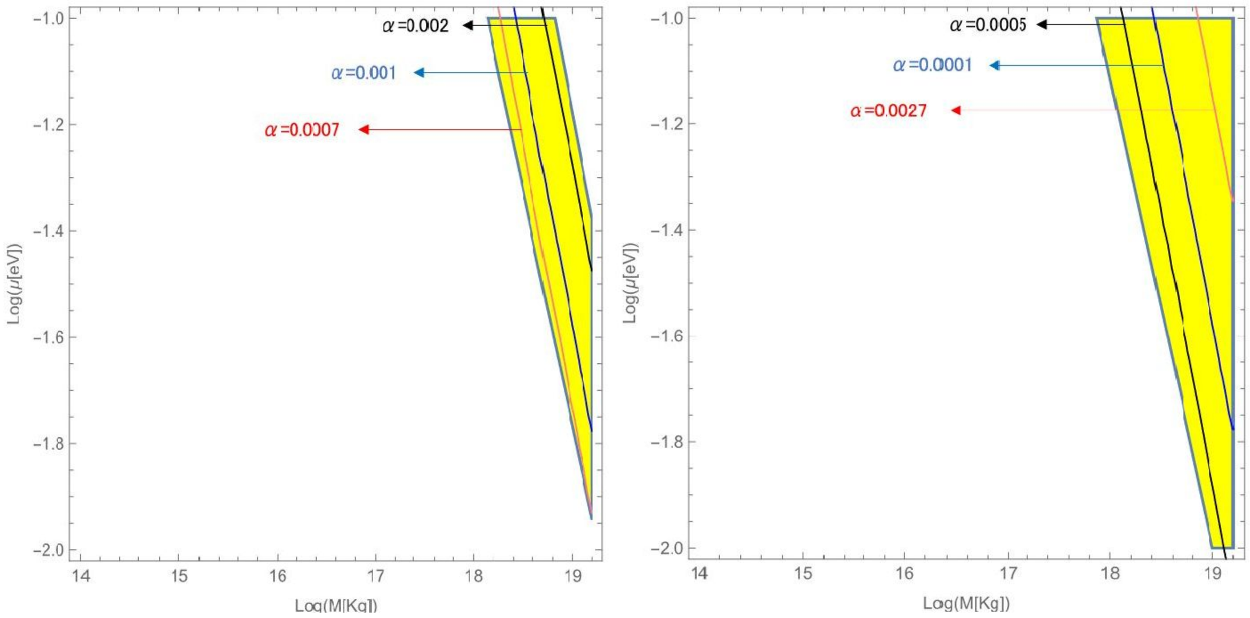

Figure 11: Regions where condition 1 and 2 are satisfied for the QCD axion. There is no available region for the black hole masses within the $[10^{14} - 10^{18}]$ kg range. We extended this region until 10^{19} kg where it may represent 10% of the DM [14]. We consider two extreme values of spin: In the left plot $\tilde{a} = 0.01$, and in the right plot $\tilde{a} = 0.99$. Different values of α are represented by straight lines with different colours as labelled.

5.1.3 Numerical solution

We may now proceed with the numerical study of the dynamics resulting from equations 5.1-5.4. Now that we possess an insight on the parameter space, we compute values within this range and solve the equations numerically. We will restrict our discussion to ALPs since it represents the most demanding case. In fact, the equations are exactly the same for both cases the only difference being the f_a connection with the QCD axion's mass. For ALPs, there is no connection.

Due to self-interactions the number of particles cannot grow arbitrarily large. In this manner, we compare the equilibrium number, N_{eq}, with the maximum axion number it is possible for the cloud to hold, N_{max}, in the absence of self-interactions. We establish an upper value for the decay constant, above which the equilibrium number surpasses the maximum number. This threshold is estimated from the superradiant condition (equation 2.34) neglecting the variation of the black hole's mass, $\Delta M \simeq 0$, which is a valid approximation for small spin values,

$$N_{max} = \frac{\Delta J}{\hbar} = (\tilde{a}_i - \tilde{a}_f)\frac{M^2}{M_p^2} \implies N_{max} = (\tilde{a}_i - 4\alpha)\frac{M^2}{M_p^2} \tag{5.11}$$

where the final spin value is $\tilde{a}_f \simeq 4\alpha$, saturating the superradiance condition. We compare these quantities as $\frac{N_{eq}}{N_{max}} < 1$ leading to,

$$f_a^{upper} < 1.8 \times 10^{13} \left(\frac{\alpha}{4 \times 10^{-4}}\right)^{3/2} (\tilde{a} - 4\alpha)^{1/4}\,\text{GeV} \implies f_a^{upper} < 5.0 \times 10^{12}\,\text{GeV} \tag{5.12}$$

where in the last expression we considered, and will consider henceforth, an ALP with $\mu = 1$ keV, and a black hole spin, $\tilde{a} = 0.01$, and mass, $M = 10^{14}$ kg which corresponds to $\alpha \simeq 4 \times 10^{-4}$. This provides an upper bound for the decay constant, above which self-interactions are negligible and the axion number reaches is maximal value. For values above this threshold we assume the number of axions to remain approximately stable, at $\simeq N_{max}$, as long as $\Gamma_{a\gamma\gamma}^{-1} > t_{uni}$. We can also construct a lower bound for the decay constant ensuring an effective axion production with $\Gamma_2 > \Gamma_{a\gamma\gamma}$,

$$f_a^{lower} > 1.6 \times 10^{4} (\tilde{a} - 4\alpha)^{-1/2} \left(\frac{\mu}{\text{keV}}\right) \left(\frac{4 \times 10^{-4}}{\alpha}\right)^{4} \text{GeV} \implies f_a^{lower} > 2.2 \times 10^{5}\,\text{GeV} \tag{5.13}$$

where in the last expression we used the same parameters as above and considered, and will consider henceforth, $|C_{a\gamma\gamma}| = 1$. To have a complete understanding of the dynamics, we perform a numerical analysis of the differential equations within this range. Considering the previous parameters, we study four different f_a values. Results are plotted in Figure 12.

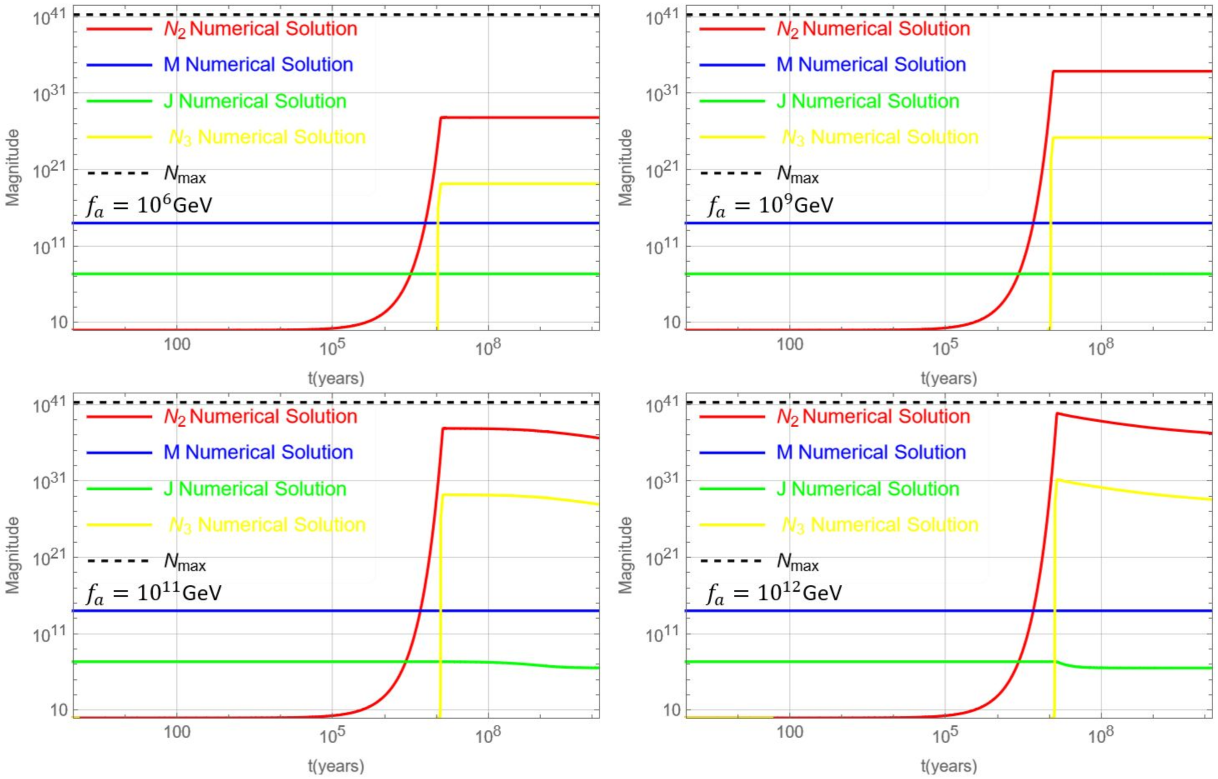

Figure 12: Numerical solution to the dynamics considering four different f_a values assuming $M = 10^{14}$ kg, $\tilde{a} = 0.01$, $\mu = 1$ keV and $|C_{a\gamma\gamma}| = 1$.

The cloud reaches an equilibrium after $\simeq 10^7$ years, where it remains approximately stable until today for low f_a values (upper plots of Figure 12). As f_a increases, the number of particles in the dominant superradiant states is enhanced. When the black hole loses a significant portion of its angular momentum (notice the green line in the lower plots of Figure 12) the equilibrium ceases and the axion number slowly decreases at an approximately constant rate. This suppression will be further explored in the next subsection. The relevant quantity in this analysis is the number of particles in the 211 state. We therefore evaluate the evolution of the ALP number in this state for different f_a values in Figure 13 (left plot). We are interested in computing the photon flux emitted by axion clouds and this is ultimately a product of the ALP final number in the cloud, which grows with f_a^2 when the equilibrium is reached, and the ALP decay rate (equation B.15), which decreases with f_a^{-2}, so that we compute N_2/f_a^2 in order to estimate the values of f_a that maximize this flux. The latter statement anticipates constant flux values (f_a independent) as long as the equilibrium is sustained. Results are illustrated in Figure 13 (right plot). As previously anticipated, for f_a values smaller than 10^{10} GeV the fraction seems to reach a constant value. For higher f_a values, the axion number suppression translates into a smaller quotient value. For this particular case, f_a's ranging over $\simeq [2 \times 10^5 - 10^{10}]$ GeV maximize N_2/f_a^2.

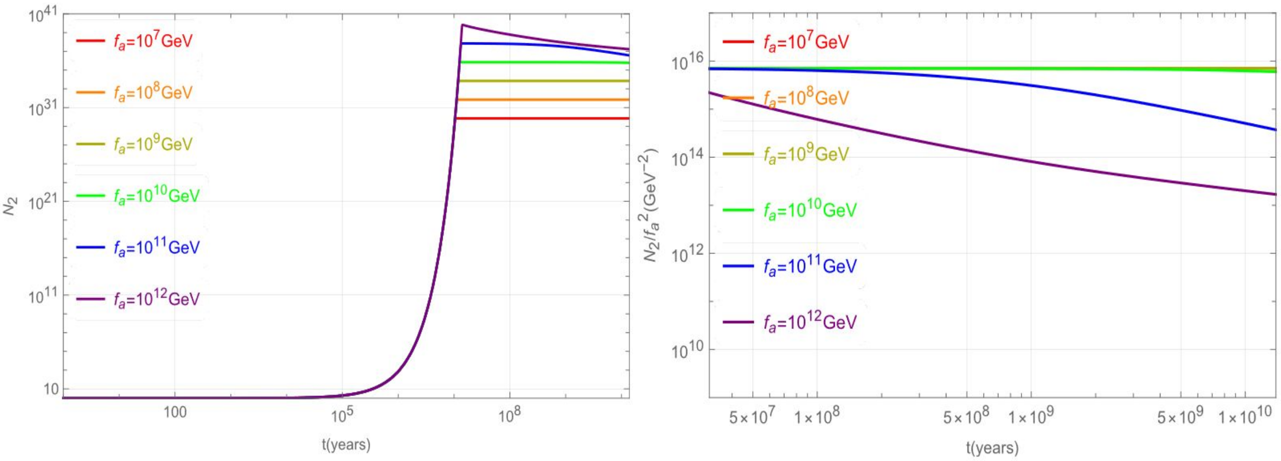

Figure 13: Left plot: Evolution of the ALP number in the 211 state for different f_a values. We observe a slight suppression of the ALP number which seems to slowly decrease, at an approximately constant rate, for $f_a \gtrapprox 10^{10}$ GeV. Right plot: N_2/f_a^2 fraction as a function of time. We consider a time interval ranging over the instant the system reaches an equilibrium until today. For $f_a \lessapprox 10^{10}$ GeV, the fraction reaches a constant value. For both cases we consider f_a values ranging over $[10^7 - 10^{12}]$ GeV with different colours as labelled.

5.1.4 Analytical solution

Now that we have a numerical insight on the dynamics, we construct an analytical description of the axion number in the 211 state. In order to proceed, and considering the lower (equation 5.13) and upper (equation 5.12) f_a values, we distinguish four regimes:

1) $f_a > f_a^{upper}$: The cloud reaches the maximum particle number allowed before any kind of equilibrium is achieved. We estimate an instant, t_{max}, taking into account $N_2(t) \simeq e^{\Gamma_2 t}$ and using N_{max} (equation 5.11),

$$t_{max} \simeq 8.0 \times 10^2 \frac{\ln\left[N_{max}\right]}{\tilde{a} - 4\alpha} \left(\frac{\alpha}{4 \times 10^{-4}}\right)^{-8} \left(\frac{\text{keV}}{\mu}\right) \text{ years} \simeq 1.2 \times 10^7 \text{ years} \tag{5.14}$$

Self-interactions play a negligible role and the cloud remains stable around the black hole as long as $\Gamma_{a\gamma\gamma}^{-1} > t_{uni}$,

$$f_a > 6.6 \times 10^7 \left(\frac{\mu}{\text{keV}}\right)^{3/2} \text{GeV} \implies f_a > 6.6 \times 10^7\,\text{GeV} \tag{5.15}$$

Equations 5.15 and 5.12 dependence on the axion mass ensure us that the cloud remains approximately stable around the black hole for any parameter value within our previously determined parameter space. For this regime we estimate,

$$\begin{cases} N(t) = e^{\Gamma_2 t} & \text{for} \quad t \in [0, t_{max}] \\ N(t) = N_{max} & \text{for} \quad t \in [t_{max}, t_{uni}] \end{cases} \tag{5.16}$$

2) $f_a < f_a^{upper}$: The system reaches a dynamical equilibrium which prevents the cloud from growing arbitrarily large. After reaching equilibrium one of two situations may occur:

   2.1) The black hole does not lose a significant portion of its angular momentum within the age of the universe and the cloud remains stable, $t_J > t_{uni}$. We estimate this instant as $t_J \simeq \frac{J}{\dot{J}} \simeq \frac{\tilde{a}M^2}{M_p^2 N_{eq} \Gamma_2}$, yielding,

$$t_J \simeq 2.6 \times 10^7 \frac{\tilde{a}}{(\tilde{a} - 4\alpha)^{3/2}} \left(\frac{\text{keV}}{\mu}\right) \left(\frac{\alpha}{4 \times 10^{-4}}\right)^{-5} \left(\frac{10^{11}\text{GeV}}{f_a}\right)^2 \text{years} \tag{5.17}$$

   which bounds the decay constant as,

$$f_a < 4.4 \times 10^9 \frac{\tilde{a}^{1/2}}{(\tilde{a} - 4\alpha)^{3/4}} \left(\frac{\text{keV}}{\mu}\right)^{1/2} \left(\frac{\alpha}{4 \times 10^{-4}}\right)^{-5/2} \text{GeV} \implies f_a < 1.8 \times 10^{10}\,\text{GeV} \tag{5.18}$$

For this regime we estimate,

$$\begin{cases} N(t) = e^{\Gamma_2 t} & \text{for} \quad t \in [0, t_{eq}] \\ N(t) = N_{eq} & \text{for} \quad t \in [t_{eq}, t_{uni}] \end{cases} \tag{5.19}$$

where t_{eq} is given in a similar manner as equation 5.14,

$$t_{eq} \simeq 8.0 \times 10^2 \frac{\ln\left[N_{eq}\right]}{\tilde{a} - 4\alpha} \left(\frac{\alpha}{4 \times 10^{-4}}\right)^{-8} \left(\frac{\text{keV}}{\mu}\right) \text{years} \tag{5.20}$$

2.2) The black hole loses a significant portion of its angular momentum within the age of the universe and the cloud is unstable, $t_J < t_{uni}$,

$$f_a > 4.4 \times 10^9 \frac{\tilde{a}^{1/2}}{(\tilde{a} - 4\alpha)^{3/4}} \left(\frac{\text{keV}}{\mu}\right)^{1/2} \left(\frac{\alpha}{4 \times 10^{-4}}\right)^{-5/2} \text{GeV} \implies f_a > 1.8 \times 10^{10}\, \text{GeV} \tag{5.21}$$

As concluded through the numerical solutions, after the black hole loses a significant portion of its angular momentum the particle number starts to slowly decrease. Thus far, we have considered the superradiant growth rate, Γ_2, as constant. Looking at Figure 12, we conclude that the black hole's mass has indeed a very small variation but its angular momentum has significantly changed. At this particular point we can no longer consider the superradiant growth rate as a constant parameter. In fact, equation 5.6 and the superradiant growth rate in equation 5.7 should be re-written as,

$$\Gamma_2(t) \simeq 4 \times 10^{-2} \alpha^8 \mu (\tilde{a}(t) - 4\alpha) \text{ and } N_2(t) \simeq \frac{2}{\Gamma_{22}} \sqrt{\frac{\Gamma_{33}\Gamma_2(t)}{3}} \tag{5.22}$$

The variation in the black hole's spin neglecting the variation of its mass, $\Delta M \simeq 0$ yields,

$$\dot{\tilde{a}} \simeq \left(\frac{M_p}{M}\right)^2 \frac{\dot{J}}{\hbar} \tag{5.23}$$

and from equation 5.4,

$$\dot{\tilde{a}} = -\frac{M_p^2 N_2(t) \Gamma_2(t)}{M^2} \tag{5.24}$$

Inserting equation 5.22,

$$\dot{\tilde{a}} = -z(\tilde{a}(t) - 4\alpha)^{3/2} \text{ with } z = \left(\frac{M_p}{M}\right)^2 \frac{2}{\Gamma_{22}} \sqrt{\frac{\Gamma_{33}}{3}} (4 \times 10^{-2} \alpha^8 \mu)^{3/2} \tag{5.25}$$

We solve the differential equation,

$$\tilde{a}_f = \frac{4(\tilde{a}_i - 4\alpha)}{(2 + z(\tilde{a}_i - 4\alpha)^{1/2}(t - t_J - t_{eq}))^2} + 4\alpha \tag{5.26}$$

and insert this result in the axion number in equation 5.22,

$$N(t) = \frac{N_{eq}}{1 + 2 \times 10^{-2} N_{eq} \left(\frac{M_p}{M}\right)^2 \alpha^8 \mu (t - t_J - t_{eq})} \tag{5.27}$$

For this regime we then have,

$$\begin{cases} N(t) = e^{\Gamma_2 t} \quad \text{for} \quad t \in [0, t_{eq}] \\ N(t) = N_{eq} \quad \text{for} \quad t \in [t_{eq}, t_{eq} + t_J] \\ N(t) = \dfrac{N_{eq}}{1 + 2 \times 10^{-2} N_{eq} \left(\frac{M_p}{M}\right)^2 \alpha^8 \mu (t - t_J - t_{eq})} \quad \text{for} \quad t \in [t_{eq} + t_J, t_{uni}] \end{cases} \tag{5.28}$$

3) The black hole has not yet lost a significant portion of its angular momentum by today but $\Gamma^{-1}_{a\gamma\gamma} < t_{uni}$ and continuously adds ALPs to the cloud as they decay into photons, meaning that the number of particles stays at equilibrium values. In terms of the dynamics region 3) is equal to region 2.1),

$$\begin{cases} N(t) = e^{\Gamma_2 t} \quad \text{for} \quad t \in [0, t_{eq}] \\ N(t) = N_{eq} \quad \text{for} \quad t \in [t_{eq}, t_{uni}] \end{cases} \tag{5.29}$$

A pictorial description, illustrated in Figure 14, of the different regimes using the particular ALP parameters previously discussed, provides a better understanding of the scales involved.

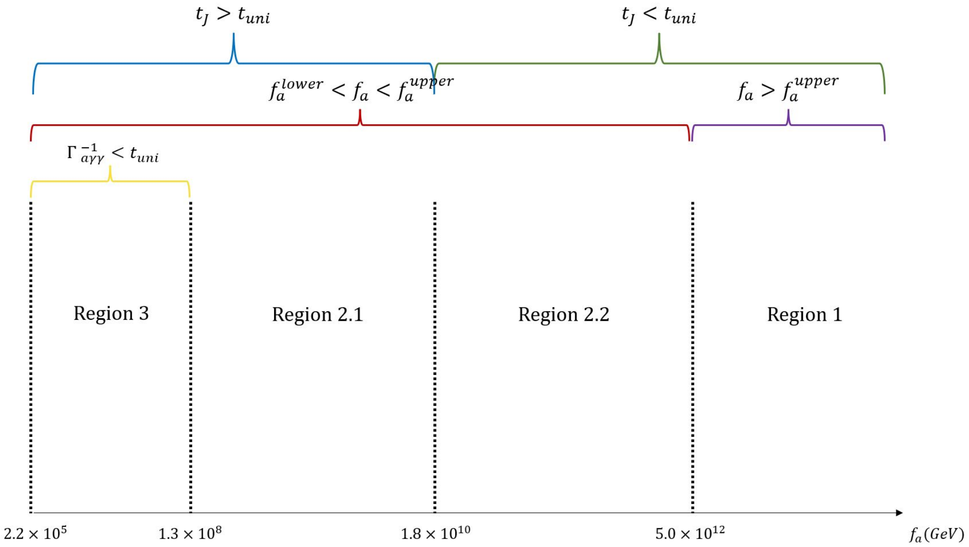
$t_J > t_{uni}$
$t_J < t_{uni}$
$f_a^{lower} < f_a < f_a^{upper}$
$f_a > f_a^{upper}$
$\Gamma^{-1}_{a\gamma\gamma} < t_{uni}$
Region 3
Region 2.1
Region 2.2
Region 1
2.2×10^5
1.3×10^8
1.8×10^{10}
5.0×10^{12}
$f_a(GeV)$

Figure 14: Different regimes for the dynamics according to the decay constant value. Here we consider $\mu = 1$ keV, $\tilde{a} = 0.01$ and $M = 10^{14}$ kg.

Now that we have separated our analysis into different parametric regimes, we present an analytical plot of the 211 state evolution for different f_a values in Figure 15. We compute the numerical *versus* analytical solutions and conclude that there is a very good matching for $f_a < 10^{11}$ GeV. However, there seems to be a large discrepancy for $f_a = 5.0 \times 10^{12}$ GeV, that is, in the far upper limit of our analysis. This requires a closer look.

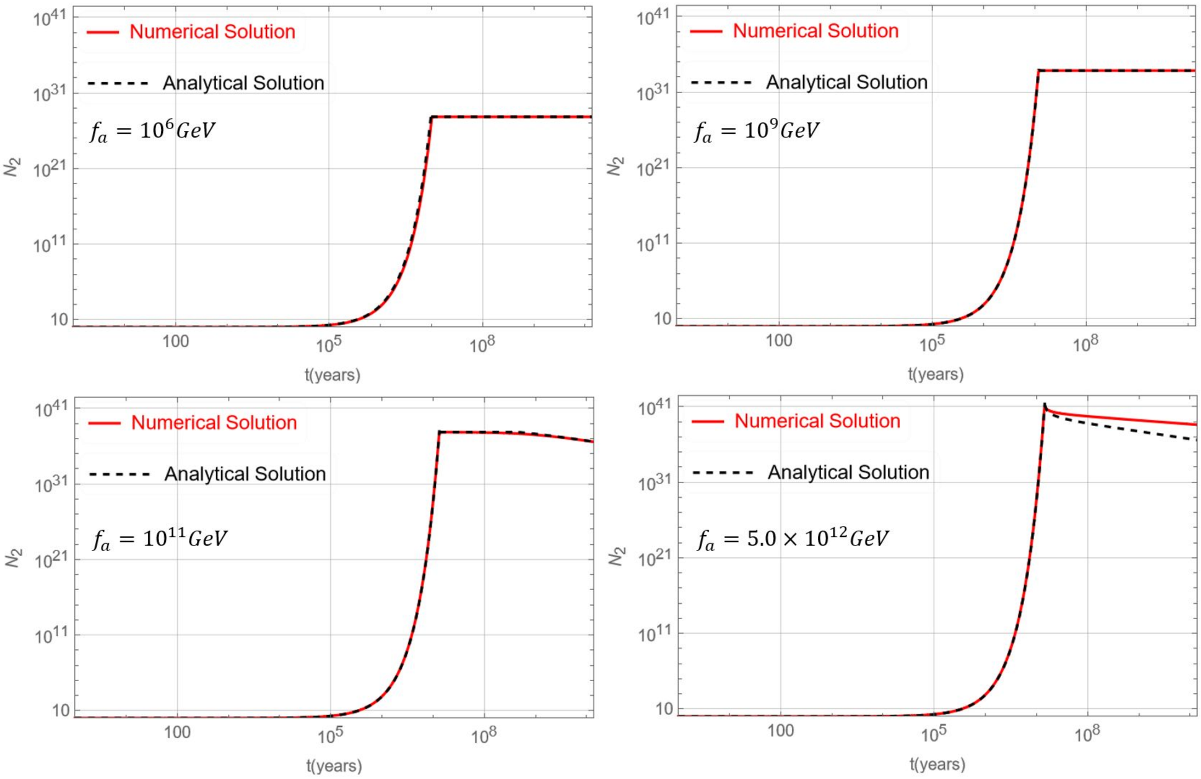

Figure 15: Contrast between numerical and analytical solutions. We obtain a fairly reasonable matching for $f_a < 10^{11}$ GeV. For higher f_a values a change in the dynamics is required.

In this case, the black hole has lost a significant amount of its angular momentum and the superradiant condition is near its saturating point ($\omega \simeq m\Omega$). At some instant, previous to t_{uni}, it must have completely saturated. From equations 5.1-5.2 we set the superradiant term to zero ensuring the superradiant saturation[25],

$$\frac{dN_2}{dt} = -2\Gamma_{22} N_2^2 N_3 + \Gamma_{33} N_3^2 N_2 \tag{5.30}$$

$$\frac{dN_3}{dt} = \Gamma_{22} N_2^2 N_3 - 2\Gamma_{33} N_3^2 N_2 \tag{5.31}$$

A closer look at Figure 12 tells us that the occupation number for both states decreases at a constant proportional rate. We therefore establish a connection between the particle number in the 211 and 322 states after saturation,

---

[25] We also neglect the decaying terms and the superradiant rate of the 322 state as previously justified.

$$N_3 = f N_2 \tag{5.32}$$

where f is the suppression constant. Inserting this in equations 5.30-5.31 and solving for f yields,

$$f \simeq \frac{\Gamma_{22}}{2\Gamma_{33}} \tag{5.33}$$

Using this result we obtain a differential equation,

$$\frac{dN_2}{dt} = -\frac{3}{4}\frac{\Gamma_{22}^2}{\Gamma_{33}} N_2^3 \tag{5.34}$$

and solving it yields,

$$N_2(t) = \frac{N_{sat}}{\left(1 + \frac{3\Gamma_{22}^2}{2\Gamma_{33}} N_{sat}(t - t_{sat} - t_{eq})\right)^{1/2}} \tag{5.35}$$

where N_{sat} is equation 5.27 evaluated at $t = t_{eq} + t_{sat}$ and t_{sat} is the instant the superradiant condition is saturated. How do we define this instant? A simple plot for $f_a = 10^{11}$ GeV can provide us the answer. If we extend the interval to 10^{16} years and plot equation 5.27 and 5.35 both starting at N_{eq} at the same time[26], we observe that the expressions match at one particular point (Figure 16).

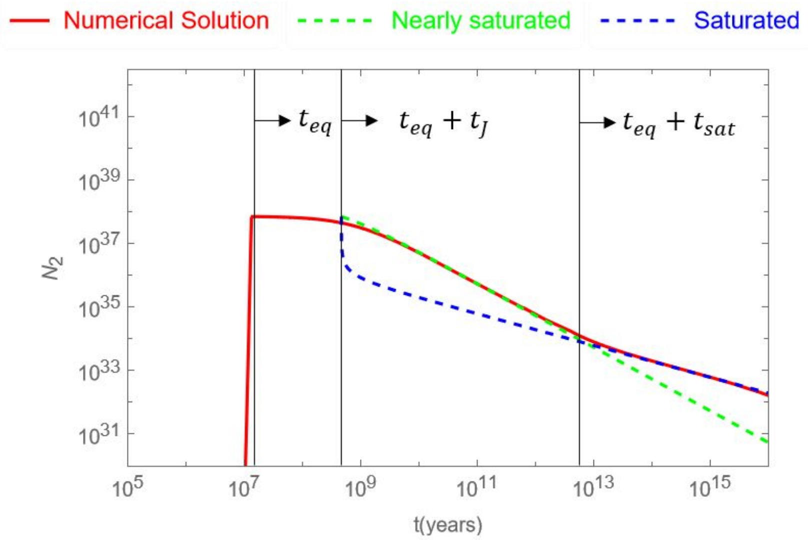

Figure 16: Numerical solution plot for $f_a = 10^{11}$ GeV (in red). We match the analytical axion number, once the superradiant condition is saturated (in blue), with the analytical axion number, once a significant amount of the black hole's angular momentum is extracted but has not yet saturated (in green). We plot both expressions starting at exactly the same point.

---

[26] We considered the instant the black hole loses a significant amount of its angular momentum, $t_{eq} + t_J$, as the starting point.

Therefore, matching equation 5.27 and 5.35 analytically provides an estimate of t_{sat}. This matching yields,

$$t_{sat} \simeq 5.4 \times 10^{12} \left(\frac{\mu}{\text{keV}}\right)^3 \left(\frac{10^{11}\text{GeV}}{f_a}\right)^4 \left(\frac{4 \times 10^{-4}}{\alpha}\right)^6 \text{years} \simeq 8.2 \times 10^{12} \text{years} \tag{5.36}$$

We then re-write the dynamics of regime/scenario 2.2) as,

$$\begin{cases} N(t) = e^{\Gamma_2 t} \quad \text{for} \quad t \in [0, t_{eq}] \\ N(t) = N_{eq} \quad \text{for} \quad t \in [t_{eq}, t_{eq} + t_J] \\ N(t) = \dfrac{N_{eq}}{1 + 2 \times 10^{-2} N_{eq} \left(\frac{M_p}{M}\right)^2 \alpha^8 \mu (t - t_J - t_{eq})} \quad \text{for} \quad t \in [t_{eq} + t_J, t_{eq} + t_{sat}] \\ N(t) = \dfrac{N_{sat}}{\left(1 + \frac{3\Gamma_{22}^2}{2\Gamma_{33}} N_{sat} (t - t_{sat} - t_{eq})\right)^{1/2}} \quad \text{for} \quad t \in [t_{eq} + t_{sat}, t_{uni}] \end{cases} \tag{5.37}$$

We re-plot this result with the numerical solution in Figure 17 where we ensure that the problem is solved. We now have a complete understanding of the analytical description of the system dynamics within the cloud.

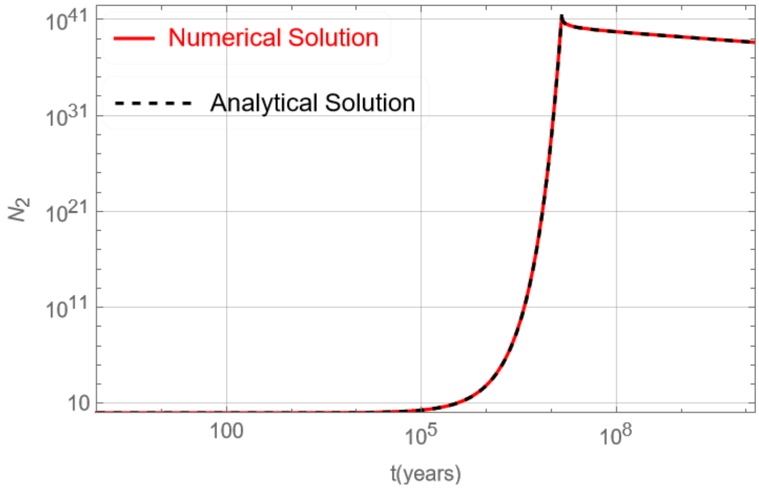

Figure 17: Numerical (red) *versus* analytical (black) plot for $f_a = 5.0 \times 10^{12}$ GeV.

To determine the errors associated with our calculations we use,

$$\%\text{error} = \frac{|\text{analytical} - \text{numerical}|}{\text{numerical}} \times 100\% \tag{5.38}$$

We evaluate the value discrepancy for different f_a values in Tables 1-4.

Table 1: Value discrepancy for the numerical and analytical solutions for the 211 occupation number with $f_a = 10^6$ GeV.

	N at $t = t_{eq}$	N at $t = t_{eq} + t_J$	N at $t = t_{eq} + t_{sat}$	N at $t = t_{uni}$
Numerical	$\simeq 6.89 \times 10^{27}$	Not reached	Not reached	$\simeq 6.89 \times 10^{27}$
Analytical	$\simeq 7.07 \times 10^{27}$	Not reached	Not reached	$\simeq 7.07 \times 10^{27}$
%error	$\simeq 2\%$	-	-	$\simeq 2\%$

Table 2: Value discrepancy for the numerical and analytical solutions for the 211 occupation number with $f_a = 10^9$ GeV.

	N at $t = t_{eq}$	N at $t = t_{eq} + t_J$	N at $t = t_{eq} + t_{sat}$	N at $t = t_{uni}$
Numerical	$\simeq 7.07 \times 10^{33}$	Not reached	Not reached	$\simeq 7.05 \times 10^{33}$
Analytical	$\simeq 7.07 \times 10^{33}$	Not reached	Not reached	$\simeq 7.07 \times 10^{33}$
%error	$\ll 1\%$	-	-	$\ll 1\%$

Table 3: Value discrepancy for the numerical and analytical solutions for the 211 occupation number with $f_a = 10^{11}$ GeV.

	N at $t = t_{eq}$	N at $t = t_{eq} + t_J$	N at $t = t_{eq} + t_{sat}$	N at $t = t_{uni}$
Numerical	$\simeq 7.06 \times 10^{37}$	$\simeq 6.60 \times 10^{37}$	Not reached	$\simeq 3.77 \times 10^{36}$
Analytical	$\simeq 7.07 \times 10^{37}$	$\simeq 7.07 \times 10^{37}$	Not reached	$\simeq 3.76 \times 10^{36}$
%error	$\ll 1\%$	$\simeq 6\%$	-	$\ll 1\%$

Table 4: Value discrepancy for the numerical and analytical solutions for the 211 occupation number with $f_a = 5.0 \times 10^{12}$ GeV.

	N at $t = t_{eq}$	N at $t = t_{eq} + t_J$	N at $t = t_{eq} + t_{sat}$	N at $t = t_{uni}$
Numerical	$\simeq 9.28 \times 10^{40}$	$\simeq 4.26 \times 10^{40}$	$\simeq 3.13 \times 10^{40}$	$\simeq 4.15 \times 10^{38}$
Analytical	$\simeq 1.76 \times 10^{41}$	$\simeq 1.76 \times 10^{41}$	$\simeq 3.49 \times 10^{40}$	$\simeq 4.16 \times 10^{38}$
%error	$\simeq 90\%$	$\simeq 300\%$	$\simeq 11\%$	$\ll 1\%$

5.1.5 Axions outside the cloud

In the previous section we studied the system dynamics in the presence of self-interactions within the cloud. As observed, self-interactions do not allow the cloud to grow arbitrarily large, which then fixes an equilibrium particle number. But what about outside the cloud? From Figure 9 we know that a fraction of the axions escape the black hole's gravitational potential. These axions become free and, depending on their velocity, they might be bound to our galaxy. These axions should be taken into consideration when computing flux calculations. From Figure 9 b) and through energy conservation, the particles that become free possess,

$$E_\infty = \frac{\alpha^2}{72}\mu \tag{5.39}$$

Since these axions become free, this resulting energy is purely kinetic. In a non-relativistic analysis,

$$v = \frac{\alpha}{6} \tag{5.40}$$

For the parameter space (Figure 10) we are studying $\alpha \lessapprox 2 \times 10^{-3}$,

$$v \lessapprox 100\,\mathrm{kms}^{-1} \tag{5.41}$$

where we conclude that this velocity is lower than the Milky Way's escape velocity [60] $\simeq 497\,\mathrm{kms}^{-1}$, which ensures that the particles are bound to our galaxy. A subtle detail in this analysis is that, even though this is difficult to measure, the photon energy detected in this case would be slightly different from the axions bound to the black hole. This is due to the fact that the photon energy is half the axion's energy and not exactly the axion's mass. Therefore, if they are bound to the black hole, the energy detected is smaller. Nevertheless, the difference is $\mathcal{O}(\alpha^2)$ and since $\alpha \ll 1$ this difference is practically negligible.

Let us now try to estimate the axion number that escapes the black hole's gravitational potential. We construct an additional equation for our dynamics,

$$\frac{dN_\infty}{dt} = \Gamma_{33} N_3^2 N_2 - \Gamma_{a\gamma\gamma} N_\infty \tag{5.42}$$

We plot numerical simulations for the particular ALP we were previously considering for different f_a values in Figure 18. In the initial moments, the number of axions that become free, N_∞, seems to have a similar growth rate steepness as N_3 until 211 and 322 eventually reach equilibrium. However, when this equilibrium is achieved, N_∞ seems to continue its very steep growth until $N_\infty \simeq N_{eq}$. Afterwards, it continues to grow but at a significantly smaller rate. We are not particularly interested in how this number evolves throughout the cosmic history, but rather in how it evolves after equilibrium is reached. There seems to be two restrictive factors for the N_∞ growth rate: the decay rate and the black hole's significant loss of angular momentum. When the decay rate is negligible,

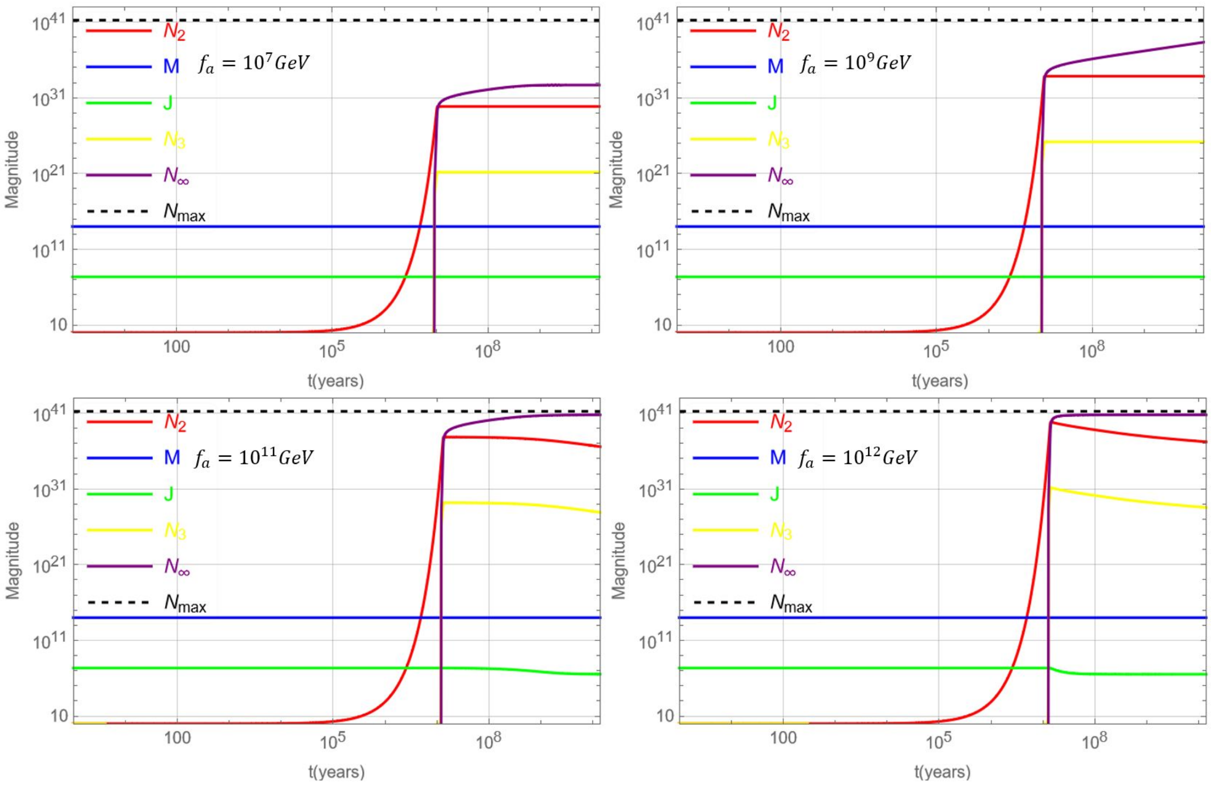

Figure 18: Numerical solutions considering $\mu = 1$keV, $M = 10^{14}$kg and $\tilde{a} = 0.01$.

$$\frac{dN_\infty}{dt} \simeq \Gamma_{33} N_3^2 N_2 \tag{5.43}$$

where N_2 and N_3 are evaluated at equilibrium. Integrating this equation, and assuming $N_{\infty_{initial}} \simeq N_{eq}$, yields,

$$N_\infty(t) = N_{eq} + 3.0 \times 10^{35}(\tilde{a} - 4\alpha)^{3/2}\Big(\frac{f_a}{10^{11}\text{GeV}}\Big)^2\Big(\frac{\text{keV}}{\mu}\Big)\Big(\frac{\alpha}{4 \times 10^{-4}}\Big)^7(t - t_{eq})\text{years}^{-1} \quad (5.44)$$

The decay rate is relevant when,

$$\Gamma_{a\gamma\gamma}N_\infty > \Gamma_{33}N_3^2N_2 \quad (5.45)$$

which yields,

$$N_\infty > 9.4 \times 10^{51}(\tilde{a} - 4\alpha)^{3/2}\Big(\frac{\alpha}{4 \times 10^{-4}}\Big)^7\Big(\frac{f_a}{10^{11}\text{GeV}}\Big)^4\Big(\frac{\text{keV}}{\mu}\Big)^4 \quad (5.46)$$

We can estimate the instant the decay rate starts to suppress N_∞'s growth. Eventually, equations 5.46 and 5.44 will match at $t = t_{decay}$, yielding,

$$t_{decay} \simeq 3.1 \times 10^{16}\Big(\frac{f_a}{10^{11}\text{GeV}}\Big)^2\Big(\frac{\text{keV}}{\mu}\Big)^3\text{years} \quad (5.47)$$

Now, we envisage a f_a parameter space for which the decay rate is relevant within the universe timeline, $t_{uni} > t_{decay}$,

$$f_a < 6.5 \times 10^7\Big(\frac{\mu}{\text{keV}}\Big)^{3/2}\text{GeV} \quad (5.48)$$

From Figure 18 we conclude that once the decay rate becomes negligible, N_∞ grows at a constant rate as long as $t_J < t_{uni}$. For regimes where $t_J > t_{uni}$ the growth is suppressed once a significant amount of the black hole's angular momentum is lost. After this instant, N_∞ seems to reach an equilibrium slightly lower than N_{max}. How do we estimate this number? From Figure 9 we know that a fraction of axions go back into the black hole. We can construct a similar equation accounting for the rate of this process,

$$\frac{dN_{BH}}{dt} = \Gamma_{22}N_2^2N_3 \quad (5.49)$$

We now compute the fraction of both rates at equilibrium,

$$\frac{\Gamma_{33}N_2N_3^2}{\Gamma_{22}N_2^2N_3}\Big|_{\text{at eq}} = \frac{1}{2} \quad (5.50)$$

The rate at which the axions go back into the black hole is twice the rate at which they become free. Through conservation, the sum of both quantities should be equal to N_{max} which means that $N_\infty \simeq \frac{N_{max}}{3}$.

In a similar way to what was previously done, let us try to compute an analytical description of the free axion number evolution. First, we provide a pictorial description for the particular ALP we have been studying in Figure 19.

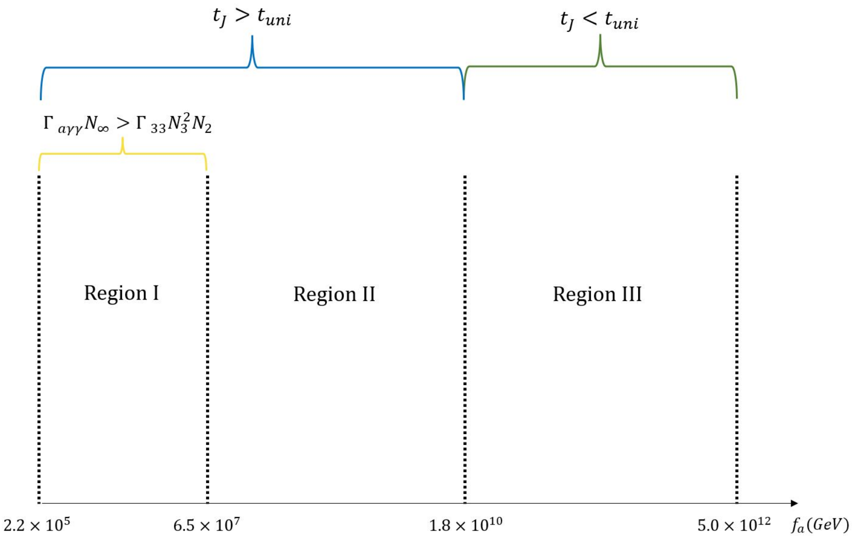

Figure 19: Different regimes for the dynamics of N_∞ according to the decay constant value considering $\mu = 1$ keV, $M = 10^{14}$ kg and $\tilde{a} = 0.01$.

For region I, we expect N_∞ to grow until a certain threshold value, forced by the decay rate, where it remains stable,

$$\begin{cases} N(t) = N_{eq} + \dfrac{3.0 \times 10^{35}}{(\tilde{a} - 4\alpha)^{-3/2}} \left(\dfrac{f_a}{10^{11}\mathrm{GeV}}\right)^2 \left(\dfrac{\mathrm{keV}}{\mu}\right) \left(\dfrac{\alpha}{4 \times 10^{-4}}\right)^7 (t - t_{eq})\mathrm{years}^{-1} \quad \text{for} \quad t \in [t_{eq}, t_{decay}] \\ N(t) = 9.4 \times 10^{51} (\tilde{a} - 4\alpha)^{3/2} \left(\dfrac{\alpha}{4 \times 10^{-4}}\right)^7 \left(\dfrac{f_a}{10^{11}\mathrm{GeV}}\right)^4 \left(\dfrac{\mathrm{keV}}{\mu}\right)^4 \quad \text{for} \quad t \in [t_{decay}, t_{uni}] \end{cases} \tag{5.51}$$

For region II, we expect N_∞ to grow at a steady rate since the decay rate is negligible and it never reaches N_{max},

$$\begin{cases} N(t) = N_{eq} + \dfrac{3.0 \times 10^{35}}{(\tilde{a} - 4\alpha)^{-3/2}} \left(\dfrac{f_a}{10^{11}\mathrm{GeV}}\right)^2 \left(\dfrac{\mathrm{keV}}{\mu}\right) \left(\dfrac{\alpha}{4 \times 10^{-4}}\right)^7 (t - t_{eq})\mathrm{years}^{-1} \quad \text{for} \quad t \in [t_{eq}, t_{uni}] \end{cases} \tag{5.52}$$

For region III, we expect N_∞ to grow being eventually suppressed when the black hole loses a significant amount of its angular momentum,

$$\begin{cases} N(t) = N_{eq} + \dfrac{3.0 \times 10^{35}}{(\tilde{a} - 4\alpha)^{-3/2}} \left(\dfrac{f_a}{10^{11}\mathrm{GeV}}\right)^2 \left(\dfrac{\mathrm{keV}}{\mu}\right) \left(\dfrac{\alpha}{4 \times 10^{-4}}\right)^7 (t - t_{eq})\mathrm{years}^{-1} \quad \text{for} \quad t \in [t_{eq}, t_J] \\ N(t) = \dfrac{N_{max}}{3} \quad \text{for} \quad t \in [t_J, t_{uni}] \end{cases} \tag{5.53}$$

Notice that for large μ values there is a possibility that region I is extended overlapping region III. Nevertheless, in this scenario equations 5.53 hold. Now that we managed to compute an analytical description of the free axion number evolution, we plot analytical *versus* numerical results in Figure 20. Since we are ultimately interested in this number as of today, we estimate numerically and analytically N_∞ at $t = t_{uni}$ for various f_a values inserted in different regions. We estimate the error of our results in Table 5 where we obtain an excellent match.

Table 5: Value discrepancy for the numerical and analytical solutions for N_∞ at $t = t_{uni}$ for various f_a values.

	$f_a = 10^7$ GeV	$f_a = 10^9$ GeV	$f_a = 10^{11}$ GeV	$f_a = 10^{12}$ GeV
Numerical	$\simeq 4.81 \times 10^{32}$	$\simeq 2.11 \times 10^{38}$	$\simeq 5.96 \times 10^{40}$	$\simeq 5.98 \times 10^{40}$
Analytical	$\simeq 4.82 \times 10^{32}$	$\simeq 2.04 \times 10^{38}$	$\simeq 5.98 \times 10^{40}$	$\simeq 5.98 \times 10^{40}$
%error	$\ll 1\%$	$\simeq 3\%$	$\ll 1\%$	$\ll 1\%$

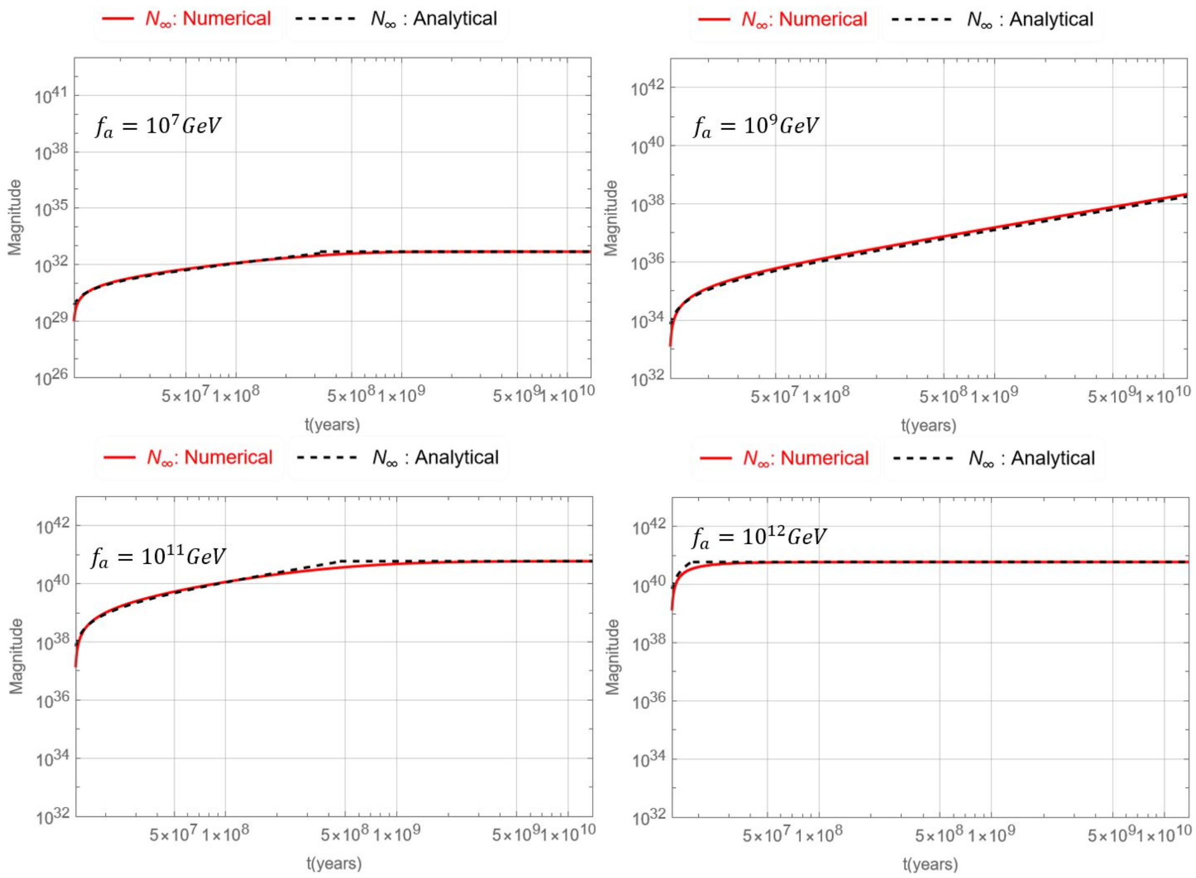

Figure 20: Contrast between numerical and analytical solutions for the number of free axions considering $\mu = 1$ keV, $M = 10^{14}$ kg and $\tilde{a} = 0.01$.

This analysis is important because it shows that one can produce a vastly larger number of axions outside the cloud at lower f_a values than within the cloud. Since photon flux values are ultimately a fraction N/f_a^2, a larger axion number at smaller f_a values produces a significantly larger flux.

5.2 Bosenova

We have so far followed the perturbative, non-relativistic approach in [4] to study the dynamics of superradiant axion clouds, which should hold for $\alpha \ll 1$. For larger values of α (within the superradiant regime) this approach may no longer be accurate, but self-interactions should nevertheless halt the growth of superradiant axion clouds when the leading quartic interaction term $\frac{\lambda\Psi^4}{4!}$ becomes comparable to the axion mass term in the Lagrangian $\frac{\mu^2\Psi^2}{2}$, at a field value,

$$\Psi_B^2 = 12f_a^2 \tag{5.54}$$

When the field reaches this value, the non-linear effects of the attractive self-interactions cause a gradual concentration of the axion field configuration leading to a dynamical collapse usually known as bosenova [61, 62]. This phenomena decreases the field value back to the linear superradiant regime where it grows again to the bosenova value. The number density[27] is,

$$n = \frac{N}{V} = \mu\Psi^2 \tag{5.55}$$

where N is the axion number and V the cloud volume. Using the bosenova field value and the cloud volume (equation 2.58) we obtain,

$$N_B = \frac{600\pi^2}{\alpha^3}\left(\frac{f_a}{\mu}\right)^2 \tag{5.56}$$

In terms of the dynamics, we can only assume that the cloud has an exponential growth until it reaches the bosenova number where it remains approximately stable. Comparing the bosenova number with the equilibrium value yields,

$$\frac{N_{eq}}{N_B} \simeq 5\times 10^{-3}\sqrt{\tilde{a}-4\alpha}\,\alpha^2 \tag{5.57}$$

In order to distinguish this case from the equilibrium one, which considers a non-relativistic approach [4], we require larger α values,

$$\alpha \gtrapprox 0.1 \tag{5.58}$$

---

[27] This is obtained from the energy momentum tensor in the non-relativistic limit.

Nevertheless, since $\alpha < 1$, we conclude that the bosenova number is larger than the equilibrium value. We are not particularly interested in this analysis due to the fact that we cannot establish an accurate description of the cloud's growth throughout the cosmic history. However, for the sake of completeness, we will also consider this number, assuming that it stays roughly constant until today as long as $\Gamma_{a\gamma\gamma}^{-1} > t_{uni}$, when we estimate photon fluxes in the next section.

6 Electromagnetic signatures of superradiant axion clouds

In this section we estimate the photon flux emitted within and outside the axion cloud, considering a system made of a rotating PBH, assuming it to be a relevant fraction of the DM, that copiously produces “heavy” axions, which decay into photon pairs, in the presence of interactions between superradiant states. We will cover two options for this calculation: the flux from the center of our galaxy, where we use the Navarro-Frenk-White (NFW) dark matter density profile, and the extragalactic background flux. We then compare our results with observational data.

6.1 Photon emission from bound axions

In this subsection we estimate the photon flux emitted within the cloud taking into consideration the dynamics induced by the interactions between superradiant states and the bosenova effect. We estimate the flux emitted from the Milky Way as well as the extragalactic background flux and compare them with observational data.

6.1.1 Milky Way’s galactic center photon flux

Assuming that black holes within the considered mass range represent 100% of the DM, the differential photon flux produced by axion decay is [63],

$$\frac{d\phi}{dE} = \frac{1}{4\pi}\Big(\frac{1}{M_{PBH}}\Big)\frac{J_D}{\Delta\Omega}\frac{dN}{dEdt} \tag{6.1}$$

where we take into account the number of PBHs (represented by $\frac{1}{M_{PBH}}$) and the J-factor, J_D, accounts for the amount of DM one is looking at and depends on the choice of the DM density profile. Its value can be obtained integrating [64],

$$J(\Delta\Omega) = \int_{\Delta\Omega} d\Omega \int_0^\infty \rho[r(l,\Omega)]dl \tag{6.2}$$

which is an integral of the density profile, $\rho[r(l,\Omega)]$, that runs along the line-of-sight, l, integrated over a certain solid angle $\Delta\Omega$. A sketch of the geometry of the problem is illustrated

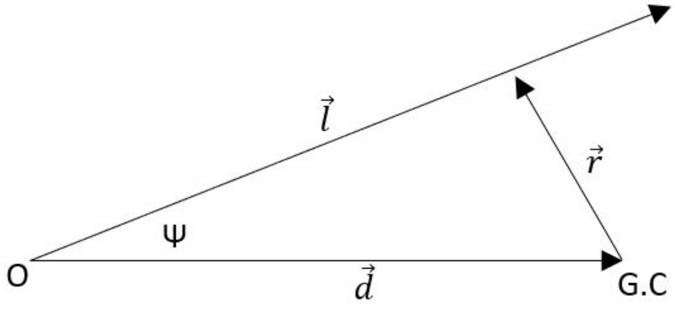

Figure 21: Sketch of the geometry.

in Figure 21. Geometrically, the observer is located at O and is looking along the line-of-sight, $\vec{l}$, that is separated from the straight line, $\vec{d}$, separating the observer and the galactic centre, $G.C$. Furthermore, the angle Ψ connects the observer and the centre of the halo. This way, $\vec{r}$ connects the centre of the halo with the line-of-sight. We use the NFW density profile [64],

$$\rho(r) = \frac{\rho_s}{\frac{r}{r_s}\left(1+\frac{r}{r_s}\right)^2} \tag{6.3}$$

where ρ_s and r_s are the scale density and scale radius, respectively, which are characteristic of individual halos. According to the geometry of the problem, one just has to write r as a function of l, d and Ψ in order to write the density profile as a function of these variables to integrate equation 6.2,

$$r = \sqrt{l^2 + d^2 - 2ld\cos\Psi} \tag{6.4}$$

which yields,

$$\rho[r(l,\Psi)] = \frac{\rho_s r_s^3}{\sqrt{l^2+d^2-2ld\cos\Psi}(r_s + \sqrt{l^2+d^2-2ld\cos\Psi})^2} \tag{6.5}$$

Considering,

$$d\Omega = 2\pi \sin\Psi d\Psi \tag{6.6}$$

and the 40 arcsec region around the galactic center [64], as well as $\rho_s = 0.4\,\text{GeVcm}^{-3}$, $r_s = 21\,\text{kpc}$ and $d = 8\,\text{kpc}$, we integrate numerically using *Wolfram Mathemathica*, yielding,

$$J \simeq 5.54\times 10^{16}\,\text{GeVcm}^{-2} \tag{6.7}$$

As for the emission spectrum, $\frac{dN}{dEdt}$, and since the axions are non-relativistic as concluded from equation 2.55, we consider that the photons are emitted with an energy $E_\gamma \simeq \frac{\mu}{2}$. We then consider a monochromatic distribution [11] with a fixed energy, meaning that $\frac{dN}{dEdt} \simeq$

$2N\Gamma_{a\gamma\gamma}\delta(E-E_\gamma)$. Here, N is the axion number and $\Gamma_{a\gamma\gamma}$ the axion decay rate which is given by equation B.15. The observed flux over an energy band spanning the range (E_1, E_2) is,

$$\phi = \int_{E_1}^{E_2} \frac{d\phi}{dE} dE \tag{6.8}$$

Therefore, and multiplying[28] by $\Delta\Omega$, equation 6.1 may be re-written as,

$$\phi = \frac{J_D}{4\pi M_{PBH}} \int_{E_1}^{E_2} 2N\Gamma_{a\gamma\gamma}\delta(E-E_\gamma) dE \tag{6.9}$$

where we conclude that,

$$\phi = \frac{J_D}{2\pi M_{PBH}} N\Gamma_{a\gamma\gamma} \tag{6.10}$$

To determine whether or not the flux estimates are strong enough to surpass the observational data, we test the regime that maximizes axion numbers within the cloud. More precisely, and as previously anticipated from Figure 13, we are particularly interested in the regime where an equilibrium is reached and the number of particles remains approximately stable within the age of the universe, since this is the regime that produces a larger N_2/f_a^2 fraction and, hence, larger flux values. We substitute the number of axions within the cloud with two options: the equilibrium value, N_{eq} (equation 5.8), and the bosenova value, N_B (equation 5.56). Introducing these in equation 6.10 yields,

$$\phi_{eq} \simeq 2.2 \times 10^{-7} |C_{a\gamma\gamma}|^2 \sqrt{\tilde{a} - 4\alpha} \left(\frac{J_D}{10^{16}\mathrm{GeVcm}^{-2}} \right) \left(\frac{10^{14}\mathrm{kg}}{M} \right)^2 \mathrm{ph\ m^{-2}s^{-1}} \tag{6.11}$$

$$\phi_B \simeq 4.5 \times 10^{-3} |C_{a\gamma\gamma}|^2 \left(\frac{10^{-1}}{\alpha} \right)^2 \left(\frac{J_D}{10^{16}\mathrm{GeVcm}^{-2}} \right) \left(\frac{10^{14}\mathrm{kg}}{M} \right)^2 \mathrm{ph\ m^{-2}s^{-1}} \tag{6.12}$$

where ϕ_{eq} is the flux associated with the equilibrium analysis and ϕ_B with the bosenova analysis. We conclude that for the same parameters used the bosenova flux is greatly enhanced. Nevertheless, for the QCD axion, where the black hole masses are required to be much higher (Figure 11), the flux in both cases is very small and, henceforth, we only consider ALPs. We want to compare these estimates with the observational data given in Figure 22. Even though it only shows a small range for the X-ray particle decay ([2 − 30] keV), from reference[29] [65] we know that for larger masses the observational photon flux decreases at a constant rate as apparent in Figure 22. For ALPs, in the equilibrium analysis, there are no flux estimates greater than the observational data. However, for the bosenova analysis, some values surpass this threshold. Fixing[30] $M = 10^{14}$ kg, $\tilde{a} = 0.9$ and $|C_{a\gamma\gamma}| = 1$, we envisage a parameter space in which the flux estimated exceeds the observational data thus excluding the particular parameters assumed. Results are illustrated in Figure 23.

---

[28] We do this because we want to compare with observational data that is in units of ph m^{-2} s^{-1}.

[29] In this paper the bounds are written in terms of the decaying time of the DM candidate which is nearly constant within the X-rays range.

[30] For this analyses to hold we require $\alpha \gtrapprox 0.1$, hence, higher spins.

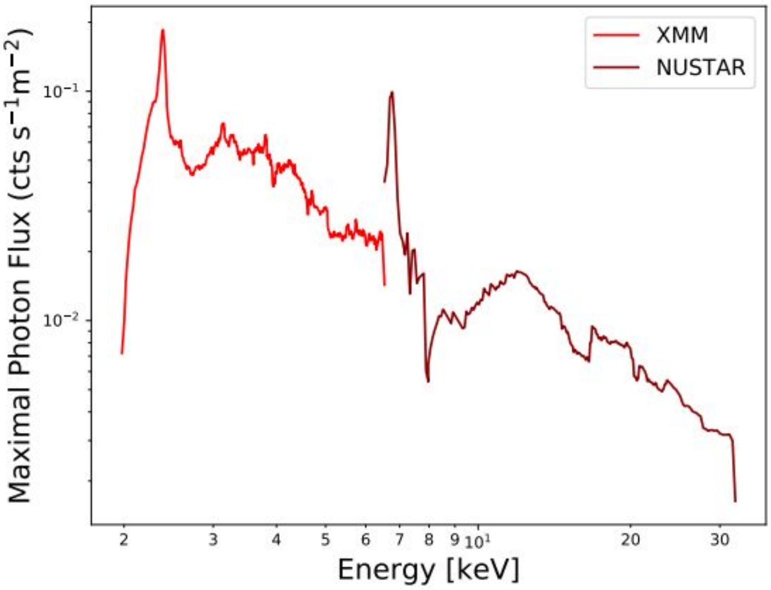

Figure 22: Experimental data of the intensity flux bound for the XMM-NuSTAR observation, for $[2-30]$ keV range X-ray particle decay. Plot taken from [64].

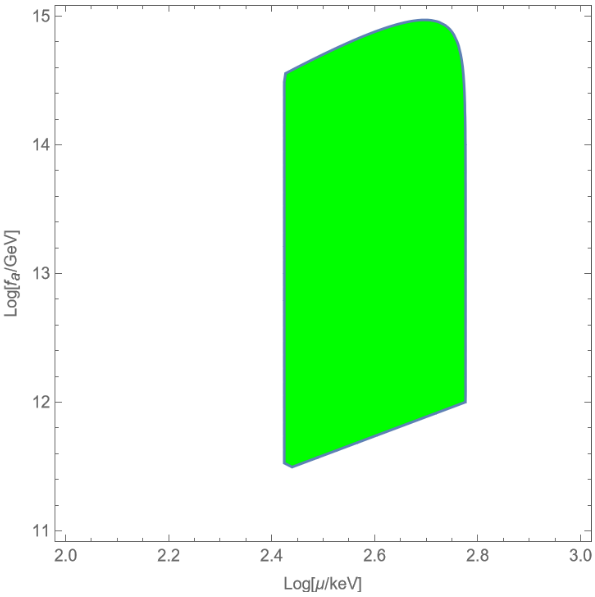

Figure 23: Parameter space for which the galactic center photon flux estimate exceeds the observational data in the bosenova analysis, and is therefore excluded. Parameters assumed: $\tilde{a} = 0.9$, $|C_{a\gamma\gamma}| = 1$, $M = 10^{14}$ kg and $\alpha > 0.1$.

Notice that these flux estimates could be vastly enhanced if we considered dwarf spheroidal galaxies such as Draco or Fornax which possess larger DM densities, and hence larger J-factors [66]. However, there is currently no observational data with which we can compare our theoretical estimates, so we restricted our analysis to the Milky Way.

6.1.2 Extragalactic background photon flux

In order to estimate the extragalactic background flux one usually assumes that the distribution of PBHs is isotropic [11]. This produces an isotropic photon flux resulting from the decay of axions produced by superradiant instabilities. The flux measured today will be a superposition of all photons emitted since the very beginning of the process[31], resulting in a broadening of the spectrum. The emission rate per volume per unit solid angle ($\mathrm{cm}^{-3}\mathrm{s}^{-1}\mathrm{sr}^{-1}$) at a cosmological time t is given by [11],

$$\frac{dn_\gamma}{dt}(E_\gamma, t) \simeq \frac{1}{4\pi} n_{PBH}(t) E_\gamma \frac{dN_\gamma}{dE_\gamma dt}(E_\gamma, t) \tag{6.13}$$

where n_{PBH} is the PBH number density. Experimentally, one measures the photon flux in an energy interval $\Delta E \simeq E$ [67], which means that the flux can be written as,

$$I = \frac{dI}{dE}\Delta E \simeq \frac{dI}{dE} E \tag{6.14}$$

To use the data illustrated in Figure 24, and to compare it with our estimates, we must consider the intensity as a function of the wavelength which means that equation 6.14 must be written as,

$$I \simeq -\frac{dI}{d\lambda}\lambda^2 \frac{1}{\lambda} = -\frac{dI}{d\lambda}\lambda \tag{6.15}$$

and, equivalently, equation 6.13 as,

$$\frac{dn_\gamma}{dt}(\lambda_\gamma, t) \simeq -\frac{1}{4\pi} n_{PBH}(t) \lambda_\gamma \frac{dN_\gamma}{d\lambda dt}(\lambda_\gamma, t) \tag{6.16}$$

Recall that due to the universe's expansion, and if one wants to consider the flux measured today, one must account for the redshift factor of the wavelength and densities, $(1+z)$ and $(1+z)^{-3}$, respectively. The PBH number density can be written as,

$$n_{\mathrm{PBH}}(t) = \Omega^0_{\mathrm{PBH}} \frac{\rho^0_c}{M} (1+z)^3 \tag{6.17}$$

---

[31] In fact, only photons emitted after recombination are important. Nevertheless, this will not be relevant for our analysis due to the large timescales involved.

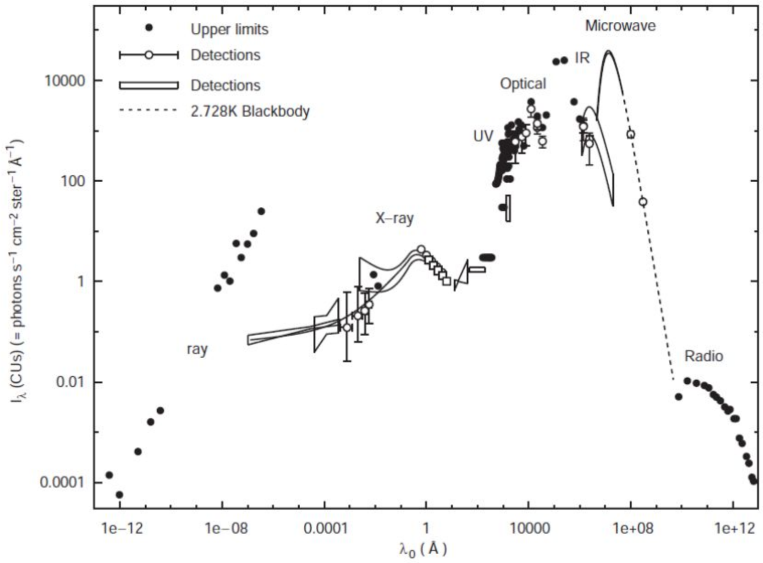

Figure 24: Extragalactic background photon flux. Plot and data taken from [68].

where $\Omega^0_{PBH} = f_{DM}\Omega_{CDM}$ is the PBH abundance (which is a function of the DM fraction in PBHs, f_{DM}, and the cold DM abundance, Ω_{CDM}) and $\rho^0_c \simeq 9.47 \times 10^{-33}\,\mathrm{kg\,cm^{-3}}$ is the critical density of the universe, both measured as of today. This leads to,

$$n^0_\gamma(\lambda^0_\gamma) = -\frac{1}{4\pi}\Omega^0_{PBH}\rho^0_c\lambda^0_\gamma \int dt \frac{1}{(1+z)M(t)}\frac{dN_\gamma}{d\lambda dt} \tag{6.18}$$

As previously stated, we consider the emission spectrum relation [11],

$$\frac{dN_\gamma}{dEdt} \simeq 2N\Gamma_{a\gamma\gamma}\delta(E - E_\gamma) \tag{6.19}$$

which for our analysis must be re written as,

$$\frac{dN_\gamma}{d\lambda dt} = -2N\Gamma_{a\gamma\gamma}\delta(\lambda - \lambda_\gamma) \tag{6.20}$$

Introducing this result in equation 6.18 we get,

$$n^0_\gamma(\lambda^0_\gamma) = \frac{1}{2\pi}\Omega^0_{PBH}\rho^0_c\lambda^0_\gamma\Gamma_{a\gamma\gamma} \int dt \frac{N(t)}{(1+z)M(t)}\delta(\lambda - \lambda_\gamma) \tag{6.21}$$

According to the time scales we are considering all relevant photons are emitted in the CDM dominated era, for which $(1+z)^{-1} = (\frac{t}{t^0})^{2/3}$. So, the present photon flux in $\mathrm{cm^{-2}s^{-1}sr^{-1}}$ units is,

$$I(\lambda^0) = \frac{c}{2\pi}\Omega^0_{PBH}\rho^0_c\lambda^0_\gamma\Gamma_{a\gamma\gamma} \int_{t_{recomb}}^{t_{today}} dt \Big(\frac{t}{t^0}\Big)^{2/3} \frac{N(t)}{M(t)}\delta(\lambda - \lambda_\gamma) \tag{6.22}$$

Notice that,

$$\left(\frac{t}{t^0}\right)^{2/3} = \frac{\lambda}{\lambda_\gamma^0} \qquad \Longrightarrow \qquad dt = \frac{3t^0}{2}(\lambda_\gamma^0)^{-3/2}\lambda^{1/2}d\lambda \tag{6.23}$$

Inserting this into equation 6.22 and after integration,

$$I(\lambda^0) = \frac{3c}{4\pi}\Omega_{PBH}^0\rho_c^0 t^0 \Gamma_{a\gamma\gamma}\left(\frac{\lambda_\gamma}{\lambda_\gamma^0}\right)^{3/2}\frac{N(t)}{M(t)}\Big|_{t=t(\lambda_\gamma^0)} \tag{6.24}$$

In order to get the spectral flux and to compare our results with Figure 24 we calculate the derivative of the latter equation with respect to the wavelength as of today, $\frac{dI}{d\lambda_\gamma^0}$,

$$\left|\frac{dI}{d\lambda_\gamma^0}\right| = \frac{9c}{8\pi}\Omega_{PBH}^0\rho_c^0 t^0 \Gamma_{a\gamma\gamma}\left(\frac{\lambda_\gamma}{\lambda_\gamma^0}\right)^{3/2}\frac{N(t)}{M(t)}\Big|_{t=t(\lambda_\gamma^0)}\frac{1}{\lambda_\gamma^0} \tag{6.25}$$

Recall that $N(t)$ and $M(t)$ are the axion number and the black hole's mass, respectively, in the instant the photons are emitted. We know that the axion number's growth is extremely steep as soon as the superradiant instability is triggered and the black hole's mass is approximately constant throughout the process (Figure 12). To determine whether or not the flux estimates are strong enough to surpass the observational data, we test the regime that maximizes axion numbers within the cloud. We re-write equation 6.25 in terms of the fundamental parameters considering the general axion decay rate (equation B.15) the equilibrium value, N_{eq} (equation 5.8), and the bosenova value, N_B (equation 5.56). We also ease this calculation considering the flux values for photons emitted today, which possess lower wavelengths, and hence a larger differential flux value. For the equilibrium differential flux we obtain,

$$\left|\frac{dI}{d\lambda_\gamma^0}\right|_{eq} = 1.7\times10^{-5}\sqrt{\tilde{a}-4\alpha}\left(\frac{\mu}{\text{keV}}\right)\left(\frac{10^{14}\text{kg}}{M}\right)^2|C_{a\gamma\gamma}|^2\ \text{ph cm}^{-2}\text{s}^{-1}\text{sr}^{-1}\mathring{A}^{-1} \tag{6.26}$$

and considering equation 5.57, we obtain the bosenova differential flux,

$$\left|\frac{dI}{d\lambda_\gamma^0}\right|_{B} = 3.5\times10^{-1}\left(\frac{10^{-1}}{\alpha}\right)^2\left(\frac{\mu}{\text{keV}}\right)\left(\frac{10^{14}\text{kg}}{M}\right)^2|C_{a\gamma\gamma}|^2\ \text{ph cm}^{-2}\text{s}^{-1}\text{sr}^{-1}\mathring{A}^{-1} \tag{6.27}$$

where we conclude that the bosenova differential flux is vastly enhanced. Similarly to what we concluded in the previous subsection, for the QCD axion, where the black hole masses are required to be much larger, flux values seems to be much lower than observational data. Furthermore, in this particular region (around the microwave range in Figure 24) the observational constraints are much weaker. As for ALPs, regarding the equilibrium analysis, there are still no parameter values capable of producing a large enough flux to surpass the observational data. However, in the bosenova analysis, some parameter values seem to surpass this threshold. We envisage a parameter space in which we obtain flux values greater than the threshold providing an exclusion of the particular parameters assumed. Results are illustrated in Figure 25. Notice that the constraints are practically indistinguishable from the ones obtained for the galactic center in Figure 23. The reason is that the assumption assumed when computing the bosenova analysis ($\alpha > 0.1$) is the dominant condition.

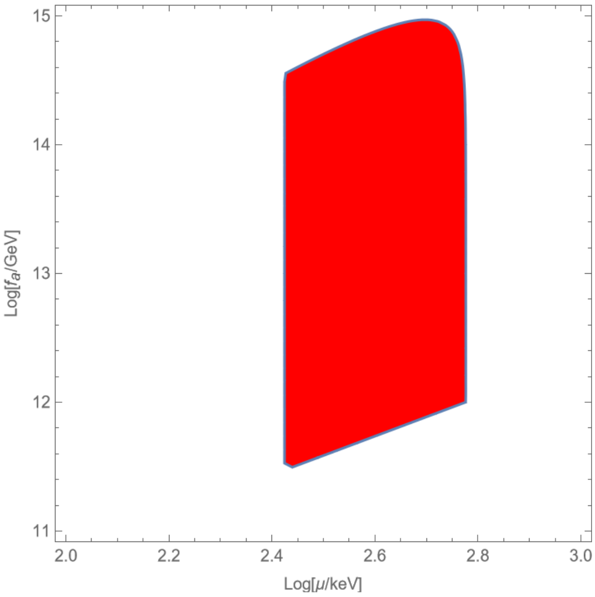

Figure 25: Parameter space for which the extragalactic background photon flux exceeds the observational data in the bosenova analysis, and is therefore excluded. Parameters assumed: $\tilde{a} = 0.9$, $|C_{a\gamma\gamma}| = 1$, $M = 10^{14}$ kg and $\alpha > 0.1$.

6.2 Photon emission from free axions

In section 5 we concluded that the axion number outside the cloud is vastly larger than within the cloud for a wide f_a range (Figure 18). The axion number enhancement at smaller f_a values may provide a large enough flux capable of surpassing observational data. In the previous section we provided a thorough analysis of the methods used to compare estimates with observational data from the Milky Way's galactic center and the extragalactic background photon fluxes. Now, we consider a more straightforward method of using existing bounds on the axion-photon coupling in the literature, which take into account both the galactic centre and the extragalactic background emission (Figure 26).

We are particularly interested in masses within the X-ray range[32] since these represent

---

[32] Throughout our main analysis we assumed low spin values, hence, small α which, for a fixed black hole mass, $M = 10^{14}$ kg, justifies lower axion masses within the keV range. The results obtained in the bosenova regime, which is a secondary analysis, forced us to consider heavier axions (within the gamma ray range) due to the $\alpha > 0.1$ condition.

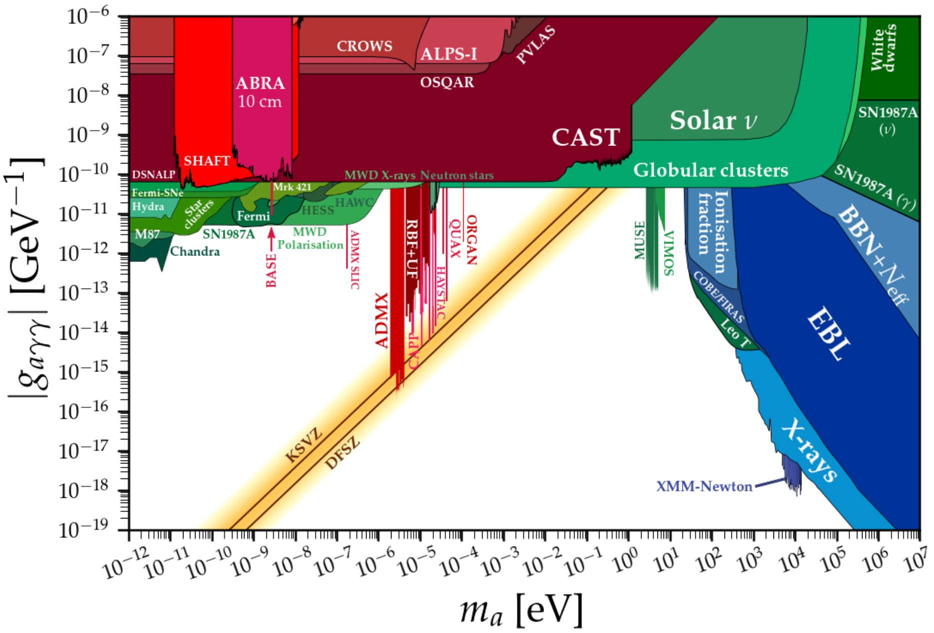

Figure 26: Axion-photon coupling strength limits [69]. Constraints in green do not account axions as DM candidates. The X-ray bounds assume axions as DM candidates.

both the strongest constraints and flux estimates. The X-ray bounds in Figure 26, assume the axions as DM candidates which would correspond to having $\frac{M}{\mu}$ axions per PBH. In reality, the number of axions produced through superradiant instabilities per PBH is smaller as previously estimated. We can then rescale the X-ray bounds in Figure 26 by a factor $\frac{N\mu}{M}$ where N is the number of axions produced per PBH. Now, we compare this rescalled observational data with the photon flux estimate, $2\Gamma_{a\gamma\gamma}N_\infty$. We use the N_∞ analytical expressions obtained in section 5, providing a parameter space in which the theoretical estimates surpass the observational data. Results are illustrated in Figure 27. We then convert the allowed parameter space in Figure 27, which is given in terms of the decay constant, f_a, into the coupling constant, $g_{a\gamma\gamma}$. We conclude that constraints from PBH superradiance where axions only account for a fraction of DM, are stronger than existing astrophysical constraints on keV-axions, namely from globular clusters, which are independent of axions accounting or not for a sizeable fraction of DM. We emphasize that these constraints assume 100% of the DM in PBHs with 10^{14} kg.

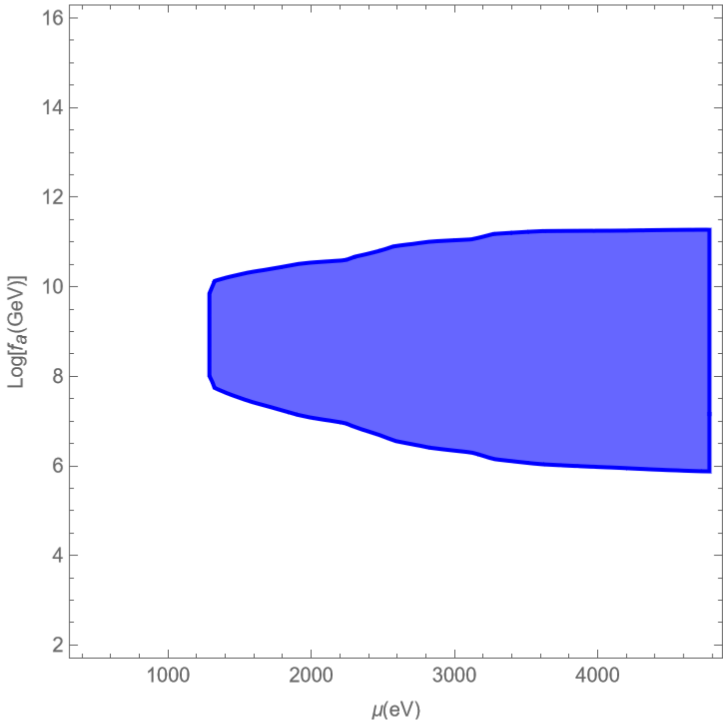

Figure 27: Parameter space for which theoretical flux estimates surpass observational data, and is therefore excluded. Parameters assumed: $M = 10^{14}$ kg, $\tilde{a} = 0.01$ and $|C_{a\gamma\gamma}| = 1$. The axion mass ranges over $\simeq [450 - 5000]$ eV (Figure 10).

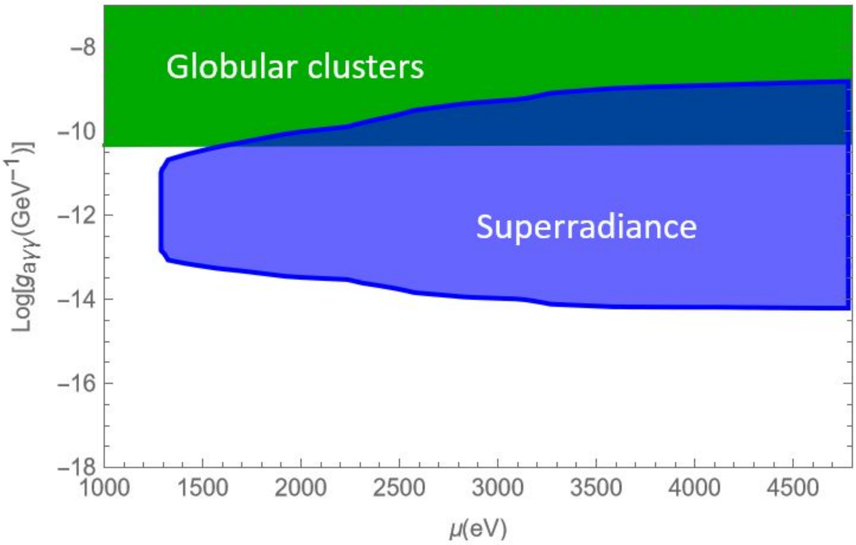

Figure 28: Constraints on the axion-photon coupling from PBH superradiance (blue), assuming 100% of DM in 10^{14} kg and $\tilde{a} = 0.01$ PBHs. For comparison, we show existing constraints on axions in the keV mass range that are independent on the fraction of DM they account for, from globular clusters (green).

7 Conclusion

In this thesis, we studied superradiant instabilities of axions, which decay into photons, in the vicinity of a rotating PBH, assuming PBHs are a relevant fraction of the DM. We used the perturbative analysis in [4], which should hold for $\alpha \ll 1$, where axion self-interactions lead to a non-linear mixing between the two dominant superradiant states, 211 and 322, alongside axion reabsorption by the black hole and emission to infinity (free axions). There may be other non-linear processes that populate different bound/free states or emit gravitational waves. However, since these are negligible when compared with the dominant processes, we perform a simplified analysis where the main self-interactions involve only two superradiant states.

One of the goals of this project was to describe the dynamics of the axion/black hole system both numerically and analytically to determine the number of axions produced by superradiance throughout the cosmic history. Since, due to the presence of interactions between superradiant states, a significant portion of the black hole's angular momentum is converted into axions that escape its gravitational potential, we separate our analysis for the axion production in two sections: axions produced within and outside the cloud.

Regarding axions produced within the cloud, for low f_a values where self-interactions are significant, the 211 axion number reaches an equilibrium value before extracting a significant portion of the black hole spin. This may remain constant until the present day or decrease in an adiabatic fashion as the black hole spins down and the superradiant growth rate decreases. For large f_a values, self-interactions become less and less important and the 211 axion number reaches the maximum possible value within the age of the universe.

When self-interactions are important, a large number of axions become free, but are nevertheless bound within the galaxy. There seems to be two restrictive factors for the N_∞ growth rate: the decay rate and the black hole's significant loss of angular momentum from superradiance.

For both cases, the system dynamics within the age of the universe varies depending on the specific parameters assumed. We successfully obtained analytical expressions that accurately describe the dynamics of these systems for different f_a values. These expressions agree with numerical data for the axion number estimated as of today within an average relative error of up to only $\simeq 3\%$.

For $\alpha \gtrapprox 0.1$ the analysis in [4] is unreliable and the number of axions within the cloud should reach the bosenova threshold [61, 62], significant larger than the equilibrium value.

The second goal was to estimate the Milky Way's galactic center and also the extragalactic background photon fluxes and compare theoretical results with observational data. Results obtained are as follows:

For axions within the cloud: in the perturbative analysis, flux estimates were not strong enough to surpass observational data. However, in the bosenova regime we envisage a parameter space in which estimates surpass this threshold for both flux sources providing an exclusion of the particular parameters assumed. This conclusion requires, however, a better understanding of the superradiant cloud dynamics for $\alpha \gtrapprox 0.1$.

For axions outside the cloud: in the perturbative analysis, we obtained a large region where the flux estimates exceed the observational data, thus, providing a constraint on the axion mass *vs* axion-photon coupling parameter space.

Throughout this analysis we fixed various parameters such as the black hole's mass, $M = 10^{14}$ kg, spin, $\tilde{a} = 0.01$ or $\tilde{a} = 0.9$ (whether concerning the equilibrium or the bosenova analysis, respectively), and $|C_{a\gamma\gamma}| = 1$. A more systematic approach to the problem would require a computational analysis on the full parameter space that may produce bounds on the axion-photon coupling strength limits, which we plan to do in future works. In addition, an interesting future avenue for research is to consider the effects and potential observability of gravitational waves from superradiant axion clouds around PBH DM.

We hope that our results also motivate other future studies of PBH superradiance.

Appendix A - Details on Klein Gordon equation in Kerr spacetime

Kerr's metric is not diagonal meaning that the calculation of 2.7 is not trivial. The metric may be represented in a matrix form as,

$$g_{\mu\nu} = \begin{bmatrix} g_{tt} & 0 & 0 & g_{t\phi} \\ 0 & \frac{\Sigma}{\Delta} & 0 & 0 \\ 0 & 0 & \Sigma & 0 \\ g_{\phi t} & 0 & 0 & g_{\phi\phi} \end{bmatrix} \tag{A.1}$$

where,

$$\begin{aligned} g_{t\phi} &= -\frac{2Mra\sin^2\theta}{\Sigma} \\ g_{tt} &= -\left(1 - \frac{2Mr}{\Sigma}\right) \\ g_{\phi\phi} &= \left(r^2 + a^2 + \frac{2Mra^2\sin^2\theta}{\Sigma}\right)\sin^2\theta \end{aligned} \tag{A.2}$$

In order to use equation 2.1 one has to find the determinant of the metric as well as its inverse. It is wise to notice that the coordinates may be written in a different order,

$$g_{\mu\nu} = \begin{bmatrix} g_{tt} & g_{t\phi} & 0 & 0 \\ g_{\phi t} & g_{\phi\phi} & 0 & 0 \\ 0 & 0 & g_{\theta\theta} & 0 \\ 0 & 0 & 0 & g_{\phi\phi} \end{bmatrix} \tag{A.3}$$

One then obtains two smaller 2×2 diagonal sub-matrices making the task of calculating the determinant and the inverse of the metric much easier. Evaluating these quantities by blocks and reorganizing the coordinates to the original form, one gets $g = -\Sigma^2 \sin^2\theta$ and,

$$g^{\mu\nu} = \begin{bmatrix} g^{tt} & 0 & 0 & g^{t\phi} \\ 0 & \frac{\Delta}{\Sigma} & 0 & 0 \\ 0 & 0 & \frac{1}{\Sigma} & 0 \\ g^{\phi t} & 0 & 0 & g^{\phi\phi} \end{bmatrix} \tag{A.4}$$

where,

$$
\begin{aligned}
g^{t\phi} &= -\frac{2Mra}{\Delta\Sigma} \\
g^{tt} &= -\frac{1}{\Delta}\Big(r^2 + a^2 + \frac{2Mra^2\sin^2\theta}{\Sigma}\Big) \\
g^{\phi\phi} &= \frac{\Delta - a^2\sin^2\theta}{\Sigma\Delta\sin^2\theta}
\end{aligned}
\tag{A.5}
$$

It is now straightforward to obtain the full Klein Gordon equation. Putting all pieces together one obtains equation 2.7.

Appendix B - Decay rate calculation

B.1 Decay rate

Let us consider the golden rule for decays. Suppose a particle 1 decays into two other particles,

$$1 \rightarrow 2 + 3 \tag{B.1}$$

The decay rate for this process is [70],

$$d\Gamma = |\mathcal{M}|^2 \frac{S}{2m_1} \frac{d^3\mathbf{p}_2}{(2\pi)^3 2E_2} \frac{d^3\mathbf{p}_3}{(2\pi)^3 2E_3} (2\pi)^4 \delta^4(P_1 - P_2 - P_3) \tag{B.2}$$

where $\mathcal{M}$ is the invariant amplitude and S is a statistical coefficient that goes with $\frac{1}{j!}$ for each j identical particles in the final state. For the specific case of the axion decay into two photons, the decay rate is significantly simplified in the rest frame[33] of the axion because the photons are massless. In this frame $E_1 = m_1$ and $\mathbf{p}_1 = 0$. Furthermore, one can write $E_2 = |\mathbf{p}_2|$ and $E_3 = |\mathbf{p}_3|$. Taking this into consideration, one can easily get a simplified formula by also taking advantage of some properties of the delta function [23]. Splitting the delta function as,

$$\delta^4(P_1 - P_2 - P_3) = \delta(m_1 - |\mathbf{p}_2| - |\mathbf{p}_3|)\delta^3(\mathbf{p}_2 + \mathbf{p}_3) \tag{B.3}$$

where the symmetries of the delta function were used, $\delta^3(x) = \delta^3(-x)$. For the particular case where the final state has two identical particles (thus $S = \frac{1}{2}$) and effectively using the latter delta function, the decay rate is then,

$$\Gamma = \frac{1}{4m_1(4\pi)^2} \int \frac{d^3\mathbf{p}_2}{|\mathbf{p}_2|^2} |\mathcal{M}|^2 \delta(m_1 - 2|\mathbf{p}_2|) \tag{B.4}$$

---

[33] In fact, equation B.2 was derived assuming the observer is in the rest frame. Considering the decaying particle at rest, the usual normalization factor $\frac{1}{2E_1}$ becomes $\frac{1}{2m_1}$.

Moving to spherical coordinates [23], $d^3\mathbf{p}_2 = |\mathbf{p}_2|^2 d|\mathbf{p}_2| sin\theta d\theta d\phi$, using the property $\delta(kx) = \frac{1}{|k|}\delta(x)$, and integrating over the angular part,

$$\Gamma = \frac{1}{32\pi m_1}\int_0^{+\infty} d|\mathbf{p}_2||\mathcal{M}|^2\delta(|\mathbf{p}_2| - \frac{m_1}{2}) = \frac{1}{32\pi m_1}|\mathcal{M}|^2 \tag{B.5}$$

Knowing the square modulus of the invariant amplitude one can then compute the decay rate.

B.2 Matrix element $\mathcal{M}$

The Lagrangian for the axion/photon interaction is [10],

$$\mathcal{L}_{a\gamma\gamma} = -\frac{1}{4}g_{a\gamma\gamma}aF_{\mu\nu}\tilde{F}^{\mu\nu} \tag{B.6}$$

where $g_{a\gamma\gamma}$ is the coupling constant that includes the fermion-loop integral [10]. The Feynman diagram leading to this interaction is,

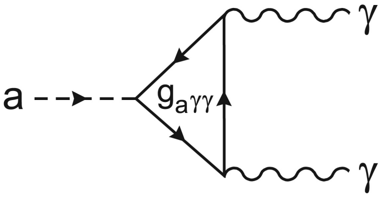

Figure 29: Feynman diagram of the decay of the axion into two photons with coupling strength $g_{a\gamma\gamma}$.

In order to get the Feynman rule for this interaction one can expand the field strength tensor and its dual. By doing so, one gets an expression of the form,

$$-\frac{g_{a\gamma\gamma}}{8}(\varepsilon^{\mu\nu\alpha\beta}\partial_\mu A_\nu\partial_\alpha A_\beta - \varepsilon^{\mu\nu\alpha\beta}\partial_\mu A_\nu\partial_\beta A_\alpha - \varepsilon^{\mu\nu\alpha\beta}\partial_\nu A_\mu\partial_\alpha A_\beta + \varepsilon^{\mu\nu\alpha\beta}\partial_\nu A_\mu\partial_\beta A_\alpha) \tag{B.7}$$

Taking into account the properties of the anti-symmetric Levi-Civita tensor and moving into momentum space, $\partial_\mu \rightarrow \mathrm{P}_\mu$ and $A^i_\nu \rightarrow \epsilon^{*\lambda_i}_\beta(P_i)$, the Feynman rule for such interaction is,

$$R_{a\gamma\gamma} = -\frac{1}{2}g_{a\gamma\gamma}\varepsilon^{\mu\nu\alpha\beta}P_{2\mu}\epsilon^{*\lambda_1}_\nu(P_2)P_{3\alpha}\epsilon^{*\lambda_2}_\beta(P_3) \tag{B.8}$$

One can then write the invariant amplitude as,

$$\mathcal{M} = -g_{a\gamma\gamma}\varepsilon^{\mu\nu\alpha\beta}P_{2\mu}\epsilon^{*\lambda_1}_\nu(P_2)P_{3\alpha}\epsilon^{*\lambda_2}_\beta(P_3) \tag{B.9}$$

where the $\frac{1}{2}$ term cancelled out due to the possible permutations of the outgoing state. One may now write the modulus squared of the invariant amplitude with the help of the completeness relation for the photon polarization [31] $\sum_\lambda \epsilon^{*\lambda}_\mu(P)\epsilon^\lambda_\nu(P) = \eta_{\mu\nu}$,

$$|\mathcal{M}|^2 = g^2_{a\gamma\gamma}\varepsilon^{\mu\nu\alpha\beta}\varepsilon^{\gamma\sigma\tau\rho}P_{2\mu}P_{2\gamma}P_{3\alpha}P_{3\tau}\eta_{\sigma\nu}\eta_{\rho\beta} \tag{B.10}$$

Finally, using the contraction for the Levi-Civita tensor $\varepsilon^{abcd}\varepsilon_{abkl} = 2(\delta^c_k\delta^d_l - \delta^c_l\delta^d_k)$,

$$|\mathcal{M}|^2 = 2g^2_{a\gamma\gamma}(P_2^\tau P_{3\tau}P_2^\alpha P_{3\alpha} - P_2^\gamma P_{2\gamma}p_3^\tau P_{2\tau}) \tag{B.11}$$

For the first term and using conservation of momentum, $P_1^2 = (P_2 + P_3)^2 = 2P_2 \cdot P_3$ since the photons are massless, which means that $2P_2 \cdot P_3 = -\frac{m_a^2}{2}$, m_a being the mass of the decaying particle, the axion. The second term of the previous expression is equal to zero because it corresponds to the product of the squared mass of the massless photons. This yields the final form of the matrix element,

$$|\mathcal{M}|^2 = \frac{m_a^4}{2}g^2_{a\gamma\gamma} \tag{B.12}$$

Thus, inserting this result in equation B.5 and renaming $m_1 \equiv m_a$,

$$\Gamma = \frac{g^2_{a\gamma\gamma}m_a^3}{64\pi} \tag{B.13}$$

The coupling constant $g_{a\gamma\gamma}$ for a general axion is given by [71],

$$g_{a\gamma\gamma} = \frac{\alpha_{EM}}{2\pi f_a}|C_{a\gamma\gamma}| \tag{B.14}$$

where $\alpha_{EM} \simeq \frac{1}{137}$ is the electromagnetic fine structure constant and $|C_{a\gamma\gamma}|$ is the effective coefficient that describes the mediators that carry the charge in the loop in Figure 29. This quantity has a wide range of possible values [72]. For a general axion,

$$\Gamma = \frac{\alpha^2_{EM}}{256\pi^3}|C_{a\gamma\gamma}|^2 m_a\left(\frac{m_a}{f_a}\right)^2 \tag{B.15}$$

For the particular case of the QCD axion,

$$|C_{a\gamma\gamma}| = \left(\frac{E}{\xi} - 1.92\right) \tag{B.16}$$

where E and ξ are the electromagnetic and color anomalies, respectively, of the axial current associated with the QCD axion. The quotient value $\frac{E}{\xi}$ varies depending the model one considers. For the KSVZ model [73], $\frac{E}{\xi} = 0$ if the electric charge of the new heavy quark is taken to vanish. Considering the decay constant relation between the QCD axion's mass and Λ_{QCD},

$$\Lambda^4_{QCD} \simeq f_a^2 m_a^2 \tag{B.17}$$

and putting all pieces together, one gets the final form of the decay rate of the QCD axion in this process [10],

$$\Gamma \simeq \frac{\alpha^2_{EM}}{64\pi^3}\frac{m_a^5}{\Lambda^4_{QCD}} \simeq 1.1 \times 10^{-24}\left(\frac{m_a}{\text{eV}}\right)^5 \text{s}^{-1} \tag{B.18}$$

where we assumed $\Lambda_{QCD} \simeq 75$ MeV [71].

8 References

[1] Ya B Zel'dovich. Pis' ma zh. eksp. teor. fiz. 14, 270 (1971)[jetp lett. 14, 180 (1971)]. *Zh. Eksp. Teor. Fiz*, 62:2076, 1972.

[2] William H Press and Saul A Teukolsky. Floating orbits, superradiant scattering and the black-hole bomb. *Nature*, 238(5361):211–212, 1972.

[3] Vitor Cardoso, Oscar JC Dias, José PS Lemos, and Shijun Yoshida. Black-hole bomb and superradiant instabilities. *Physical Review D*, 70(4):044039, 2004.

[4] Masha Baryakhtar, Marios Galanis, Robert Lasenby, and Olivier Simon. Black hole superradiance of self-interacting scalar fields. *Physical Review D*, 103(9):095019, 2021.

[5] Asimina Arvanitaki, Masha Baryakhtar, and Xinlu Huang. Discovering the qcd axion with black holes and gravitational waves. *Physical Review D*, 91(8):084011, 2015.

[6] Vitor Cardoso, Óscar JC Dias, Gavin S Hartnett, Matthew Middleton, Paolo Pani, and Jorge E Santos. Constraining the mass of dark photons and axion-like particles through black-hole superradiance. *Journal of Cosmology and Astroparticle Physics*, 2018(03):043, 2018.

[7] Mateja Bošković, Richard Brito, Vitor Cardoso, Taishi Ikeda, and Helvi Witek. Axionic instabilities and new black hole solutions. *Physical Review D*, 99(3):035006, 2019.

[8] Roberto D Peccei and Helen R Quinn. Cp conservation in the presence of pseudoparticles. *Physical Review Letters*, 38(25):1440, 1977.

[9] Roberto D Peccei. The strong cp problem and axions. In *Axions*, pages 3–17. Springer, 2008.

[10] G Rybka. 90. axions and other similar particles.

[11] Paulo B Ferraz, Thomas W Kephart, and João G Rosa. Superradiant pion clouds around primordial black holes. *Journal of Cosmology and Astroparticle Physics*, 2022(07):026, 2022.

[12] Stephen Hawking. Gravitationally collapsed objects of very low mass. *Monthly Notices of the Royal Astronomical Society*, 152(1):75–78, 1971.

[13] Christian T Byrnes and Philippa S Cole. Lecture notes on inflation and primordial black holes. *arXiv preprint arXiv:2112.05716*, 2021.

[14] Anne M Green and Bradley J Kavanagh. Primordial black holes as a dark matter candidate. *Journal of Physics G: Nuclear and Particle Physics*, 48(4):043001, feb 2021.

[15] Steven Detweiler. Klein-gordon equation and rotating black holes. *Phys. Rev. D*, 22:2323–2326, Nov 1980.

[16] Richard Brito, Vitor Cardoso, and Paolo Pani. *Superradiance.* Springer, 2020.

[17] Christopher M Hirata. Lecture xxvi: Kerr black holes: I. metric structure and regularity of particle orbits. *Caltech M/C*, pages 350–17.

[18] R Penrose. The question of cosmic censorship, chapter 5 in black holes and relativistic stars, r. *Wald (editor)*, 1994.

[19] Lawrence Howard Ford. Quantization of a scalar field in the kerr spacetime. *Physical Review D*, 12(10):2963, 1975.

[20] Milton Abramowitz and Irene A Stegun. *Handbook of mathematical functions with formulas, graphs, and mathematical tables*, volume 55. US Government printing office, 1964.

[21] AA Starobinskii. Amplification of waves reflected from a rotating black hole. Technical report, Inst. of Theoretical Physics, Moscow, 1973.

[22] Joao G Rosa and Thomas W Kephart. Stimulated axion decay in superradiant clouds around primordial black holes. *Physical review letters*, 120(23):231102, 2018.

[23] DJ Griffiths. Introduction to quantum mechanics, 3rd.

[24] Nouredine Zettili. Quantum mechanics: concepts and applications, 2003.

[25] Mark Srednicki. Quantum field theory(2006).

[26] GH Derrick. Math. *Phys*, 5:1252, 1964.

[27] Sidney Coleman. *Aspects of symmetry: selected Erice lectures.* Cambridge University Press, 1988.

[28] RJ Crewther, P Di Vecchia, G Veneziano, and Edward Witten. Chiral estimate of the electric dipole moment of the neutron in quantum chromodynamics. *Physics Letters B*, 88(1-2):123–127, 1979.

[29] CA Baker, DD Doyle, P Geltenbort, K Green, MGD Van der Grinten, PG Harris, P Iaydjiev, SN Ivanov, DJR May, JM Pendlebury, et al. Improved experimental limit on the electric dipole moment of the neutron. *Physical Review Letters*, 97(13):131801, 2006.

[30] J. Beringer et al. Review of Particle Physics (RPP). *Phys. Rev. D*, 86:010001, 2012.

[31] Matthew D Schwartz. *Quantum field theory and the standard model.* Cambridge University Press, 2014.

[32] Jae Hyeok Chang, Rouven Essig, and Samuel D. McDermott. Supernova 1987a constraints on sub-gev dark sectors, millicharged particles, the qcd axion, and an axion-like particle. *Journal of High Energy Physics (Online)*, 2018(9), 9 2018.

[33] Matthew J. Stott and David J. E. Marsh. Black hole spin constraints on the mass spectrum and number of axionlike fields. *Phys. Rev. D*, 98(8):083006, 2018.

[34] Ricardo Z. Ferreira, Alessio Notari, and Fabrizio Rompineve. Dine-fischler-srednicki-zhitnitsky axion in the CMB. *Physical Review D*, 103(6), mar 2021.

[35] Edward W Kolb and Michael S Turner. *The early universe.* CRC press, 2018.

[36] BP Abbott et al. (virgo, ligo scientific). *Phys. Rev. Lett*, 116:061102, 2016.

[37] JS Bagla. Compact objects and black holes: Nobel prize for physics 2020. *arXiv preprint arXiv:2012.08774*, 2020.

[38] Bernard Carr and Florian Kühnel. Primordial black holes as dark matter candidates. *SciPost Physics Lecture Notes*, may 2022.

[39] Masahiro Kawasaki, Alexander Kusenko, and Tsutomu T. Yanagida. Primordial seeds of supermassive black holes. *Physics Letters B*, 711(1):1–5, may 2012.

[40] Daniel Baumann. Tasi lectures on inflation. *arXiv preprint arXiv:0907.5424*, 2009.

[41] J.Rosa. Introduction to cosmology.

[42] Y. Akrami et al. Planck 2018 results: X. constraints on inflation. *Astronomy and Astrophysics*, 641, September 2020.

[43] G. Hinshaw et al. FIVE-YEAR iWILKINSON MICROWAVE ANISOTROPY PROBE/i OBSERVATIONS: DATA PROCESSING, SKY MAPS, AND BASIC RESULTS. *The Astrophysical Journal Supplement Series*, 180(2):225–245, feb 2009.

[44] National Aeronautics and Space Administration - What is the Universe Made Of? *https://wmap.gsfc.nasa.gov/universe/uni_matter.html.*

[45] Vera C Rubin. Evidence for dark matter from rotation curves: Ten years later. In *AIP Conference Proceedings*, volume 222, pages 371–380. American Institute of Physics, 1991.

[46] Basudeb Dasgupta and Joachim Kopp. Sterile neutrinos. *Physics Reports*, 928:1–63, sep 2021.

[47] Bernard J. Carr and S. W. Hawking. Black holes in the early Universe. *Mon. Not. Roy. Astron. Soc.*, 168:399–415, 1974.

[48] Bernard J Carr. The primordial black hole mass spectrum, 1975.

[49] Bernard J. Carr. Primordial black holes: Recent developments. *eConf*, C041213:0204, 2004.

[50] Chul-Moon Yoo, Tomohiro Harada, and Hirotada Okawa. Threshold of Primordial Black Hole Formation in Nonspherical Collapse. *Phys. Rev. D*, 102(4):043526, 2020.

[51] William H Press and Paul Schechter. Formation of galaxies and clusters of galaxies by self-similar gravitational condensation. *The Astrophysical Journal*, 187:425–438, 1974.

[52] Pablo Villanueva-Domingo, Olga Mena, and Sergio Palomares-Ruiz. A brief review on primordial black holes as dark matter. *Frontiers in Astronomy and Space Sciences*, page 87, 2021.

[53] Misao Sasaki, Teruaki Suyama, Takahiro Tanaka, and Shuichiro Yokoyama. Primordial black holes—perspectives in gravitational wave astronomy. *Classical and Quantum Gravity*, 35(6):063001, 2018.

[54] Masahiro Kawasaki, Alexander Kusenko, Yuichiro Tada, and Tsutomu T. Yanagida. Primordial black holes as dark matter in supergravity inflation models. *Phys. Rev. D*, 94:083523, Oct 2016.

[55] Leor Barack, Vitor Cardoso, and Richard Brito et al. Black holes, gravitational waves and fundamental physics: a roadmap. *Classical and Quantum Gravity*, 36(14):143001, jun 2019.

[56] Fabio Capela, Maxim Pshirkov, and Peter Tinyakov. Constraints on primordial black holes as dark matter candidates from capture by neutron stars. *Physical Review D*, 87(12), jun 2013.

[57] Paolo Pani and Abraham Loeb. Tidal capture of a primordial black hole by a neutron star: implications for constraints on dark matter. *Journal of Cosmology and Astroparticle Physics*, 2014(06):026–026, jun 2014.

[58] Guillaume Defillon, Etienne Granet, Peter Tinyakov, and Michel H. G. Tytgat. Tidal capture of primordial black holes by neutron stars. *Phys. Rev. D*, 90:103522, Nov 2014.

[59] Mehrdad Mirbabayi, Andrei Gruzinov, and Jorge Noreñ a. Spin of primordial black holes. *Journal of Cosmology and Astroparticle Physics*, 2020(03):017–017, mar 2020.

[60] Koppelman, Helmer H. and Helmi, Amina. Determination of the escape velocity of the milky way using a halo sample selected based on proper motion. *A&A*, 649:A136, 2021.

[61] Asimina Arvanitaki, Savas Dimopoulos, Sergei Dubovsky, Nemanja Kaloper, and John March-Russell. String axiverse. *Physical Review D*, 81(12), jun 2010.

[62] Hirotaka Yoshino and Hideo Kodama. Bosenova collapse of axion cloud around a rotating black hole. *Progress of theoretical physics*, 128(1):153–190, 2012.

[63] Ranjan Laha, Julian B. Muñoz, and Tracy R. Slatyer. *integral* constraints on primordial black holes and particle dark matter. *Phys. Rev. D*, 101:123514, Jun 2020.

[64] R. Yunis, C. R. Argüelles, N. E. Mavromatos, A. Moliné, A. Krut, J. A. Rueda, and R. Ruffini. New constraints on sterile neutrino dark matter from the galactic center, 2018.

[65] Davide Cadamuro and Javier Redondo. Cosmological bounds on pseudo nambu-goldstone bosons. *Journal of Cosmology and Astroparticle Physics*, 2012(02):032–032, feb 2012.

[66] N. W. Evans, J. L. Sanders, and Alex Geringer-Sameth. Simple j-factors and d-factors for indirect dark matter detection. *Physical Review D*, 93(10), may 2016.

[67] B. J. Carr, Kazunori Kohri, Yuuiti Sendouda, and Jun'ichi Yokoyama. New cosmological constraints on primordial black holes. *Phys. Rev. D*, 81:104019, May 2010.

[68] J.M. Overduin and P.S. Wesson. Dark matter and background light. *Physics Reports*, 402(5-6):267–406, nov 2004.

[69] Ciaran O'HARE. cajohare/axionlimits: Axionlimits, July 2020.

[70] Michael Edward Peskin and Daniel V. Schroeder. *An Introduction to Quantum Field Theory*. Westview Press, 1995. Reading, USA: Addison-Wesley (1995) 842 p.

[71] Giovanni Grilli di Cortona, Edward Hardy, Javier Pardo Vega, and Giovanni Villadoro. The QCD axion, precisely. *Journal of High Energy Physics*, 2016(1), jan 2016.

[72] Martin Bauer, Matthias Neubert, and Andrea Thamm. Collider probes of axion-like particles. *Journal of High Energy Physics*, 2017(12), dec 2017.

[73] Jihn E. Kim. Weak-interaction singlet and strong CP invariance. *Phys. Rev. Lett.*, 43:103–107, Jul 1979.